Characterization of the mechanical and hydrological properties of a rock joint by using a fractal model

Sumihiko MURATA

Characterization of the mechanical and hydrological properties of a rock joint by using a fractal model

Sumihiko MURATA

ACKNOWLEDGMENTS

I would like to acknowledge Professor Toshiaki Saito, Department of Earth Resources Engineering, Kyoto University for his valuable advice and kindly guidance throughout preparation of this thesis.

I also wish to express my gratitude to Professor Yuzo Ohnishi, Department of Civil Engineering System, Kyoto University and Professor Kenji Aoki, Department of Earth Resources Engineering, Kyoto University for giving me valuable suggestions.

Special thanks are due to Associate Professors Toshihiro Asakura, Toshifumi Matsuoka, Kazuhiko Tsukada, Department of Earth Resources Engineering, Kyoto University and Professor Takashi Nishiyama, Department of Energy Science and Technology, Kyoto University for giving their kind suggestions and encouragement.

The discussion with Dr. Naondo Jin, Lecturer of Department of Mathematics, Faculty of Education, Shiga University, was very helpful on the mathematical treatment of statistical self-affine fractal discussed in Chapter2.

I thank my graduate students, Mr. M. Nakai, now working for Maeda Corp. and Koji Ogawa, now working for Oyo Corp. They excellently carried out the shear tests and surface profile measurements for many specimens discussed in Chapter 3 and Chapter 4. I wish their valuable activities and success in their major field.

I would thank the stuffs of Reservoir and Recovery Laboratory, Technology Research Center, Japan National Oil Corporation. Director K. Okatsu, now vice president of London Representative Office of JNOC, especially permitted me to use the experimental apparatuses, and Mr. M. Ueki and Ms. H. Kaido helped me to measure the fracture permeability discussed in Chapter 5. In addition, the several pieces of advice that Mr. Ueki gave me based on his long years experience on rock core analysis were great help.

Clearly, this work could not have been completed without the support of other many people. I would express my acknowledgement to all of them.

Finally, I wish to express special thanks to my parents, my wife and my children for their constant encouragement.

January 15, 2001
Sumihiko MURATA

CONTENTS

Chapter 1 Introduction 1

1.1. Introduction 1

1.2. Review of the previous researches 2

1.2.1. The researches on mechanical properties of rock fractures 2

1.2.2. The researches on hydrological properties of rock fractures 4

1.3. The objectives and the outline of this thesis 7

References 9

Chapter 2 Fractal model of a fracture surface by using variogram method 13

2.1. Introduction 13

2.2. Fractal of fracture surfaces 14

2.2.1 Self-similar fractal and self-affine fractal 14

2.2.2 Fractal of a fracture surface and the methods to make a fractal model . . 15

2.3 Variogram method 19

2.3.1 Mathematical expression of variogram method 19

2.3.2 The problem of variogram method and its causes 21

2.4 Discussion 23

2.4.1 The range of lag where the power low is valid 23

2.4.2 The matters that require special attention for the variogram method . . . 26

2.5. Conclusions 27

References 27

Chapter 3 Evaluation of surface roughness and mechanical properties of rock fracture by using a fractal model 29

3.1. Introduction 29

3.2. Fractal model and steepness by variogram method 31

3.3. The correlation between steepness and *JRC* 33

3.4. Estimation of rock fracture surface roughness by using JRC-diagram 36

3.4.1. JRC-diagram 36

3.4.2. Control size 39

3.4.3. Size effect of *JRC* 42

3.5. *JRC* and shear strength of rock fractures 44

3.5.1. Profile measurement and shear test 44

3.5.2. Estimation of *JRC* and shear strength 48
3.5.3. Discussion 52
3.6. Conclusions 56
References 57

Chapter 4 Change of surface properties and contact condition of rock fracture with the progress of shearing 59
4.1 Introduction 59
4.2. Surface topography measurement and observation of contact condition 61
4.2.1. Fracture specimen of rock 61
4.2.2. Measurement of fracture surface topography 62
4.2.3. Microscope observation of contact condition of fractures 63
4.3. Results of surface topography measurement 63
4.3.1. The change of surface height 63
4.3.2. The change of MEDF 65
4.3.3. The change of power spectral density and fractal property 67
4.3.4. The change of interlocking 69
4.4. Results of microscope observation 70
4.5. The relation between the fracture contact area and P-wave amplitude 72
4.5.1. The specimens for P-wave measurement 72
4.5.2. P-wave measurement and shear test 74
4.5.3. The relation between the contact area and P-wave amplitude 75
4.5.4. The change of P-wave amplitude during the shear test 77
4.6. Discussion on the shear process 79
4.7. Conclusions 83
References 84

Chapter 5 Characterization of fracture permeability by using a fractal model 85
5.1 Introduction 85
5.2 Permeability measurement of single fracture 86
5.2.1 Specimens of the single fracture 86
5.2.2 Measurement of surface topography of the single fracture 88
5.2.3 Permeability measurement 89
5.3 The results of the permeability measurement 90
5.3.1 The results of surface topography measurement 90
5.3.2 The results of the permeability measurement 91

5.4 Deviation from the cubic law of fracture permeability
described by a fractal model 98
5.4.1 Fracture permeability described by the equivalent channel model 98
5.4.2 Deviation from the cubic law of fracture permeability
described by using a fractal model 102
5.4.3 Discussion 104
5.5 Conclusions 106
References 107

Chapter 6 The effect of tortuosity on the fracture permeability 109
6.1 Introduction 109
6.2 Visualization of fluid flow through fractures 110
6.2.1 Method to generate an aperture distribution of fracture
based on the fractal model 110
6.2.2 The physical flow experiments 114
6.2.3 The numerical flow simulations 117
6.3 The results of the visualization 119
6.3.1 The results of physical flow experiments 119
6.3.2 The results of numerical flow simulations 122
6.4 Discussion 124
6.5 Conclusions 125
References 126

Chapter 7 Concluding remarks 129

LIST OF FIGURES AND TABLES

Chapter 2

Figure 2.1: Self-similar fractal (a) and self-affine fractal (b).
Figure 2.2: An example of log-log plot for the box-counting methods.
Figure 2.3: Illustration of the boxes used in the modified box-counting method.
Figure 2.4: Log-log plot of power spectral density of fracture surface.
Figure 2.5: Fractal model by using the variogram method.
Figure 2.6: The variogram plot for a fractal profile generated by Fourier filtering method.
Figure 2.7: The plot of the hypergeometric function of Equation (2.14).
Figure 2.8: The long profile generated by Fourier filtering method.
Figure 2.9: The variogram plots of the profiles cut from the long profile drawn in Figure 6.

Chapter 3

Figure 3.1: JRC-profiles. (After Barton and Choubey, 1977)
Figure 3.2: Fractal model by using the variogram method.
Figure 3.3: The variogram plot of JRC-profiles.
Figure 3.4: Relation between *JRC* and steepness.
Figure 3.5: Relation between *JRC* and fractal dimension.
Figure 3.6: JRC-diagram that is a self-similar fractal model determined by the variogram method.
Figure 3.7: Surface profiles of the artificial fracture (a) and the natural fracture (b).
Figure 3.8: The log-log plot of the PSD function of surface profile and aperture profile for the artificial rock fracture shown in Figure 3.7.
Figure 3.9: Aperture profile of a rock fracture.
Figure 3.10: The surface profile and the aperture profile of a rock fracture.
Figure 3.11: Relation between the JRC-model and the fractal model of a rock fracture surface profile.
Figure 3.12: The artificial fracture surfaces by Brazilian test procedure.
Figure 3.13: Surface profiler composed of two linear positioning systems and one laser displacement transducer.
Figure 3.14: The schematic diagram of shear testing machine.

Figure 3.15: The log-log plots of the averaged PSD functions of the surface and aperture profiles for the granite specimen sheared under the normal stress of 14MPa.
Figure 3.16: The variogram plots for the granite specimen sheared under the normal stress of 14MPa.
Figure 3.17: An example of the selected profiles and determined *JRC* values.
Figure 3.18: The shear displacement vs. shear stress curves and shear displacement vs. vertical displacement curves for each fractured specimen.
Figure 3.19: Cross plot for the estimated shear strength and measured shear strength.

Table 3.1: Steepness and fractal dimension of JRC-profile.
Table 3.2: Young's modulus, Poisson's ratio and uniaxial compressive strength of the core samples.
Table 3.3: The estimated interlocking wavelength, steepness, fractal dimension and *JRC*
Table 3.4: Typical basic friction angle (after Barton and Choubey, 1977)
Table 3.5: The peak shear strength estimated by JRC-diagram and JRC-profile and the peak and residual shear strength obtained by the shear test.
Table 3.6: Estimated actual interlocking wavelength for the fracture surface before shear test.

Chapter 4

Figure 4.1: The shape of the rock specimen and the method to make a rock fracture surface.
Figure 4.2: The shear displacement vs. shear stress and normal displacement vs. shear displacement curves obtained from the shearing.
Figure 4.3: A result of the surface topography measurement.
Figure 4.4: The distribution of surface height change.
Figure 4.5: The change of MEDF for the specimen of different stage of shearing.
Figure 4.6: The change of PSD for the specimen of each stage of shearing.
Figure 4.7: The contact condition of the rock fractures observed by a microscope.
Figure 4.8: The specimens arranged to have different contact area.
Figure 4.9: The shear testing machine and P-wave measurement system.
Figure 4.10: The observed waveforms for the specimens of different contact area.
Figure 4.11: The relation between the contact area and P-wave amplitude.
Figure 4.12: Shear displacement vs. shear stress curves and shear displacement vs.

normal displacement curves for the fractured specimens.
Figure 4.13: Observed waveforms according to the progress of shearing.
Figure 4.14: The change of the rms-amplitude with the progress of shearing.
Figure 4.15: Five phases of shear process.
Figure 4.16: The dilatancy curve and the MEDF curve.

Table 4.1: The list of the rock fracture specimens used for the topography measurement and microscope observation.
Table 4.2: The mean and the standard deviation (S.D.) of the change of surface height caused by the shearing.
Table 4.3: The change of the fractal dimension and failure-limited frequency.
Table4.4: The change of interlocking frequency with the progress of shearing.
Table 4.5: Summary of the P-wave travel-time, velocity and amplitude.

Chapter 5

Figure 5.1: The epoxy core specimens containing a single fracture
Figure 5.2: The stress-strain curve of the epoxy core specimen.
Figure 5.3: An example of the variogram plot for T4, M2 and I2
Figure 5.4: Relation between the deviation from the cubic law of fracture permeability, k_f/k_c and the mean fracture aperture, $<d>$.
Figure 5.5: The correlation between the deviation from the cubic law of fracture permeability, k_f/k_c, and the fractal parameters
Figure 5.6: Relation between the fracture permeability, k_f, and the mean fracture aperture, $<d>$.
Figure 5.7: The correlation between the fracture permeability, k_f, and the fractal parameters.
Figure 5.8: The relation between the fracture permeability, k_f, and the confining pressure, P_c.
Figure 5.9: The relation between the fracture permeability, $k_f^{1/3}$, and the confining pressure, P_c.
Figure 5.10: Geometry used in the equivalent channel model. (Redrawn from Walsh and Brace, 1984).
Figure 5.11: The relation between the fracture surface area, A_f, and the nominal fracture area, A.
Figure 5.12: Explanation of flow-path length along a fractal surface measured by h.

Figure 5.13: The actual flow-path length on the fracture surface, L_t, the projected flow-path length on the XY-plane, L, and the nominal fracture length, L_x.

Table 5.1: The specimens of natural and artificial rock fracture

Table 5.2: The uniaxial compressive strength, Young's modulus and Poisson's ratio of the epoxy core specimen.

Table 5.3: The mean value of the fractal dimension, steepness and rms-height.

Table 5.4: The fracture shape factor, β, of various cross section shape (after Schön, 1996).

Table 5.5: The results of sensitivity check of the fractal dimension, D, steepness, V, and two-dimensional tortuosity, α, on the deviation from the cubic law of fracture permeability, k_f/k_c, for the interlocking wavelength, h, of 0.1mm, 0.5mm, 10.0mm.

Chapter 6

Figure 6.1: PSD function of fracture surface profile and fracture aperture profile.

Figure 6.2: PSD function of fracture surface profile and fracture aperture profile for the fracture generated by Brown's method, (a) and Glover's method, (b).

Figure 6.3: Algorithm of Glover's method described by Fortran cord.

Figure 6.4: The prepared specimen for each type of fracture, IL1 and PL1.

Figure 6.5: Schematic diagram of the physical flow experiment.

Figure 6.6: Influx and efflux in the small volume element.

Figure 6.7: Fluid flow image observed in the physical flow experiment.

Figure 6.8: Two-leveled image of the fracture whose pore space is filled with the tracer

Figure 6.9: Fracture contact area.

Figure 6.10: Simulated volumetric flow rate vectors plotted on the image of the fracture aperture distribution.

Table 6.1: The fractal dimension, steepness and interlocking wavelength of the specimens for each specimen.

Table 6.2: The ratio of contact area to the fracture area, mean fracture aperture, hydraulic head, volumetric flow rate and two-dimensional tortuosity

Table 6.3: The deviation from the cubic law of fracture permeability, k_f/k_c estimated from the results of the physical flow experiment and numerical flow simulation and from the theoretical equation.

NOMENCLATURE

Chapter 1

JRC	joint roughness coefficient
JCS	joint wall compressive strength
L_0, L_n	length
q	volumetric flow rate
Re	Reynolds number
a_s	the ratio of the failed region area to the total area of the fracture
d	fracture aperture
k_f	fracture permeability
Ψ	friction factor of fluid fllow
Δh	the difference of hydraulic head
ε	the surface roughness in terms of the absolute height of the asperities
ϕ_μ,	the friction angle of asperity surface
ϕ_0	the friction angle of sheared surface
ϕ_f	the average of ϕ_μ.
ϕ_b	the basic friction angle of the joint surface
ϕ_r	residual fiction angle
η	the degree of interlocking
μ	fluid viscosity
$\dot{v}$	dilation rate at failure
σ_n	normal stress acting on the shear plane
τ	shear strength

Chapter 2

D	fractal dimension
H	Hurst exponent
h	lag
λ	profile length
σ	standard deviation of height distribution of the profile
$z(x)$	the value of data at point x
$G(f)$	power spectral density function of a fracture surface profile
$C(h)$	autocorrelation function
${}_pF_q\{\ \}$	hypergeometric function
$\Gamma\{\ \}$	gamma function

$<>$	expectation operator

Chapter 3

D	fractal dimension
H	Hurst exponent
JRC	joint roughness coefficient
JCS	joint wall compressive strength
V	steepness
h	lag
r_l	identical divider length
ϕ_b	basic friction angle
ϕ_r	residual fiction angle
σ_n	effective normal stress acting on the joint surface
τ	peak shear strength
$z(x)$	the profile height at measuring point x
$\gamma(h)$	variogram function

Chapter 4

K_n	specific stiffness in normal direction
T_p	the transmission coefficient of P-wave
V-1st	first-wave amplitude
V-rms	rms-amplitude
Z_p	the seismic impedance of P-wave
h	lag
r	sampling interval
l	profile length
ω	frequency
$z(x)$	surface height at x

Chapter 5

A	nominal fracture area
A_l	the cross-sectional area of the equivalent channel perpendicular to the streamline
A_x	the cross-sectional area of the equivalent channel perpendicular to the specimen axis
A_c	cross-sectional area of the core specimen perpendicular to the core axis
A_f	surface area of the fracture

D	fractal dimension
L	the projected flow-path length on the XY-plane
L_y	fracture width
L_x	fracture length
L_t	the actual flow-path length on the fracture surface
P	normal stress
P_c	confining pressure
P_e	effective confining pressure
V	steepness
V_b	bulk volume
V_f	fracture volume
d	fracture aperture
$<d>$	mean fracture aperture
d_m	mechanical aperture
d_h	hydraulic fracture aperture
f	correction factor for the surface roughness of a fracture
h	control size that corresponds to the size of asperity along which fluid flows faithfully
k_f	measured fracture permeability
k_c	calculated fracture permeability using cubic law
m	hydraulic radius
q	volumetric flow rate
α	two-dimensional tortuosity
β	the shape factor of pore
ϕ	porosity
μ	fluid viscosity
σ	the rms-height of fracture surface
τ	tortuosity
dp/dx	hydraulic pressure gradient
dp/dl	pressure gradient along the streamline
$\gamma(h)$	variogram function

Chapter 6

D	fractal dimension
L_x	fracture length
L_y	fracture width
$R1, R2, R3$	random number

V	steepness
d_h	hydraulic fracture aperture
e	fracture aperture
f	spatial frequency
f_c	interlocking frequency
k_f	the permeability of a general rough fracture
k_c	the permeability of parallel smooth plates
p	flow potential
q	volumetric flow rate
u, v	flow rate
α	two-dimensional tortuosity
β	fracture shape factor
Δp	pressure difference between inlet and outlet
ζ	roll-off parameter
μ	fluid viscosity

CHAPTER 1

INTRODUCTION

1.1. Introduction

Rock masses contain the several kinds of fractures such as faults, joints, fissures, cracks and artificial fractures. These fractures are weaker and more deformable than the intact parts of the rock masses. Therefore, the mechanical properties of the fractures are the most important factors affecting the stability of rock structures. Among the mechanical properties of rock fractures, the shear property is especially important because it mainly governed the failure or large deformation of the rock structures. Moreover, the fractures have considerably higher permeability than the intact parts of the rock masses except for the perfectly interlocking or clays filling fractures. Therefore, the hydrological properties of the fractures are the most important factors affecting the hydrological behavior of the rock masses. Among the hydrological properties of rock fractures, permeability is especially important because it governs the flow rate of fluid in the rock masses. For these reasons, the mechanical and hydrological properties of rock fractures are main subjects for rock engineering and petroleum engineering.

The mechanical and hydrological properties of a rock fracture are mainly affected by its surface properties that can be represented by the geometric and material properties of the fracture surfaces. Because the surface properties govern the parameters of contact condition of the fracture such as surface roughness, aperture, interlocking and contact area. In addition, these parameters affect the mechanical and hydrological properties. Therefore, many pieces of research to represent the mechanical and hydrological properties of rock fractures by quantifying the surface properties have been carried out (e.g. Patton, 1966; Ladanyi and Archambault, 1970; Barton and Choubey, 1977; Bandis *et al.*, 1981; Swan, 1981, 1983; Swan and Zongqi, 1985; Brown and Scholz, 1985, 1986; Witherspoon *et al.*, 1980; Walsh, 1981; Tsang and Witherspoon, 1983; Tsang, 1984; Brown, 1987, 1989; Zimmerman, 1991).

In this chapter, first, the previous researches on this subject are reviewed; second, the objectives and the outline of this thesis are presented.

1.2. Review of the previous researches

1.2.1. The researches on mechanical properties of rock fractures

As mentioned above, the shear property is especially important among the mechanical properties of rock fractures. Here, the researches on the shear properties are mainly reviewed.

Patton (1966) investigated the shear strength of fractures by using artificial plaster-fractures whose surface contains a number of regular and equal saw-tooth asperities. Considering the failure of the asperities, he obtained the following conclusions:

1) Failure envelopes, relation between shear strength and normal stress, for specimens with irregular failure surfaces are curved.
2) Changes in the slope of a failure envelope reflect changes in the mode of failure.
3) Changes in the mode of failure are related to the physical properties of asperities along the failure surface.

He represented a curved failure envelope by two straight lines, and suggested that the bilinear failure envelopes are adequate for some engineering design purposes. However, he concluded that to facilitate an understanding of the failure mechanism curved failure envelopes reflecting the multiple modes of shear failure appear to be a necessity.

In order to represent the curved failure envelopes, Ladanyi and Archambault (1970) proposed the next equation by adding a term due to the partial asperities shearing to the Rowe's equation (1964).

$$\tau = \frac{\sigma_n(1-a_s)(\dot{v}+\tan\phi_\mu)+a_s(\sigma_n\tan\phi_0+s_0\eta)}{1-(1-a_s)\dot{v}\tan\phi_f} \tag{1.1}$$

where τ is the shear strength, σ_n is the normal stress acting on the shear plane, ϕ_μ and ϕ_0 are the friction angles of asperity surface and sheared surface respectively, and ϕ_f is the average of ϕ_μ. In addition, a_s is the ratio of the failed region area to the total area of the fracture, $\dot{v}$ is the dilation rate at failure and η is the degree of interlocking. Since a_s and $\dot{v}$ change continuously according to the change of σ_n, this equation can represent the curved failure envelope.

On the other hand, Barton (1973) did not take such a theoretical approach but an experimental approach to represent a failure envelope. He presented a next famous experimental equation to predict peak shear strength based on the

experimental results of over 100 rock joint specimens.

$$\tau = \sigma_n \tan\left[JRC \log_{10}\left(\frac{JCS}{\sigma_n}\right) + \phi_b \right] \tag{1.2}$$

where JRC is the joint roughness coefficient, ϕ_b is the basic friction angle of the joint surface, JCS is the joint wall compressive strength, τ is the peak shear strength and σ_n is the effective normal stress acting on the joint surface. Barton and Choubey(1977) adopted the residual fiction angle, ϕ_r, instead of ϕ_b to apply this equation to weathered joints. Furthermore, in order to evaluate the JRC, they presented a very convenient method in addition to the simple shear testing method such as tilt test and push/pull test. This method determines the JRC by comparing the profile of rock joint surface with the typical 10 profiles whose JRC is from 0 to 20. Hereafter, the profiles are called JRC-profiles. Moreover, Barton and Choubey (1977), Bandis *et al.* (1981) and Barton *et al.* (1985) presented the next experimental equation to predict the size effect of JRC and JCS.

$$\begin{aligned} JRC_n &= JRC_0 \left[\frac{L_n}{L_0}\right]^{-0.02 JRC_0} \\ JCS_n &= JCS_0 \left[\frac{L_n}{L_0}\right]^{-0.03 JRC_0} \end{aligned} \tag{1.3}$$

where L_0, JRC_0, and JCS_0 are respectively the length, JRC and JCS of original size respectively, and L_n, JRC_n, JCS_n are the length, JRC and JCS of predicted size respectively. Owing to these efforts of Baton's group, the peak shear strength can be evaluated easily, and consequently the Barton's method is widely used. However, it should be kept in mind that JRC and JCS are experimentally determined and they have no theoretical background.

In contrast to the above researches, Swan (1981, 1983), Swan and Zongqi (1985), Brown and Scholz (1985, 1986), and Yoshioka and Scholz (1989a, 1989b) theoretically described the mechanical properties of a fracture by applying the contact theory of rough surfaces developed in tribology. In these researches, the hemispheric asperities were assumed to be in elastic Hertzian contact at contact points, and the normal and shear forces acting on the fracture were evaluated by the summation of individual normal and shear forces mobilized at each contacting point depending on the statistical asperity-height distribution.

Swan (1981, 1983) measured the surface profiles of rock fractures and developed a discrete numerical model to evaluate the distribution of contacting asperities by applying the contact theory of Greenwood and Williamson (1966). Brown and Scholz (1985a, 1986) pointed out that the contact theory of Greenwood and Tripp (1971) are inadequate for the interlocking fractures; and they applied the contact theory of Greenwood and Williamson (1966) to the composite topography that is the distribution of summed height of facing two fracture surfaces. Swan and Zongqi (1985), Yoshioka and Scholz (1989a, 1989b) applied the contact theory of Yamada *et al.* (1978a, 1978b), and then they presented the theoretical equation to describe the shear behavior of rock fractures before a slip is initiated. In these researches, Swan and Zongqi discussed the size effect of shear compliance; Yoshioka and Scholz discussed the effect of initial aperture of fractures on the shear properties and experimentally showed that their theoretical equation can predict the shear stiffness just before a slip is initiated.

In addition to these researches, Plesha (1987), Plesha and Haimson (1988) suggested that the quantitative descriptions of behavior of dilation, bulking and surface damage are necessary, and developed the constitutional equation that can describe such the items.

1.2.2. The researches on hydrological properties of rock fractures

Since fracture permeability governs the hydrological properties of rock masses, many pieces of research have focused on the evaluation of fracture permeability. Generally, the fracture permeability, k_f, is evaluated by the next equation based on the cubic law that is derived from the laminar flow between smooth parallel plates.

$$k_f = \frac{d^2}{12\mu} \tag{1.4}$$

where d is the fracture aperture and μ is the fluid viscosity. However, the facing two surfaces of an actual fracture are rough and they are in contact with each other at several points; that is, actual fractures cannot be assumed to be the smooth parallel plates. For this reason, actual fracture permeability deviates from the permeability determined by Equation (1.4). Therefore, many pieces of research to investigate the fluid flow behavior in a fracture and the degree of deviation from the cubic law, and to develop an empirical or theoretical equation in order to evaluate the fracture permeability considering the effect of surface roughness or contact condition have

been carried out.

Lomize (1951) investigated the effect of surface roughness by flooding experiments for the sand coated parallel glass plates. He introduced the surface roughness, ε, in terms of the absolute height of the asperities, and then developed the next empirical equation.

$$\Psi = \frac{96}{\mathrm{Re}}\left[1+6.0\left(\frac{\varepsilon}{d}\right)^{1.5}\right] = \frac{96}{\mathrm{Re}} f \tag{1.5}$$

where Ψ is the friction factor, Re is the Reynolds number and f is a factor that accounts for the deviation from the ideal condition on which the cubic law is standing. This equation is valid for $\varepsilon/d>0.065$. Louis (1969) also obtained the same result of Lomize. By the factor f used in Equation (1.5), the cubic law can be written as follows.

$$q = \frac{C}{f} d^3 \Delta h \tag{1.6}$$

where q is the volumetric flow rate, Δh is the difference of hydraulic head and C is a constant that depends on the flow geometry and fluid properties.

Witherspoon *et al.* (1980) investigated the validity of the cubic law for the flow in a closed fracture where the surfaces are in contact and the aperture is being decreased under stress. Consequently, they showed that the cubic law is found valid whether the fracture surfaces are held open or are being closed under stress; the effect of deviations from the ideal parallel plates concept only cause an apparent reduction in flow and are taken care of by the factor f as shown in Equation (1.6). Furthermore, they showed that f varied from 1.04 to 1.65 for their experiments. In addition, Barton *et al.* (1985) and Barton (1986) represented a fracture aperture empirically by *JRC* and *JCS*, and modified the cubic law to take into account the fracture surface roughness.

In contrast to the above researches, which were conducted by the physical experiments, the following researches were conducted by the theoretical analysis or the numerical or physical simulation. Walsh (1981) derived the Laplace's equation for two-dimensional steady state flow assuming the changes in aperture are sufficiently small. By solving the equation, he showed that the permeability reduction factor for a contacting fracture can be described by $(\alpha-1)/(\alpha+1)$, where α is the ratio of the contact area to the total area of the fracture.

On the other hand, Tsang (1984) simulated the two-dimensional fluid flow by using equivalent electrical circuits. In this simulation, the variation of the apertures in a rough fracture was modeled by the electrical resistors with different resistance values placed on a two-dimensional grid, and the resistance values were set in inverse proportion to the cubic of fracture aperture. Consequently, he found that the more small aperture there are in the aperture distribution, the larger is the effect of tortuosity, and the flow rate becomes two or three order smaller than the predicted value by the parallel plates model.

Furthermore, in order to investigate the deviation from the cubic law, Brown (1987, 1989) performed a number of numerical flow simulations for the fractures that are numerically generated by using a fractal model of fracture surface topography. He calculated the pressure distribution and flow vectors in the fractures by solving the Reynolds equation, which describes laminar flow between slightly nonplanar and nonparallel surfaces, by the finite difference method. Consequently, he found that the surface topography has little effect at large separations, and the flow is tortuous at small separations, tending to be channeled through high-aperture regions. He also showed that the parameter most affecting fluid flow through fractures is the ratio of the mean separation between the surfaces to the rms (root-mean-square) surface height, and the variations in the fractal dimension produce only a second-order effect on the fluid flow.

Tsang and Tsang (1987) also showed the fluid flow through fractures to be channeled. They proposed a channel model for the flow through a fracture by characterizing the channel by an aperture density distribution and a spatial correlation length, and showed the validity of their model by confirming the calculated tracer breakthrough curves correspond well with the experimental data. Zimmerman *et al.* (1991) also solved the Reynolds equation by using lubrication theory assuming that the fracture aperture has sinusoidal variation, and obtained the similar results to those found by Brown. In addition to the above researches, many pieces of research have been conducted (see Gangi, 1978; Kranz *et al.*, 1979; Walsh and Grosenbaugh, 1979; Walsh, 1981; Tsang and Witherspoon, 1981). Most of them have investigated the stress dependency of fluid flow through fractures, because the aperture and contact area of the fractures considerably depend on the stress acting on the fracture surface.

1.3. The objectives and the outline of this thesis

As mentioned first, the surface properties of a fracture play an important roll on its mechanical and hydrological properties. The surface properties can be represented by the geometric and material properties of the fracture surfaces. The material properties can be estimated from those of the ambient rock, but the geometric properties can not be determined so easily, because the geometry of fracture surfaces is very complex. Therefore, some difficulties are always accompanied in determining the parameters, such as surface roughness, that depend on the surface geometry. For example, although the surface roughness was determined by *JRC* or rms-height in the above researches, these parameters are not unique for the fracture surfaces, because they have strong size dependency. Therefore, an experimental approach is necessary to evaluate the surface roughness by these parameters.

On the other hand, fractal approach is useful to evaluate the surface roughness. The concept of fractal was first presented by Mandelbrot in 1967 to characterize the complex shapes in nature. It has been used widely in scientific research. Also in rock mechanics, fractal has often been used to characterize the geometric surface properties of a fracture since Brown and Scholz (1985b) and Power *et al.* (1987) showed that the topography of natural rock surfaces is fractal in a very wide range of length, that is, from 10^{-5} m to 10^{5} m. However, many pieces of early research applying fractal to rock mechanics did not understand that most of the fracture surfaces are not self-similar fractal but self-affine fractal. In consequence, they misunderstood the scaling law of the fracture surfaces. Furthermore, they often used the fractal dimension, which is one of the fractal parameter, to quantify the surface roughness (e.g. Lee *et al.*, 1990). However, owing to the several researches, it cleared that fractal dimension should be a scaling parameter rather than a roughness parameter (see Power *et al.*, 1988; Power and Tullis, 1991). In addition, it has also cleared that another fractal parameter called steepness in this thesis can be a roughness parameter (see Odling, 1994; Murata and Saito, 1997). Therefore, the surface roughness and its size effect, scaling law, can be evaluated reasonably by a fractal model that can be represented by the fractal dimension and the steepness.

Thus, the geometric properties of a fracture surface can be represented well by the fractal model. Consequently, the surface properties that have been estimated experimentally and ambiguously can be estimated reasonably, and the mechanical and hydrological properties of a rock fracture can be characterized well.

Based on this concept, the objectives of this thesis are 1) to discuss the problems of variogram method in order to make a precise fractal model of a fracture surface, 2) to present a new method to evaluate the surface roughness of a fracture surface and discuss the size effect of the surface roughness based on this method, 3) to clear the contact condition of a fracture surface to apply the new method properly and 4) to represent a fracture permeability by the fractal model and investigate the geometric effect of a fracture surface on the fracture permeability.

In chapter 2, it is shown that the rock fracture is a self-affine fractal, and typical methods to make a fractal model of it will be reviewed. Among them, the variogram method is mathematically discussed concerning to its problem that the lag where the fractal model can be determined is very small. This problem has been recognized phenomenally, but the cause of it has not been explained theoretically until this work is published (Murata and Saito, 1999). Furthermore, some items that must be paid attention to apply the variogram method are discussed.

In chapter 3, the original concept of JRC-diagram is presented to evaluate the surface roughness of a fracture considering its size effect. The JRC-diagram is a self-similar fractal model represented by the variogram method and based on the correlation between *JRC* and steepness. In order to check the validity of this method, the *JRC* and peak shear strength are evaluated for several specimens and compared with the experimental results.

In chapter 4, the changes of geometric properties and contact condition of fracture surfaces with the progress of shearing are investigated to clear the contact condition of a fracture surface and to apply the JRC-diagram to the fracture surfaces of various conditions. From the results of this investigation, the shear mechanism of a fracture surface is also discussed.

In chapter 5, in order to develop a more reasonable evaluation method of fracture permeability, first, several single-fracture specimens that has different fractal parameters are prepared, and their permeability are measured under the hydrostatic pressure to investigate the relation between the permeability and the fractal parameters; and second, based on the fractal model, a theoretical equation representing the deviation from the cubic law of fracture permeability is presented, and the effect of the fractal parameters on the deviation is also discussed.

In chapter 6, based on the discussion in chapter 5, the tortuosity of fluid flow through a fracture is investigated experimentally and numerically.

In chapter 7, the results obtained from this study are summarized.

References

Bandis, S., A. C. Lumsden, and N. R. Barton, Experimental studies of scale effects on the shear behavior of rock joints, *Int. J. Rock. Mech. Min. Sci. & Geomech. Abstr.*, Vol. 18, 1-21, 1981.

Barton, N., Review of a new shear strength criterion for rock joints, *Engineering Geology*, Vol. 7, 287-332, 1973.

Barton, N. and V. Choubey, The shear strength of rock joints in theory and practice, *Rock Mechanics*, Vol. 10, 1-54, 1977.

Barton, N., S. Bandis, and K. Bakhtar, Strength, deformation and conductivity coupling of rock joints, *Int. J. Rock Mech. Min. Sci. & Geomech. Abstr.*, Vol. 22, 121-140, 1985.

Barton, N. R., Deformation phenomena in jointed rock, *Geotechnique*, Vol. 36, 147-167, 1986.

Brown, S. R. and C. H. Scholz, Closure of random elastic surfaces in contact, *J. Geophys. Res.*, Vol. 90, 5531-5545, 1985a.

Brown, S. R. and C. H. Scholz, Broad bandwidth study of the topography of natural rock surfaces, *J. Geophys. Res.*, Vol. 90, 12575-12582, 1985b.

Brown, S. R. and C. H. Scholz, Closure of rock joints, *J. Geophys. Res.*, Vol. 91, 4939-4948, 1986.

Brown, S. R., Fluid flow through rock joints: the effect of surface roughness, *J. Geophys. Res.*, Vol. 92, 1337-1347, 1987.

Brown, S. R., Transport of fluid and electric current through a single fracture, *J. Geophys. Res.*, Vol. 94, 9429-9438, 1989.

Gangi, A. F., Variation of whole and fractured porous rock permeability with confining pressure, *Int. J. Rock Mech. Min. Sci. & Geomech. Abstr.*, Vol. 15, 249-257, 1978.

Greenwood, J. A. and J. B. P. Williamson, Contact of nominally flat surfaces, *Proc. R. Soc. London*, Vol. A295, 300-319, 1966.

Greenwood, J. A. and J. H. Tripp, The contact of two nominally flat rough surfaces, *Proc. Instn. Mech. Engrs.*, Vol. 185, 625-633, 1971.

Kranz, R. L., A. D. Frankel, T. Engelder, and C. H. Scholz, The permeability of whole and jointed Barre granite, *Int. J. Rock Mech. Min. Sci. & Geomech. Abstr.*, Vol. 16, 225-234, 1979.

Ladanyi, B. and G. Archambault, Simulation of shear behavior of a jointed rock mass, *Proc. 11th Symp. on Rock Mech.*, Vol. 1, 105-125, 1970.

Lee, Y. H., J. R. Carr, D. J. Barr, and C. J. Haas, The fractal dimension as a measure of the roughness of rock discontinuity profiles, *Int. J. Rock Mech. Min. Sci. & Geomech. Abstr.*, Vol. 27, 453-464, 1990.

Lomize, G. M., Flow in fractured rocks (*in Russian*), 127 pp., *Geosenergoizdat*, Moscow, 1951.

Louise, C., A study of groundwater flow in jointed rock and its influence on the stability of rock masses, *Rock Mech. Res. Rep.*, 10, 90 pp., Imp. Coll., London, 1969.

Murata, S. and T. Saito, Evaluation of rock joint surface roughness by using fractal model (*in Japanese*), *Sigen-to-Sozai*, Vol. 113, 555-560, 1997.

Murata, S. and T. Saito, The variogram method for a fractal model of a rock joint surface, *Geotechnical and Geological Engineering*, Vol. 17, 197-210, 1999.

Odling, N. E., Natural fracture profiles, fractal dimension and joint roughness coefficients, Rock Mech. Rock Eng., Vol. 27, 135-153, 1994.

Patton, F. D., Multiple modes of shear failure in rock, *Proc. 1st ISRM Congr.*, Lisbon, Vol. 1, 509-513, 1966.

Plesha, M. E., Constitutive models for rock discontinuities with dilatancy and surface degradation, *Int. J. Numer. and Anal. Methods Geomech.*, Vol. 11, 345-362, 1987.

Plesha, M. E. and B. C. Haimson, Key questions in rock mechanics, *Proc. 29th U.S. Symp. on Rock Mech.*, Vol. 1, 119-126, 1988.

Power, W. L., T. E. Tullis, S. R. Brown, G. N. Boitnott, and C. H. Scholz, Roughness of natural fault surfaces, *Geophys. Res. Lett.*, Vol. 14, 29-32, 1987.

Power, W. L., T. E. Tullis, and J. D. Weeks, Roughness and wear during brittle faulting, *J. Geophys. Res.*, Vol. 93, 15,268-15,278, 1988.

Power, W. L. and T. E. Tullis, Euclidean and fractal models for the description of rock surface roughness, *J. Geophys. Res.*, Vol. 96, 415-424, 1991.

Rowe, P. W., L. Barden, and I. K. Lee, Energy components during the triaxial cell and direct shear test, *Geotechnique*, Vol. 14, 247-261, 1964.

Swan, G., Tribology and the characterization of rock joints, *Proc. 22nd U.S. Symp. on Rock Mech.*, Vol. 1, 432-437, 1981.

Swan, G., Determination of stiffness and other joint properties from roughness measurements, *Rock Mech. Rock Eng.*, Vol. 16, 19-38, 1983.

Swan, G. and S. Zongqi, Prediction of shear behavior of joints using profiles, *Rock Mech. Rock Eng.*, Vol. 18, 183-212, 1985.

Tsang, Y. W. and P. A. Witherspoon, Hydromechanical behavior of a deformable rock fracture subject to normal stress, *J. Geophys. Res.*, Vol. 86, 9287-9298, 1981.

Tsang, Y. W. and P. A. Witherspoon, The dependence of fracture mechanical and fluid flow properties on fracture roughness and sample size, *J. Geophys. Res.*, Vol. 88, 2359-2366, 1983.

Tsang, Y. W., The effect of tortuosity on fluid flow through a single fracture, *Water Resour. Res.*, Vol. 20, 1209-1215, 1984.

Tsang, Y. W. and C. F. Tsang, Channel model of flow through fractured media, *Water Resour. Res.*, Vol. 23, 467-479, 1987.

Walsh, J. B. and M. A. Grosenbaugh, A new model for analyzing the effect of fractures on compressibility, *J. Geophys. Res.*, Vol. 84, 3532-3536, 1979.

Walsh, J. B., Effect of pore pressure and confining pressure on fracture permeability, *Int. J. Rock Mech. Min. Sci. & Geomech. Abstr.*, Vol. 18, 429-435, 1981.

Walsh, J. B. and W. F. Brace, The effect of pressure on porosity and the transport properties of rock, *J. Geophys. Res.*, Vol. 89, 9425-9431, 1984.

Witherspoon, P. A., J. S. Y. Wang, K. Iwai, and J. E. Gale, Validity of cubic law for fluid flow in a deformable rock fracture, *Water Resour. Res.*, Vol. 16, 1016-1024, 1980.

Yamada, K., N. Takeda, J. Kagami, and T. Naoi, Surface density of asperities and real distribution of asperity heights on rubbed surfaces, *Wear*, Vol. 47, 5-20, 1978a.

Yamada, K., N. Takeda, J. Kagami, and T. Naoi, Mechanism of elastic contact and friction between rough surfaces, *Wear*, Vol. 48, 15-34, 1978b.

Yoshioka, N. and C. H. Scholz, Elastic properties of contacting surfaces under normal and shear loads 1. Theory, *J. Geophys. Res.*, Vol. 94, 17681-17690, 1989a.

Yoshioka, N. and C. H. Scholz, Elastic properties of contacting surfaces under normal and shear loads 2. Comparison of theory with experiment, *J. Geophys. Res.*, Vol. 94, 17691-17700, 1989b.

Zimmerman, R. W., S. Kumar, and G. S. Bodvarsson, Lubrication theory analysis of the permeability of rough-walled fractures, *Int. J. Rock Mech. Min. Sci. & Geomech. Abstr.*, Vol. 28, 325-331, 1991.

CHPTER2

FRACTAL MODEL OF A FRACTURE SURFACE BY USING VARIOGRAM METHOD

2.1. Introduction

Mechanical and hydrological properties of fractures in rock mass are considered dependent on their geometric surface properties such as surface roughness. Therefore, many pieces of research to investigate the geometric surface properties of the fractures quantitatively have been conducted (see Renger, 1970; Swan and Zongqi, 1985; Brown and Scholz, 1985; Power and Tullis, 1991). They took mainly statistical approaches until the topography of a fracture surface was suggested to be fractal. Since then, however, a fractal approach has been tried extensively, because it can describe well the complex topography of a fracture surface by a simple fractal model independent of the fracture size. The fractal model is generally formulated by a power law and several methods to make it have been presented. Among them, the variogram method is especially often used, because it can make a precise fractal model by simple calculation compared to the other methods. For the variogram method, the fractal model is determined by a straight line on the log-log plot of the semi-variogram function to the lag. The lag is a distance between the two data points used for the semi-variogram calculation. In this thesis, this plot will be called a variogram plot. On the variogram plot, however, the range of lag where the straight line is observed is very short, that is, less than 10% of the profile length (Huang *et al.*, 1992). This problem has been recognized phenomenally, but the cause of it has not been clarified yet.

Therefore, first, the fractal of a fracture surface is explained and the some methods to make a fractal model are reviewed. Second, the detail of variogram method is explained and the cause of the problem as mentioned above is clarified mathematically. Third, the range of lag where the straight line is observed on the variogram plot is estimated based on the theoretical calculation. Forth, the fact that the range of straight line increases with an increase in the profile length is demonstrated by applying the variogram method to the profile generated by the Fourier filtering method. Finally, the matters that demand special attention to make a fractal model by using the variogram method are also discussed.

According to the results of recent researches, the topography of a fracture

surface is commonly multifractal (e.g. Schmittbuhl et al., 1995). Therefore, a multifractal approach should be taken for a strict discussion, but we will take a monofractal approach here. This is because the monofractal approach is simple on the mathematical treatment, and for the problem of the variogram method, the multifractal is not a main cause of the problem as discussed in the following section.

2.2. Fractal of fracture surfaces

2.2.1 Self-similar fractal and self-affine fractal

It has been shown that most of the complex geometry in nature is fractal and the topography of a fracture surface is also fractal (Mandelbrot, 1983). The most important property of the fractal geometry is self-similarity or self-affinity. It defines the scaling law for the geometry by a simple power law. The self-similarity and the self-affinity are defined as follows (Peitgen and Saupe, 1988; Xie, 1993):

Suppose S_i $(i = 1, 2, ..., N)$ is N number of non-overlapping subsets of a set S, and S_i is obtained by transformation groups T_i from S:

$$S_i = T_i S,$$

where the transformation groups T_i could be associated with parallel translation, rotation, stretching, shearing and similarity. If T_i is only a similar transformation group, S is a self-similar set. On the other hand, if T_i is an affine transformation, S is a self-affine set. Moreover, if T_i is especially a diagonal affine transformation, S is a diagonal self-affine set.

Thus, fractal can be classified into self-similar fractal and self-affine fractal. An example of the self-similar fractal and the self-affine fractal are shown in Figure 2.1(a) and 2.1(b) respectively. On these figures, the box part of the upper profile is enlarged to be the lower profile with enlargement factor indicated beside the lower graph. The lower profile looks similar to the upper profile. As shown in Figure 2.1(a), in the case of the self-similar fractal, the enlarged profile looks similar to the original one when the enlargement factors for both horizontal and vertical directions are equal. On the other hand, in the case of the self-affine fractal, the enlargement factors for each direction must be different to make the enlarged profile look similar to the original one as shown in Figure 2.1(b).

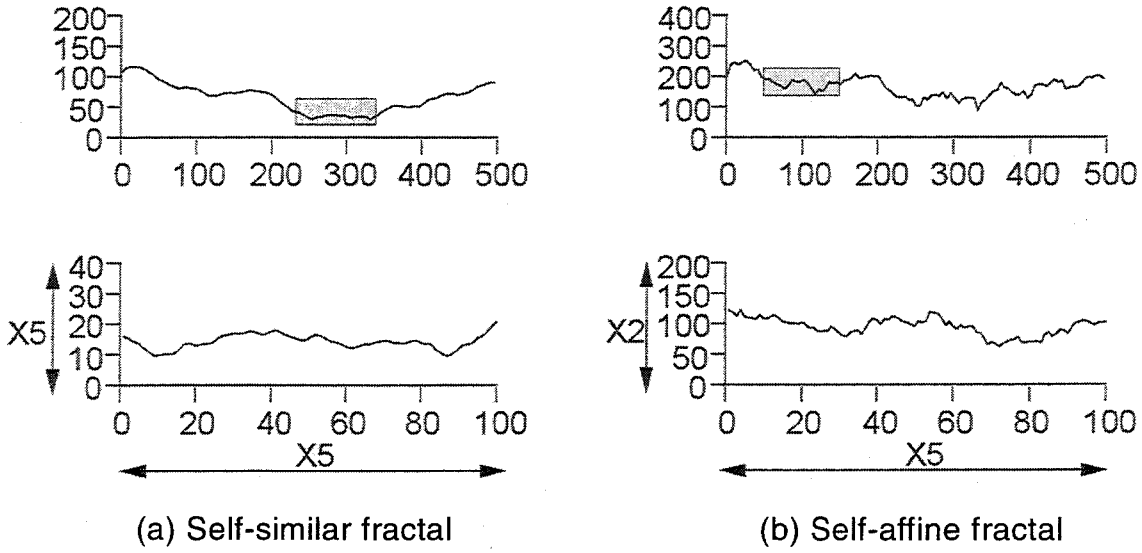

(a) Self-similar fractal (b) Self-affine fractal

Figure 2.1: Self-similar fractal (a) and self-affine fractal (b). For each case, the box part of the upper profile is enlarged to the lower profile. In the case of self-similar fractal, enlargement factors are equal in both horizontal and vertical directions if the enlarged profile looks similar to the original one. On the other hand, in the case of self-affine fractal, the factors are different if the enlarged profile looks similar to the original one.

2.2.2 Fractal of a fracture surface and the methods to make a fractal model

Generally, the profile of a fracture surface is a fractional Brownian motion, fBm (see Mandelbrot, 1983; Peitgen and Saupe, 1988). The fBm is a non-differentiable single-valued function, $B_f(t)$. The increment of this function, $B_f(t_2)$-$B_f(t_1)$, has the following relation to the increment of t, t_2-t_1

$$\left\langle \left| B_f(t_2) - B_f(t_1) \right|^2 \right\rangle \propto \left| t_2 - t_1 \right|^{2H} \qquad (0 < H < 1) \tag{2.1}$$

where < > is an expectation operator and H is a constant called Hurst exponent. From Equation (2.1), it is implicit that the increment of $B_f(t)$, $\Delta B_f(t)$, is r^H times when t is scaled r times. This scaling property of fBm can be described as

$$\left\langle \Delta B_f(rt)^2 \right\rangle \propto r^{2H} \left\langle \Delta B_f(t)^2 \right\rangle \qquad (0 < H < 1) \tag{2.2}$$

Therefore, it is deduced that the profile of a fracture surface is a diagonal self-affine fractal as shown in Figure 2.1(b) and the fracture surface looks smoother as it is observed widely.

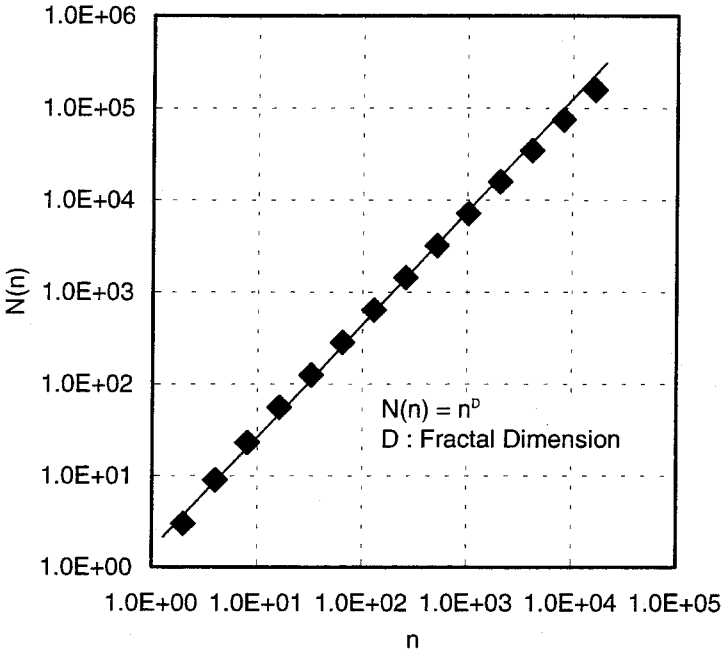

Figure 2.2: An example of log-log plot for the box-counting methods. The horizontal axis, n, is the number of division to the side of the largest box that contains a whole profile, and the vertical axis, $N(n)$, is the number of boxes intersecting the profile. For the fractal profile, the relation between n and $N(n)$ is represented as $N(n)=n^D$, where D is the fractal dimension.

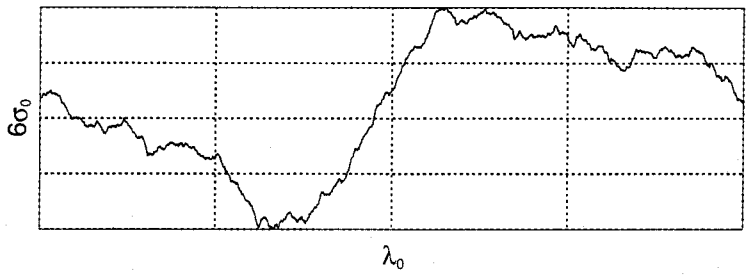

Figure 2.3: Illustration of the boxes used in the modified box-counting method. The profile is just surrounded by the rectangle which has length λ_0 and height $\approx 6\sigma_0$, where λ_0 and σ_0 correspond to the profile length and the standard deviation of height distribution of the profile respectively. The rectangle is divided into n^2 boxes with the same aspect ratio as the large rectangle.

For a self-affine fractal, the fractal model is generally made by the box-counting method, spectral method, variogram method, etc. The box-counting method is usually implemented by covering a self-similar profile with a grid of identical square boxes and counting the number of boxes intersecting the profile as a function of the box size. After that, the function is plotted in a log-log space. If the plot is linear, the slope of this curve is related to the fractal dimension (e.g. Mandelbrot, 1983; Peitgen and Saupe, 1988). An example of this log-log plot is shown in Figure 2.2. This plot is for the profile shown in Figure 2.3 that has a fractal dimension of 1.2. According to Brown (1995), however, the box-counting method must be modified for a self-affine profile to overcome the problem of crossover length that happens inherently for the self-affine fractal. Brown suggested the following modification to make a grid of rectangular box. First, draw a rectangle around the profile, which has length λ_0 and height $6\sigma_0$, so that the rectangle is completely filled by the profile, where λ_0 and σ_0 correspond to the profile length and the standard deviation of height distribution of the profile respectively. Second, divide the large rectangle into n^2 boxes with the same aspect ratio as the large rectangle (see Figure 2.3). However, the box-counting method does not work sufficiently well for the self-affine profile even with this modification (Kulatilake *et al.*, 1995). On the other hand, the spectral method is implemented by calculating the power spectral density of the profile as a function of a spatial frequency (or a wave number), then plotting the function in a log-log space and evaluating the fractal dimension from the linearity of this curve. The spectral method is not bothered by the problem of crossover length. However, it shows too noisy power spectral density to get a precise result (as shown in Figure 2.4) without stacking the power spectral densities of many profiles. Compared with these methods, the variogram method is based on the definition of self-affine fractal and presents a good result by simple calculation even from one profile. Therefore, this method is often used these days. However, this method also has a problem mentioned in the introduction and this problem yields a number of additional problems on the application of this method (Kulatilake *et al.*, 1998). In the next section, we will explain the variogram method more theoretically before the discussion about the cause of the problem.

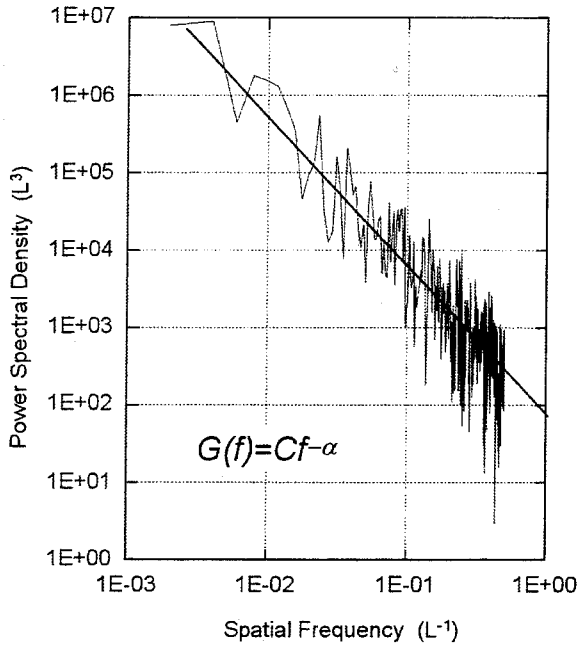

Figure 2.4: Log-log plot of power spectral density of fracture surface. As shown in this figure, the power spectral density is too noisy to yield a precise fractal model without stacking the power spectral density of many profiles.

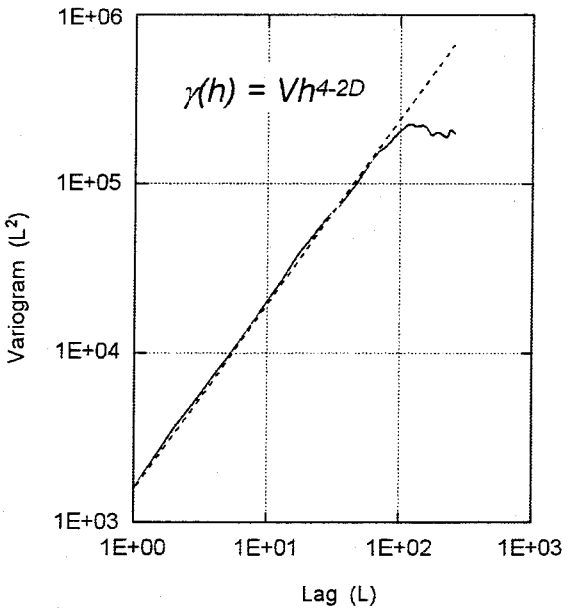

Figure 2.5: Fractal model by using the variogram method. The fractal model is described by a power law, so that it can be determined from the straight line of the variogram plot. The fractal dimension and the proportional constant are determined from the slope and the intersection of the straight line respectively.

2.3 Variogram method

2.3.1 Mathematical expression of variogram method

The variogram method yields a fractal model from a straight line appearing on the variogram plot as shown in Figure 2.5. Remember that the variogram plot is the log-log plot of the semi-variogram function to the lag. The semi-variogram function is often used in geostatistics to generate a correlation model of data in random space and defined to be

$$\gamma(h) = \frac{1}{2}\left\langle \left| z(x) - z(x+h) \right|^2 \right\rangle \tag{2.3}$$

where $z(x)$ is the data value of point x and h is the lag that is the distance between the two data points. In addition, < > indicates the expectation operator. For the profile of a fracture surface, $z(x)$ represents the height of profile at measuring point x, and h is the distance between two measuring points. The semi-variogram function is practically calculated from the experimental semi-variogram function described in Equation (2.4).

$$\gamma(h) = \frac{1}{2N}\sum_{i=1}^{N}\left[z(x_i) - z(x_i + h) \right]^2 \tag{2.4}$$

where N is the number of pairs of data whose lag is h. We will call the experimental semi-variogram function simply 'variogram' in this thesis.

On the other hand, the variogram can be described by the autocorrelation function, $C(h)$ as shown in Equation (2.5).

$$\begin{aligned} \gamma(h) &= \frac{1}{2}\left\langle \left| z(x) - z(x+h) \right|^2 \right\rangle \\ &= \frac{1}{2}\left\{ \left\langle z(x+h)^2 \right\rangle - 2\left\langle z(x)z(x+h) \right\rangle + \left\langle z(x)^2 \right\rangle \right\} \\ &= C(0) - C(h) \end{aligned} \tag{2.5}$$

Moreover, when the profile is fractal, the power spectral density function of the profile of a fracture surface, $G(f)$, can be described by Equation (2.6) (see Brown and Scholz, 1985, Power and Tullis, 1991).

$$G(f) = Cf^{-\alpha} \qquad (1 < \alpha < 3) \tag{2.6}$$

where f is a spatial frequency; C and α are constants.

The autocorrelation function is related to the power spectral density function

by Wiener-Khintchine relation as

$$C(h) = \int_0^\infty G(f)\cos(2\pi hf)df \tag{2.7}$$

Therefore, substituting Equation (2.6) into Equation (2.7), and calculating the right hand side of Equation (2.5), then

$$\begin{aligned}\gamma(h) &= C(0) - C(h) \\ &= \int_0^\infty Cf^{-\alpha}(1-\cos(2\pi hf))df \\ &= 2\int_0^\infty Cf^{-\alpha}\sin^2(\pi hf)df \\ &= 2C(\pi h)^{\alpha-1}\int_0^\infty u^{-\alpha}\sin^2 u du\end{aligned} \tag{2.8}$$

where $u = \pi hf$. The last integral in the right hand side of Equation (2.8) is a constant. Therefore, replacing the all constant terms of this equation with V,

$$\gamma(h) = Vh^{\alpha-1} \qquad (1<\alpha<3) \tag{2.9}$$

Using the relation between the fractal dimension, D, and the constant of power of Equation (2.6), α,

$$D = \frac{5-\alpha}{2} \tag{2.10}$$

Equation (2.9) can be rewritten by using fractal dimension as

$$\gamma(h) = Vh^{4-2D} \tag{2.11}$$

Thus, the fractal model of a fracture surface can be uniquely described by a simple power law determined by the constant, V and the fractal dimension, D. Considering that this equation has been derived without any assumption (except that the topography of a fracture surface is monofractal) and has no restriction on the range of lag, the power law must be valid everywhere on the variogram plot as long as the profile of fracture surface is monofractal. Actually, however, the power law is recognized only for a very small lag. This range of lag is very short compared to the profile length. For the main purpose of this work, we will discuss the cause of this short range of lag mathematically in the next section.

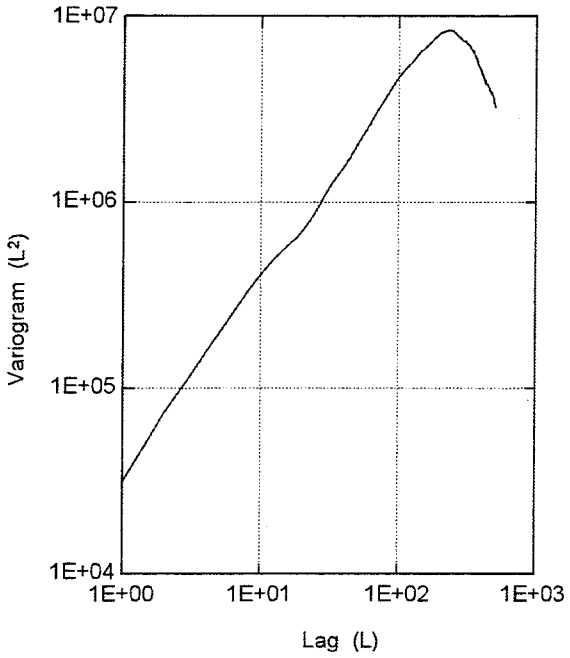

Figure 2.6: The variogram plot for a fractal profile generated by Fourier filtering method. As shown in this figure, the variogram plot sometimes has the negative slope for the large lag. This negative slope can not appear on the variogram plot if the profile is fractal.

2.3.2 The problem of variogram method and its causes

As shown in the previous section, the power law is theoretically satisfied everywhere on the variogram plot, but it is not actually. It has been recognized that the range of lag for the straight line appearing on the variogram plot is less than about 10% of the profile length. Concerning the cause of this problem, one might think that the profile of a fracture surface is not monofractal but multifractal. This idea may be right, but it is not a main cause for this problem. Because the variogram of a fractal profile must increase with an increase in the lag and the negative slope (as shown in Figure 2.6), which is sometimes observed for large lag on the variogram plot, can not appear even if the profile is multifractal. Therefore, in this section, we will discuss another cause of the problem.

Theoretically, the profile length is infinite and the sampling interval is infinite small, but actually the profile length and the sampling interval for a sampled profile are finite. Therefore, the integral interval of Equation (2.7) must be (f_{min}, f_{max}) for the actually sampled profile, where $1/f_{min}$ corresponds to the profile length, λ, and $1/f_{max}$

corresponds to the twice of sampling interval according to the sampling theorem. Thus, Equation (2.7) can be written as

$$C(h) = \int_{f_{\min}}^{f_{\max}} G(f)\cos(2\pi hf)df \tag{2.12}$$

Judging from Equation (2.6), $G(f)$ is very small when f is large. Therefore, the integral interval of Equation (2.12) can be extended to (f_{min}, ∞) without significant error. Integrating Equation (2.12) for this extended integral interval,

$$\begin{aligned} C(h) &= \int_{f_{\min}}^{\infty} G(f)\cos(2\pi hf)df \\ &= C\left[\frac{\lambda^{\alpha-1}\pi^{\alpha-0.5}\left(\frac{h}{\lambda}\right)^{\alpha-1}\Gamma\left(\frac{1-\alpha}{2}\right)}{2\Gamma\left(\frac{\alpha}{2}\right)}\right. \\ &\left. + \frac{\lambda^{\alpha-1}\,{}_pF_q\left\{(0.5-0.5\alpha);0.5,(1.5-0.5\alpha);-\left(\pi\frac{h}{\lambda}\right)^2\right\}}{\alpha-1}\right] \end{aligned} \tag{2.13}$$

where λ is the profile length, α is a constant of power described in Equation (2.6). In addition, ${}_pF_q\{\ \}$ is the hypergeometric function and $\Gamma\{\ \}$ is the gamma function.

Power series expansion of the hypergeometric function in Equation (2.13) is

$$\begin{aligned} &{}_pF_q\left\{(0.5-0.5\alpha);0.5,(1.5-0.5\alpha);-\left(\pi\frac{h}{\lambda}\right)^2\right\} \\ &= 1 + a_1\left(\pi\frac{h}{\lambda}\right)^2 + a_2\left(\pi\frac{h}{\lambda}\right)^4 + \cdots \end{aligned} \tag{2.14}$$

where a_1, a_2, ... are the constant depending on α. Judging from Equation (2.14), if

$$\frac{h}{\lambda} << 1 \tag{2.15}$$

then the value of hypergeometric function is nearly one. Therefore, in this case, Equation (2.13) can be rewritten to

$$C(h) = C\left[\frac{\lambda^{\alpha-1}\pi^{\alpha-0.5}\left(\frac{h}{\lambda}\right)^{\alpha-1}\Gamma\left(\frac{1-\alpha}{2}\right)}{2\Gamma\left(\frac{\alpha}{2}\right)} + \frac{\lambda^{\alpha-1}}{\alpha-1}\right] \tag{2.16}$$

On the other hand,

$$\begin{aligned} C(0) &= \int_{f_{\min}}^{\infty} G(f)df \\ &= \frac{C}{\alpha-1}\lambda^{\alpha-1} \end{aligned} \tag{2.17}$$

Substituting Equation (2.16) and (2.17) into Equation (2.5),

$$\begin{aligned} \gamma(h) &= C(0) - C(h) \\ &= -C\frac{\pi^{\alpha-0.5}\Gamma\left(\frac{1-\alpha}{2}\right)}{2\Gamma\left(\frac{\alpha}{2}\right)}h^{\alpha-1} \\ &= Vh^{\alpha-1} \qquad (V:\text{constant}) \end{aligned} \tag{2.18}$$

Thus, the same power law with Equation (2.9) can be derived.

From the above discussion, it was clarified that the power law is valid for the finite profile length when the lag satisfies the condition of Equation (2.15). Therefore, we can conclude that the problem of the variogram method is mainly caused by the limitation of the sampled profile length. Moreover, it can be concluded that the condition of Equation (2.15) is satisfied when the range of lag is less than 10% of the profile length, as has been recognized phenomenally.

2.4 Discussion

2.4.1 The range of lag where the power low is valid

In order to confirm exactly what range of lag satisfies the condition of Equation (2.15), the value of the hypergeometric function described in Equation (2.14) was plotted to the lag, h. Figure 2.7 shows the result of this plot when α is 2.0, 2.2, 2.4, 2.6, 2.8, 2.99 considering that α is usually from 2.0 to 3.0 for the profile of a fracture surface. In this figure, it is noted that the profile length, λ, is 100 for every α. From this figure, it can be confirmed that the value of the

hypergeometric function is approximately one and the condition of Equation (2.15) is satisfied when the lag is less than 10% of the profile length. In addition, it can also be recognized that the range of lag decreases with an increase in α. These results agree with the experimental results performed by Kulatilake *et al.* (1998). Therefore, the accurate range of lag for the variogram method can be estimated from Figure 2.7 according to α or fractal dimension that is related to α by Equation (2.10).

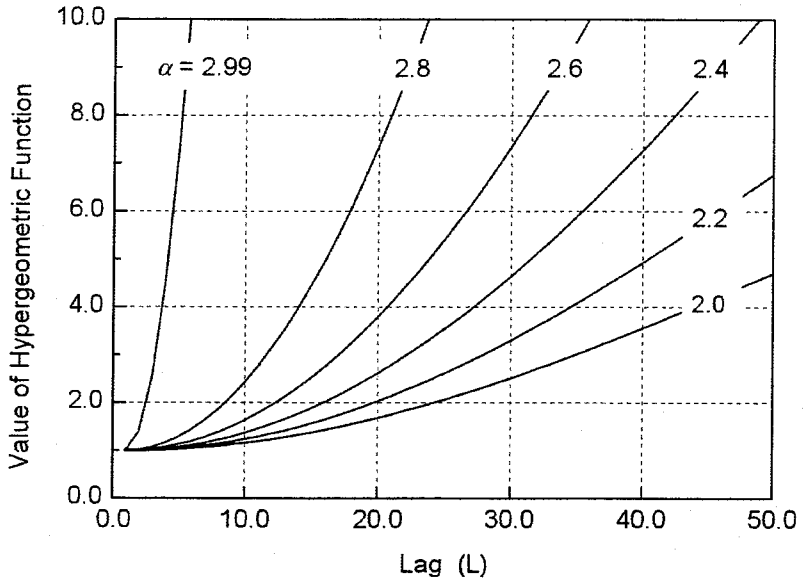

Figure 2.7: The plot of the hypergeometric function of Equation (2.14). The value of the hypergeometric function is approximately one only for the small lag. In addition, the range of lag decreases with increasing α.

Furthermore, to confirm that the range of lag satisfying the power law increases with an increase in the profile length, the variogram method was applied to the profiles cut from a long profile. A long profile whose length is 16834L was generated by Fourier filtering method as shown in Figure 2.8, and three profiles whose lengths are 16384L, 2048L and 512L respectively were cut from this long profile. Here, L is a unit of length. The fractal dimension of this profile is 1.2, that is, α = 2.6. For these three profiles, the variogram plots were drawn in Figure 2.9 after the linear trend was removed. In this figure, the range of lag satisfying the power law was also indicated for each variogram plot. From Figure 2.9, it can be reconfirmed that the range of lag satisfying the power law increases with an

increase in the profile length. Moreover, it can be recognized that the ranges of lag where the power law is satisfied are about 600L, 70L and 6L for the profiles whose length are 16834L, 2048L and 512L respectively. They are within 5% of the profile length as it is estimated from Figure 2.7 according to α.

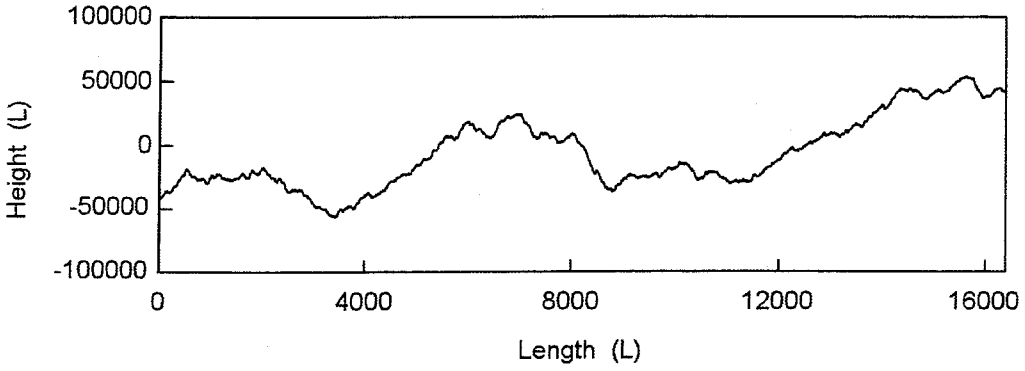

Figure 2.8 : The long profile generated by Fourier filtering method. The fractal dimension of this profile is 1.2, that is, $\alpha = 2.6$.

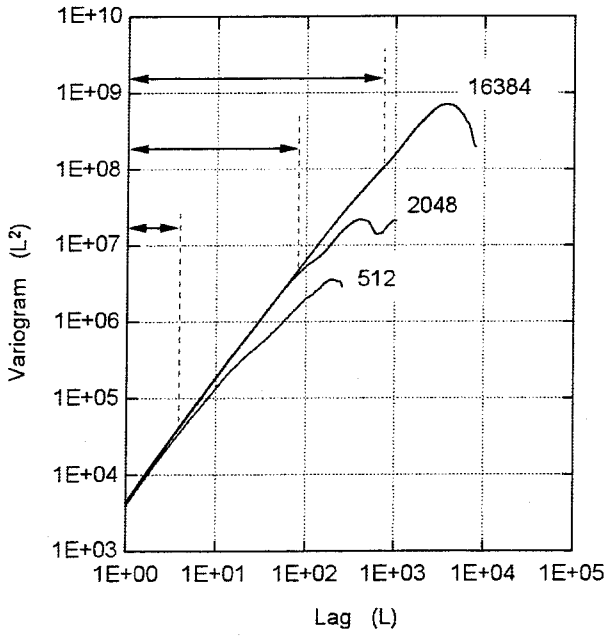

Figure 2.9 : The variogram plots of the profiles cut from the long profile drawn in Figure 6. Each of these profiles has a different profile length. The range of lag satisfying the power law increases with increasing the profile length. The range is within 5% of the profile length that can be evaluated from Figure 2.7.

2.4.2 The matters that require special attention for the variogram method

Considering the above discussion, two matters that require special attention on making a fractal model by using the variogram method can be thought.

The first matter is the profile length and the sampling interval. According to the above discussion, the problem of the variogram method is inevitable as long as the sampled profile length is finite. Judging from the Figure 2.7, the smaller the lag is, the better the estimation is, but the variogram data points are too few to make a good estimation in this case. In addition, although the effect of sampling interval on the suitable range of lag was ignored in the above discussion, according to Kulatilake *et al.* (1998), the denser the data density is, the smaller the minimum suitable lag is. Therefore, the sufficiently long profile and the sufficiently small sampling interval are recommended to make a precise fractal model.

The second matter is the removal of the linear trend. From Equation (2.1), we can derive the following relation for the fBm profile supposing $B_f(0)=0$ (Falconer, 1990).

$$\left\langle (B_f(t)-B_f(0))(B_f(t+h)-B_f(t)) \right\rangle = \frac{1}{2}\left\{(t+h)^{2H}-t^{2H}-h^{2H}\right\} \tag{2.19}$$

Hence the value of Equation (2.19) is positive or negative according to whether $H>1/2$ or $H<1/2$. If $H>1/2$ then $B_f(t)-B_f(0)$ and $B_f(t+h)-B_f(t)$ tend to be of the same sign, so that $B_f(t)$ tends to increase if it has an increasing tendency. Similarly, if $H<1/2$ then $B_f(t)-B_f(0)$ and $B_f(t+h)-B_f(t)$ tend to be of opposite sign, so that $B_f(t)$ tends to undulate.

Considering that $H>1/2$ for most of the profiles of fracture surfaces, the profile has inherently increasing or decreasing tendency. This tendency can be a component of the linear trend of the profile. Another component of the linear trend is induced by sampling a profile. It depends on how to set the base line for the sampling. Hence, the sampled profile has two components of linear trend. To make a precise fractal model, only the latter linear trend must be removed, but it is impossible to do so because we can not estimate the amount of the former linear trend and distinguish it from the latter linear trend. Consequently, we are forced to remove these two components of the linear trend to do a consistent evaluation for any profile.

Therefore, it must be noted that the removal of linear trend may cause an error for the estimation of fractal dimension. For the variogram method, the fractal

dimension will be estimated as smaller if the profile inherently has a decreasing tendency. This is because the removal of the linear trend will make the slope of the variogram plot increase. Similarly, the fractal dimension will be estimated as larger if the profile inherently has an increasing tendency.

2.5. Conclusions

It has been clarified mathematically that the problem with the variogram method is mainly caused by the fact that the sampled profile has a finite length. This result was confirmed by demonstrating that the range of lag satisfying the power law increases with an increase in the profile length. Moreover, in this work, it was also clarified that the range of lag decreases with a decrease in the fractal dimension of the profile. Furthermore, a sufficiently long profile sampled with sufficiently small sampling interval is necessary to make a precise fractal model. The removal of the linear trend of the profile can also cause an error in the evaluation of the fractal dimension for the variogram method, although it is necessary for the consistent evaluation.

These results of this work will be helpful when applying the variogram method to make a precise fractal model of a fracture surface. The monofractal approach has been assumed. A more correct discussion based on the multifractal approach should be conducted if research on the multifractal nature of the fracture surfaces advances much more.

References

Brown, S. R. and C. H. Scholz, Broad bandwidth study of the topography of natural rock surfaces, *J. Geophys. Res.*, Vol. 90, 12575-12582, 1985b.

Brown, S. R., Measuring the dimension of self-affine fractal: example of rough surfaces, In *Fractal in the Earth Sciences*, Barton, C. C. and La Point, P. R. (eds), Ch. 4. Plenum Press, New York, 77-87, 1995.

Falconer, K., *Fractal Geometry*, Ch. 16. John Wiley & Sons, 1990.

Huang, S. L., S. M. Oelfke and R. C. Speck, Applicability of fractal characterization and modeling to fracture profiles, *Int. J. Rock Mech. Min. Sci. & Geomech. Abstr.*, Vol. 29, 89-98, 1992.

Kulatilake, P. H. S. W., G. Shou, T. H. Huang and R. M. Morgan, New peak shear strength criteria for anisotropic fractures, *Int. J. Rock Mech. Min. Sci. & Geomech. Abstr.*, Vol. 32, 673-697, 1995.

Kulatilake, P. H. S. W., J. Um and G. Pan, Requirements for accurate quantification of self-affine roughness using the variogram method, *Int. J. Solids and Structures*, Vol. 35, 4167-4189, 1998.

Mandelbrot, B. B., *The fractal geometry of nature,* W. H. Freeman and Company, New York, 1983.

Peitgen, H. -O. and D. Saupe, *The science of fractal images*, Ch. 1, Springer-Verlag, New York, 1988.

Power, W. L. and T. E. Tullis, Euclidean and fractal models for the description of rock surface roughness, *J. Geophys. Res.*, Vol. 96, 415-424, 1991.

Rengers, N., Influence of surface roughness on the friction properties of rock planes, *Proc. of 2nd Congress of I.S.R.M.*, Vol. 1, Beograd, 229-234, 1970.

Schmittbuhl, J., F. Schmitt and C. H. Scholz, Scaling invariance of crack surfaces, *J. Geophys. Res.*, Vol. 100, 5953-5973, 1995.

Swan, G. and S. Zongqi, Prediction of shear behavior of joints using profiles, *Rock Mech. Rock Eng.*, Vol. 18, 183-212, 1985.

Xie, H., *Fractals in rock mechanics*, Ch. 2. A. A. Balkema, Rotterdam, 1993.

CHPTER3

EVALUATION OF SURFACE ROUGHNESS AND MECHANICAL PROPERTIES OF ROCK FRACTURE BY USING A FRACTAL MODEL

3.1. Introduction

The mechanical properties of a rock fracture considerably depend on its surface properties as mentioned in chapter 1. Therefore, many pieces of research have been carried out to estimate them, especially the shear properties, from the surface properties (e.g. Patton, 1966; Ladanyi and Archambault, 1970; Barton, 1973; Barton and Choubey, 1977; Bandis *et al.*, 1981; Swan and Zongqi, 1985). Barton (1973) presented a following empirical equation to estimate the peak shear strength, τ, using *JRC* (Joint Roughness Coefficient) and *JCS* (Joint Wall Compressive Strength), which are respectively the roughness and material parameters of a fracture.

$$\tau = \sigma_n \tan\left[JRC \log_{10}\left(\frac{JCS}{\sigma_n}\right) + \phi_b \right] \tag{3.1}$$

where σ_n is the effective normal stress acting on the joint surface and ϕ_b is the basic friction angle that is a friction angle between flat surfaces. For weathered joints, residual fiction angle, ϕ_r, is used instead of ϕ_b (see Barton and Choubey, 1977). This equation is adopted by ISRM (1978) as a suggested method to estimate the peak shear strength of a rock fracture. However, *JRC* is a considerably subjective parameter, because it is determined by comparing the profile of a fracture surface with the JRC-profiles as shown in Figure 3.1.

In order to overcome this problem, Tse and Cruden (1979) investigated the correlation between the several statistical parameters such as rms-height and *JRC*. Consequently, they found that Z_2 defined by Myers (1962) and *SF* (Structure Function) defined by Sayles and Thomas (1977) correlate with *JRC* best. However, these parameters can not determine a unique fracture roughness, because they are dependent on the fracture size.

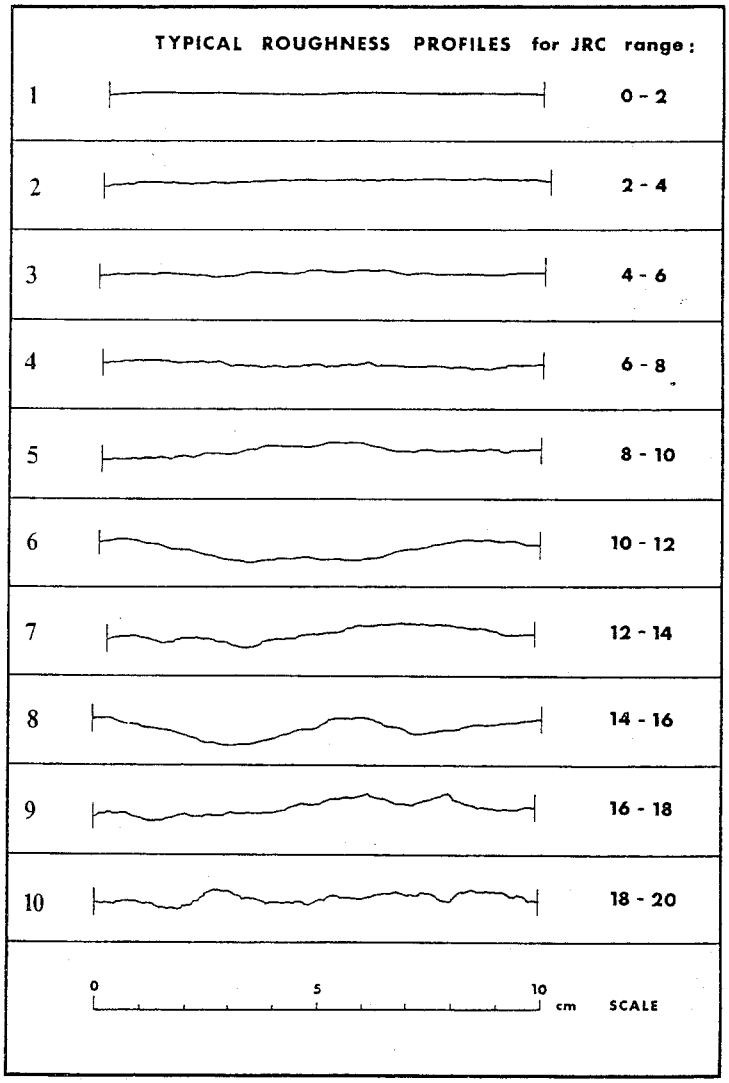

Figure 3.1: JRC-profiles. (After Barton and Choubey, 1977)

Therefore, fractal dimension has often been used for this purpose since Brown and Scholz (1985) showed that the topography of fracture surface is fractal in the wide range of size. This is because the fractal dimension is a scale invariant parameter and it has been thought to be a roughness parameter. For example, Lee *et al.*, (1990) investigated the fractal dimension of JRC-profiles in order to determine *JRC* by the fractal dimension. Consequently, they obtained a good correlation. However, the calculated fractal dimension of the JRC-profiles ranges from 1.000446 to 1.013435 and this

range of fractal dimension may be the same order of measurement or calculation errors. This nearly one of fractal dimension is often calculated when the divider method is used for the profile of a rock fracture. The divider method is implemented by dividing a profile with an identical divider length, r_i, and counting the number of divisions, N_i, as a function of r_i. After that, the function is plotted on a log-log plot. Since the relation, $N_i=Cr_i^{-D}$ (C is a proportional constant), is valid for the fractal geometry, the fractal dimension, D, can be determined from the slope of the linear part of this curve (see Mandelbrot, 1983; Peitgen and Saupe, 1988). According to Brown (1987, 1995), however, the divider method cannot yield a correct fractal dimension for a self-affine profile, if the divider length is larger than the crossover length. In such the case, obtained fractal dimension is nearly one. In addition, the crossover length is theoretically estimated from 10^{-8} m to 10^{-5} m for natural fractures. Such a small divider length is impossible for a practical application of this method. From these reasons, the result of Lee *et al.* is probably incorrect. Furthermore, it was clarified by several researches that fractal dimension should be a scaling parameter rather than a roughness parameter (see Power *et al.*, 1988; Power and Tullis, 1991).

In this chapter, in order to evaluate the roughness of a fracture surface, a new original concept of JRC-diagram is presented. The JRC-diagram is a self-similar fractal model determined by the variogram method. By using this diagram, the *JRC* and its size effect can be evaluated theoretically. In order to check the validity of JRC-diagram, the *JRC* is estimated for several specimens and compared with *JRC* determined from JRC-profiles, and then, the peak shear strength is estimated and compared with the experimental results.

3.2. Fractal model and steepness by variogram method

As shown in chapter 2, the variogram function, $\gamma(h)$, is represented by the following equation for a self-affine fractal.

$$\gamma(h) = Vh^{2H} \qquad (1 < H < 1) \tag{3.2}$$

where V is a proportional constant and H is the Hurst exponent that is related to the fractal dimension, D, by the following equation.

$$D = 2 - H \tag{3.3}$$

Equation (3.2) is the fractal model represented by variogram method. It can be uniquely determined by the proportional constant, V, and the fractal dimension, D.

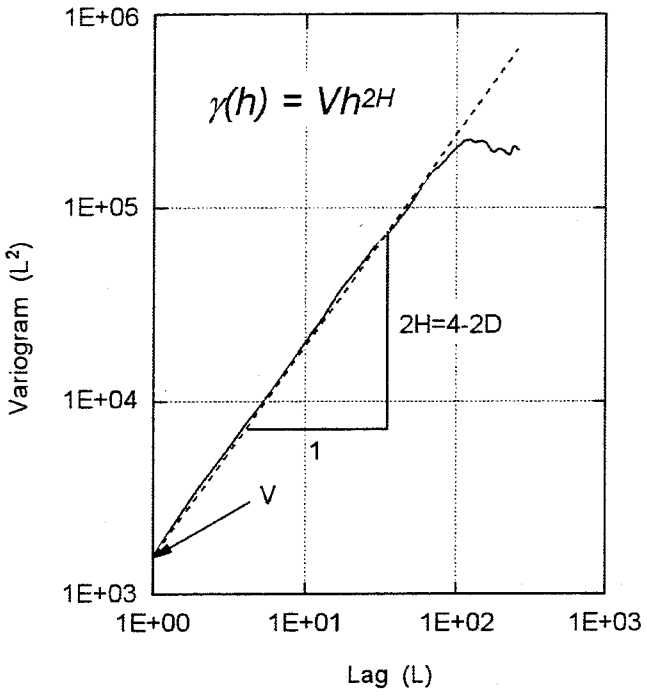

Figure 3.2: Fractal model by using the variogram method. The fractal model is described by a power law that is a straight line on the variogram plot. The fractal dimension, $D=2-H$, and proportional constant, V, are determined from the slope and intersection of the straight line respectively.

These two parameters can be determined by the intersection and slope of a straight line appearing on the variogram plot respectively as shown in Figure 3.2.

For the profile of a fracture surface, the variogram function is practically calculated from the following experimental semi-variogram function.

$$\gamma(h) = \frac{1}{2N}\sum_{i=1}^{N}[z(x_i) - z(x_i + h)]^2 \tag{3.4}$$

where N is the number of pairs of data whose lag is h, and $z(x)$ is the profile height at measuring point x. From Equation (3.4), it is explicit that the value of $\gamma(h)$ is large when the mean height difference between the two data points on the profile is large, that is to say, when the mean slope angle of the profile is large. In addition, from Equation (3.2), it is explicit that the profile of large V has larger $\gamma(h)$ than that of small V for arbitrary h, if H is same for the profiles. Therefore, it can be said that the parameter, V, represents the mean slope angle of a profile and has a close

relation with the roughness of a fracture surface. In this thesis, V is called steepness and defined by the value of variogram function at the unit lag ($h=1$).

On the other hand, from Equation (3.2) and (3.3), it can be said that the fractal dimension is a scaling parameter that represents how the steepness or the roughness changes according to the lag. Therefore, the roughness of a fracture surface can be estimated with it size effect quantitatively by the fractal model, if the roughness is purely determined by the geometry of a fracture surface. For this purpose, it is easy to investigate the correlation between the steepness and a popular roughness parameter such as *JRC*.

3.3. The correlation between steepness and *JRC*

As mentioned above, *JRC* is one of the most popular roughness parameter and it is related to the peak shear strength by Equation (3.1). Therefore, if a good correlation between the steepness and *JRC* is obtained, *JRC* of a fracture surface can be estimated considering its size effect objectively. Furthermore, the peak shear strength can be estimated by the obtained *JRC*. Based on this concept, the correlation between the steepness and *JRC* was investigated.

First, the JRC-profiles were magnified by a copy machine, and the 256 points of height data were digitized with the sampling interval of 0.337mm from each JRC-profile. Consequently, the JRC-profiles of 86mm long were obtained. Although the obtained profiles are shorter than the original JRC-profiles, their length is more than 85% of the original length, and they can be thought to keep the original geometric properties. Second, the variogram plots were made for each JRC-profile as shown in Figure 3.3. From this figure, as discussed in Chapter 2, it can be recognized that the power law is valid only for the range of lag that is less than 10% of the profile length. Therefore, the steepness and fractal dimension of each JRC-profile can be respectively obtained from the intersection and slope of the straight line determined from the linear part of the variogram plot by using least square method. However, it must be noted that the fractal dimension can be determined uniquely from the slope of the straight line, but the steepness depends on the unit lag. Therefore, the definition of the unit lag is necessary to determine the steepness. Here, 1mm that is a unit of length was adopted for a unit lag because of the convenience for the profile measurement and variogram calculation.

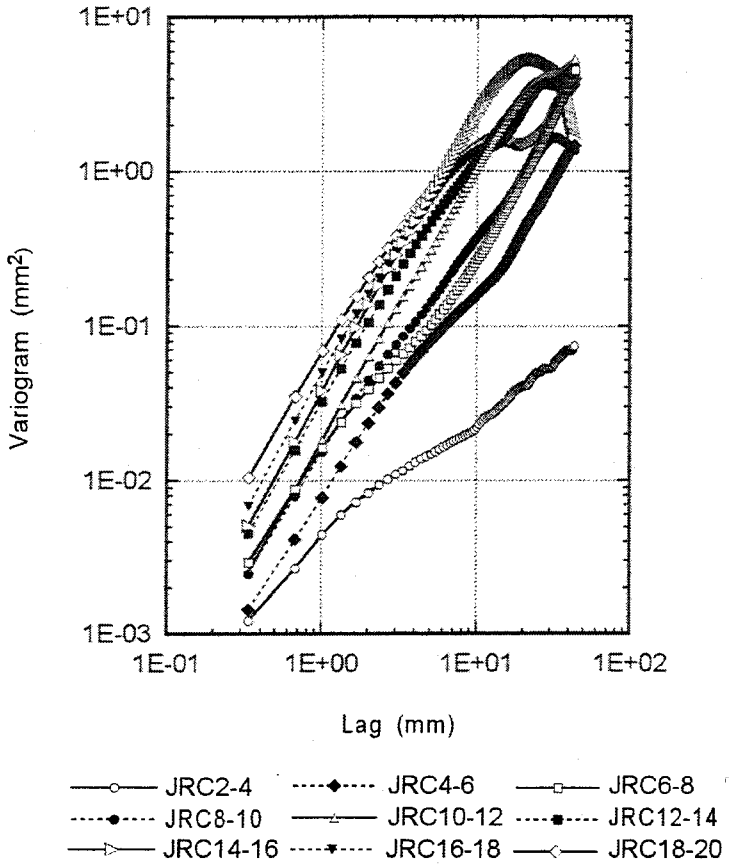

Figure 3.3: The variogram plot of JRC-profiles. In this figure, the linear relation between the variogram and lag distance can be seen in the small lag distance that is less than 10% of the profile length.

Table 3.1: Steepness and fractal dimension of JRC-profile.

JRC	Steepness	Fractal Dimension
JRC2-4	4.055E-03	1.600
JRC4-6	7.656E-03	1.303
JRC6-8	1.271E-02	1.462
JRC8-10	1.459E-02	1.276
JRC10-12	1.986E-02	1.106
JRC12-14	2.489E-02	1.211
JRC14-16	3.589E-02	1.101
JRC16-18	4.150E-02	1.230
JRC18-20	6.516E-02	1.261

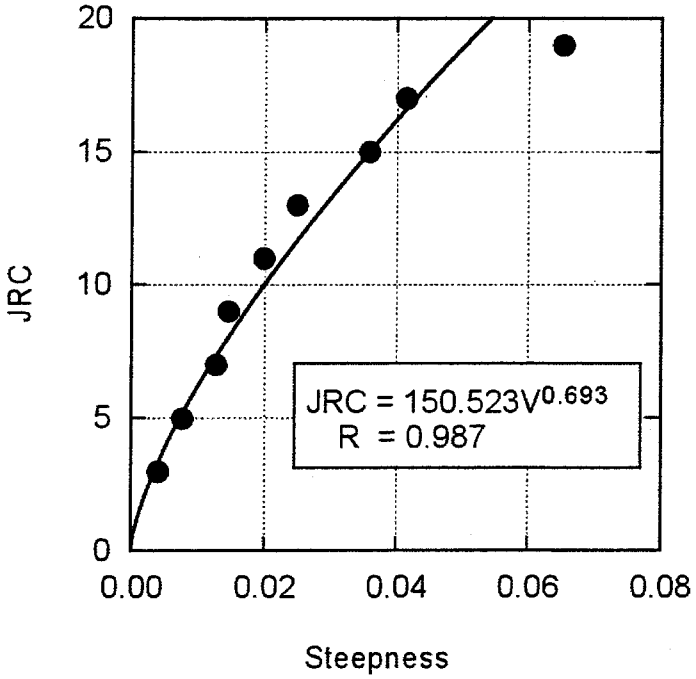

Figure 3.4: Relation between *JRC* and steepness. There is a good correlation between the two parameters as indicated in this figure with the correlation factor, R, of 0.987.

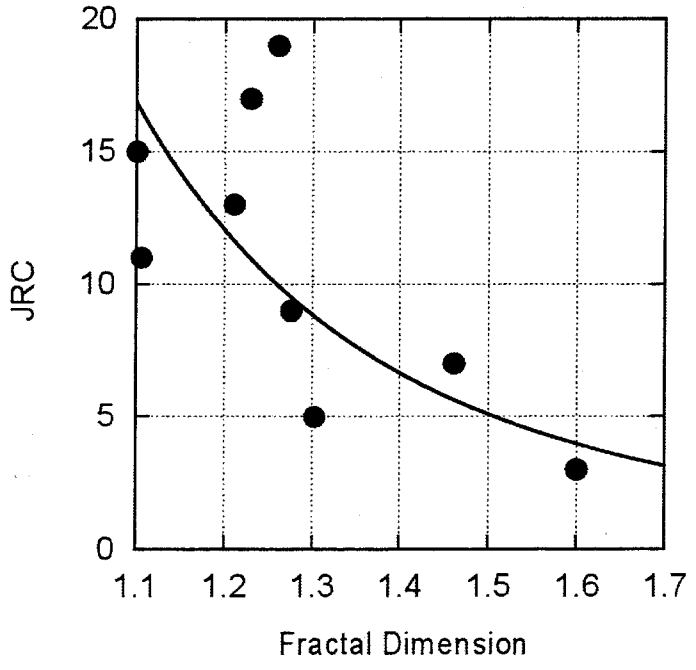

Figure 3.5: Relation between *JRC* and fractal dimension. There is no clear correlation between the two parameters.

Thus, the steepness and fractal dimension of each JRC-profile were obtained. They are shown in Table 3.1. Furthermore, *JRC* was plotted to the obtained steepness and fractal dimension. They are shown in Figure 3.4 and Figure 3.5 respectively. In these figures, *JRC* is the middle value of the range that the JRC-profile indicates, for example, *JRC=3* for the JRC2-4. Figure 3.4 shows a considerably good correlation between *JRC* and the steepness. It is,

$$JRC = 150.523V^{0.693} \tag{3.5}$$

and the correlation coefficient is greater than 0.98. On the other hand, the clear correlation between *JRC* and the fractal dimension can not be recognized from Figure 3.5. However, the tendency that the fractal dimension decreases with the increase in *JRC* can be seen. The same tendency of fractal dimension was also obtained by Odling (1994) and Kulatilake *et al.* (1995). Therefore, it can be thought that this tendency is not caused by the errors of magnification, digitizing and so on.

Many researchers (*e.g.* Lee *et al.*, 1990) have believed that the profile of large fractal dimension is rougher than that of small fractal dimension. However, the results obtained here support the concept that steepness and fractal dimension are a roughness and scaling parameter respectively. Therefore, based on this concept, the method to evaluate the *JRC* and its size effect will be discussed next.

3.4. Estimation of rock fracture surface roughness by using JRC-diagram

3.4.1. JRC-diagram

A good correlation between *JRC* and the steepness determined by the unit lag of 1mm was obtained as Equation (3.5). However, the curves of the variogram plots for each JRC-profile cross each other as shown in Figure 3.3. Therefore, it is explicit that the obtained correlation is invalid for the other unit lag. In other words, the roughness of JRC-profiles changes according to the size. This means that the JRC-profiles can not be used for estimating the roughness of the profiles whose length is different from the original JRC-profiles, that is, about 10cm. This is because the JRC-profiles are typical rough profiles copying from the surface of natural rock joints, and they are self-affine profiles that have a different scaling law (fractal dimension) each other. Therefore, if the fractal models of the JRC-profiles are replaced with the self-similar fractal models having an identical *JRC*, a unique correlation between *JRC* and the steepness can be determined. In addition, it can be

used for estimating the surface roughness of any size.

The self-similar fractal does not change its apparent shape with the change in its size, because it keeps the statistical similarity to the similar transformations. From Equation (2.2), the Hurst exponent of self-similar fractal must be one. Thus, the fractal model of self-similar fractal can be written as

$$\gamma(h) = Vh^2 \tag{3.6}$$

Therefore, on the variogram plot, parallel straight lines whose slope is two represent the self-similar fractal models of different steepness. If the parallel straight lines are drawn to take the steepness shown in Table 3.1 or calculated by using Equation (3.5), they represent the corresponding self-similar fractal models of JRC-profiles. The self-similar fractal model of a JRC-profile is called JRC-model in this thesis. The JRC-models for some *JRC* values are drawn in Figure 3.6, and the author calls this figure JRC-diagram.

By the way, it is not clear whether the values of steepness shown in Table 3.1 have the best correlation with *JRC* or not, because the correlation changes with the unit lag. However, the Equation (3.5) will not yield a significant error to the JRC-diagram, because it has a sufficiently good correlation coefficient. Moreover, the 1mm of unit lag is convenient for the practical variogram calculation. Therefore, Equation (3.5) is used for the JRC-diagram to estimate *JRC* according to the steepness.

In Figure 3.6, the fractal model of an artificial fracture surface and a natural fracture surface of granite are also drawn. The artificial fracture surface was made by Brazilian test and the natural fracture surface was sampled from a tunneling site. The profiles of these fracture surfaces are shown in Figure 3.7. The steepness and fractal dimension of them are 5.620E-03 and 1.339 respectively for the artificial fracture surface and 1.105E-03 and 1.149 respectively for the natural fracture surface. As shown in Figure 3.6, the fractal models of these fracture surfaces cross the JRC-model of smaller *JRC* with the increase in lag. This is because those fracture surfaces are self-affine fractal and the slope of their fractal model is less than two. Therefore, this figure quantitatively shows that the roughness of a fracture surface decreases with the increase in size. Thus, if the fractal model of a fracture surface is drawn on the JRC-diagram, the *JRC* of the fracture surface can be estimated with its size effect.

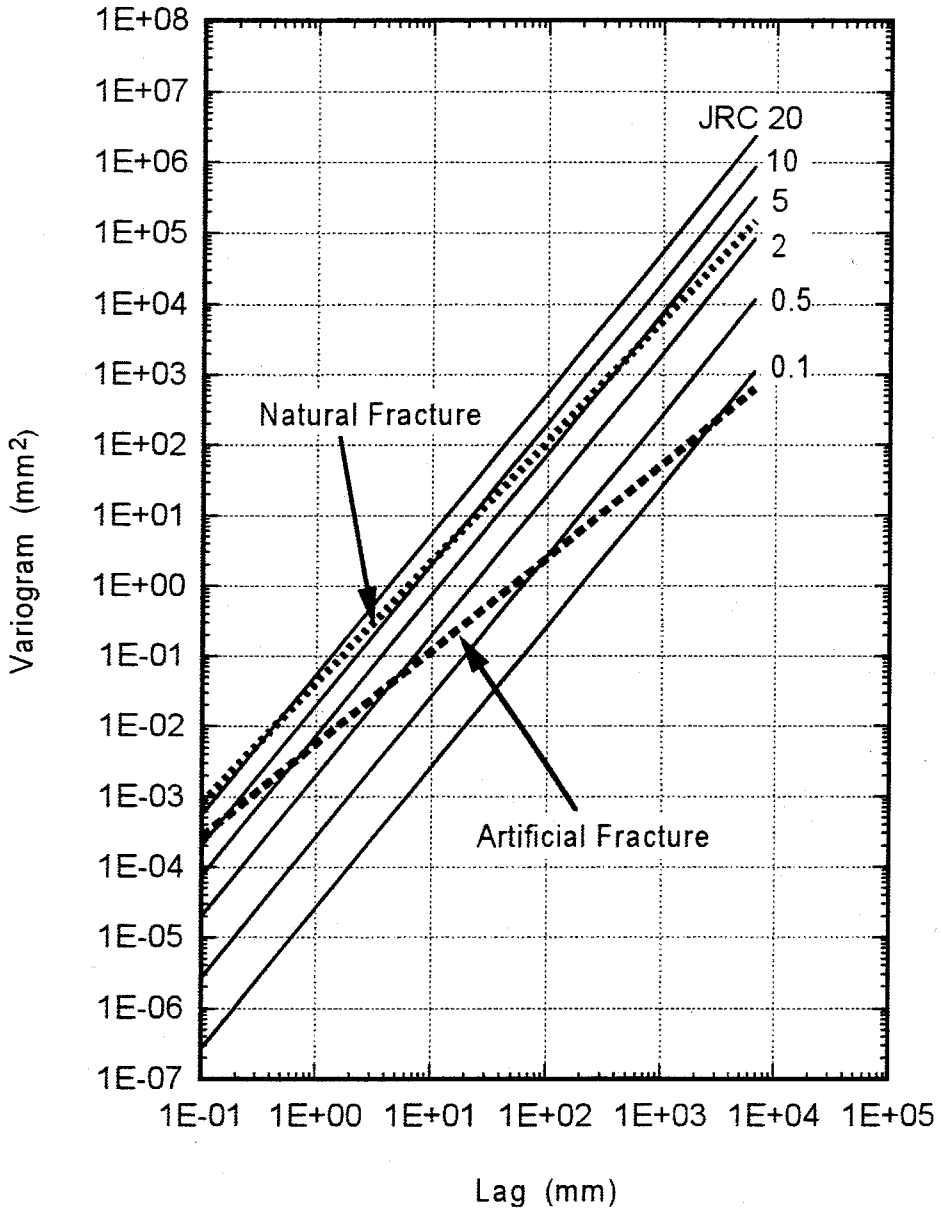

Figure 3.6: JRC-diagram that is a self-similar fractal model determined by the variogram method. The fractal models both of the artificial fracture and the natural fracture are also plotted on this diagram. The fractal models of these fractures cross the JRC-model of smaller *JRC* with the increase in lag.

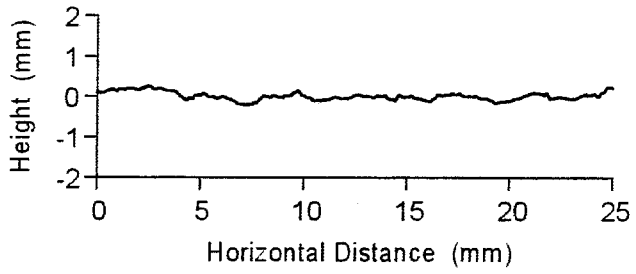

(a) A surface profile of the artificial fracture

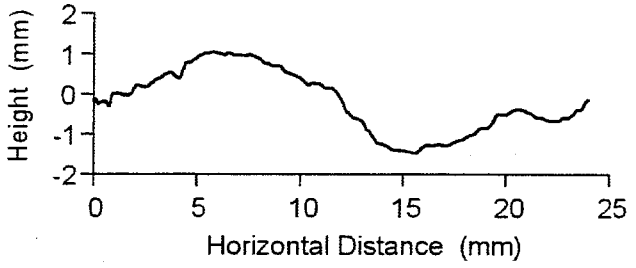

(b) A surface profile of the natural fracture

Figure 3.7: Surface profiles of the artificial fracture (a) and the natural fracture (b). The artificial fracture surface was made by Brazilian test and the natural fracture surface was sampled from a tunneling site.

3.4.2. Control size

As mentioned above, the size-dependent roughness of a fracture surface can be estimated by using the JRC-diagram. However, it is necessary to know what size of lag should be used for the estimation. Here, the author calls this lag a control size and proposes a concept to determine it.

The facing two surfaces of a rock fracture usually contact each other at several points on the interlocking asperities. Among the interlocking asperities, the steepest asperity mainly affects the shear strength. From Equation (3.2) and (3.4), the tangent of mean slope angle of a fracture surface profile can be written as a function of h, that is,

$$\frac{\sqrt{\gamma(h)}}{h} = \sqrt{V} h^{H-1} \qquad (0 < H < 1) \tag{3.7}$$

From this equation, it is explicit that the mean slop angle of a fracture surface profile increases with the decrease in profile length. Therefore, it can be supposed

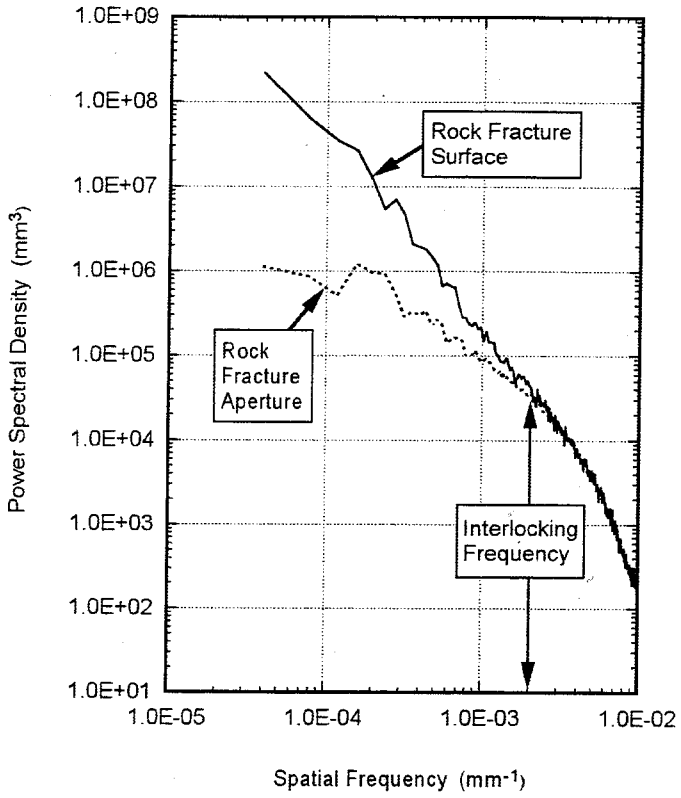

Figure 3.8: The log-log plot of the PSD function of surface profile and aperture profile for the artificial rock fracture shown in Figure 3.7. The PSD function of the aperture profile is smaller than that of the surface profile in the spatial frequency that is smaller than the interlocking frequency.

that the small asperities have steeper slope than the large asperities and the smallest asperity directly affects the shear strength. For this reason, it is reasonable to think that *JRC* should be estimated by the lag that is equal to the size of the smallest interlocking asperity.

Brown and Scholz (1985) found that the power spectral density (PSD) function of an aperture profile is smaller than that of a surface profile in the lower spatial frequency than the 'interlocking frequency' as shown in Figure 3.8. The aperture profile can be obtained by subtracting the summation of upper and lower block height from the sample block height as explained in Figure 3.9. In addition, the interlocking frequency is defined by Murata and Saito (1997) as the spatial frequency where the discrepancy of PSD function between the surface profile and the aperture profile begins to be observed.

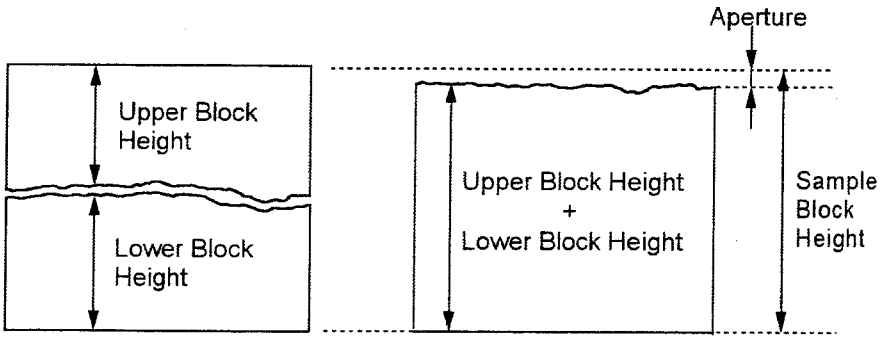

Figure 3.9: Aperture profile of a rock fracture. Aperture profile of a rock fracture can be obtained by subtracting the sum of upper block height and lower block height from the sample block height.

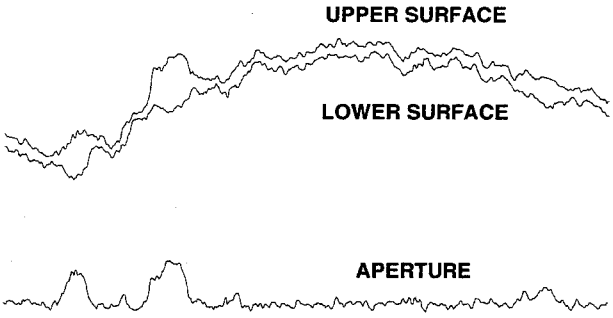

Figure 3.10: The surface profile and the aperture profile of a rock fracture. The large undulation is disappeared on the aperture profile.

The reason why the discrepancy is observed can be explained as follows. The amplitude of large asperities is larger than that of small asperities on a fracture surface, and the larger asperities on facing two fracture surfaces are usually interlocking each other. Therefore, the larger asperities that have longer wavelength than a certain wavelength is disappeared on the aperture profile as shown in Figure 3.10. Consequently, the PSD function of the aperture profile is smaller than that of the surface profile below the interlocking frequency, which corresponds to the inverse of the smallest wavelength among the disappeared wavelength. This smallest wavelength is called interlocking wavelength here. Thus, the interlocking wavelength should be first obtained as the control size, and then *JRC* is estimated at the control size by using the JRC-diagram.

By the way, in the non-interlocking frequency region, the PSD function of the aperture profile is twice that of the surface profile, because the phase difference between the facing two surfaces is random. Therefore, in Figure 3.8, the PSD function of aperture profile is shown by 1/2 of the original one to indicate the interlocking frequency clearly.

Figure 3.8 shows the PSD functions of surface profile and aperture profile for the artificial fracture mentioned above. From this figure, the discrepancy of the PSD function between the surface profile and the aperture profile can be observed in the spatial frequency smaller than $0.002\mu m^{-1}$. Therefore, the interlocking frequency of this fracture can be estimated as $0.002\mu m^{-1}$ and the interlocking wavelength is 500 (=1/0.002)μm. Furthermore, *JRC* of the artificial fracture surface can be estimated by the following procedure. First, determine the steepness of the JRC-model that has the same variogram value with the fractal model of the fracture surface; second, calculate *JRC* by substituting the obtained steepness into Equation (3.5). Thus, the estimated *JRC* is 5.75 for this fracture surface.

Generally, it is difficult to measure the aperture profile for a natural fracture. However, owing to the advance in coring technique, non-disturbed cores can be obtained from highly fractured formations in these days. Therefore, the aperture profile can be measured from such the non-disturbed core, and the proposed method to estimate the *JRC* will be effective for the natural fracture.

3.4.3. Size effect of *JRC*

As mentioned above, the fractal model of a fracture surface crosses the JRC-models of smaller *JRC* with the increase in lag. Therefore, as shown in Figure 3.11, the next equation can be derived from the relation between the JRC-model and the fractal model of a fracture surface.

$$\frac{\log(V_n h_n^2) - \log(V_0 h_0^2)}{\log h_n - \log h_0} = 2H$$
$$\therefore \quad V_n = V_0 \left(\frac{h_n}{h_0} \right)^{2H-2} \tag{3.8}$$

where V_0 and V_n are the steepness of the JRC-models that cross the fractal model at the control size of h_0 and h_n respectively. In addition, from Equation (3.5), JRC_0 and JRC_n, which are the *JRC* values estimated at the control sizes of h_0 and h_n respectively, are represented as follows.

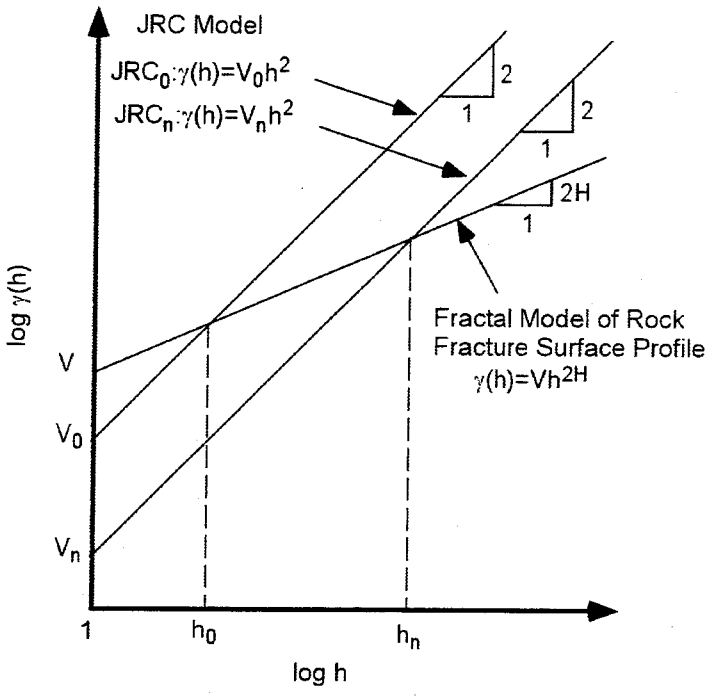

Figure 3.11: Relation between the JRC-model and the fractal model of a rock fracture surface profile.

$$\begin{cases} JRC_0 = 150.523V_0^{0.693} \\ JRC_n = 150.523V_n^{0.693} \end{cases} \tag{3.9}$$

Eliminating V_0 and V_n from Equation (3.8) and (3.9), the next equation is derived.

$$JRC_n = JRC_0\left(\frac{h_n}{h_0}\right)^{0.693(2H-2)} \tag{3.10}$$

This equation has the same style with the experimental equation presented by Barton and Choubey (1977), Bandis *et al.* (1981) and Barton *et al.* (1985) to predict the size effect of *JRC*, that is,

$$JRC_n = JRC_0\left(\frac{L_n}{L_0}\right)^{-0.02JRC_0} \tag{3.11}$$

where L_0, and JRC_0 are the length and *JRC* of original JRC-profile size respectively, and L_n and JRC_n are the length and *JRC* of predicted size respectively.

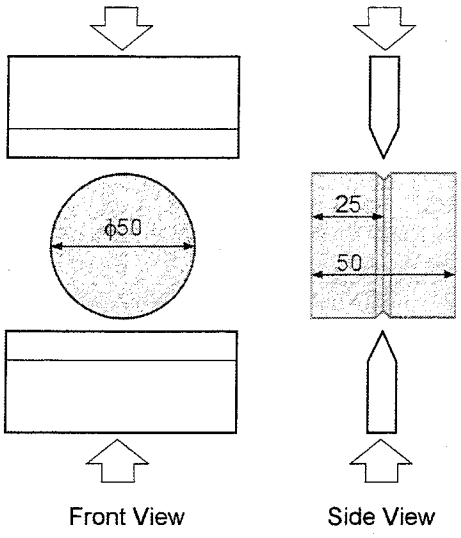

Figure 3.12: The artificial fracture surfaces by Brazilian test procedure.

Comparing Equation (3.10) with Equation (3.11), it can be said that the former is more reasonable than the latter from the next two points. The first point is that Equation (3.10) considers the interlocking of a fracture, and the second point is that the exponent representing the size effect in Equation (3.10) can be determined by the fractal dimension that is a scaling parameter.

3.5. *JRC* and shear strength of rock fractures

3.5.1. Profile measurement and shear test

In the previous sections, JRC-diagram was proposed to estimate *JRC* and its size effect. In this section, in order to check the validity of JRC-diagram, *JRC* was estimated by using JRC-diagram for several fracture surfaces produced in the laboratory, and the *JRC* values were compared with those by using JRC-profile. In addition, the peak shear strength for the fractured rock specimens was estimated by applying the *JRC* values to Equation (3.1), and it was compared with the result of the shear test.

The core-samples of Aji granite and Shirahama sandstone whose size is 5cm in length and 5cm in diameter were fractured perpendicularly to the core axis by Brazilian test procedure as shown in Figure 3.12. The Young's modulus, Poisson's ratio and uniaxial compressive strength of these samples are shown in Table 3.2.

Table 3.2: Young's modulus, Poisson's ratio and uniaxial compressive strength of the core samples.

Rock Type	Young's Modulous (GPa)	Poisson's Ratio	Uniaxial Compressive Strength (MPa)
Aji Granite	63	0.26	280
Shirahama Sandstone	12	0.38	70

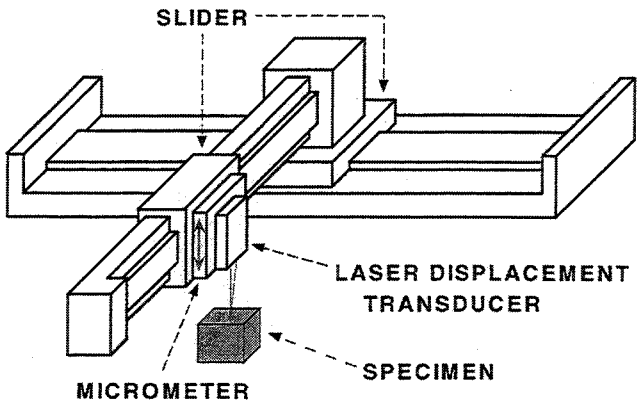

Figure 3.13: Surface profiler composed of two linear positioning systems and one laser displacement transducer.

Since the side surface of the core-samples was notched 2.5mm deep to be fractured easily, the produced fracture surfaces have 4.5cm in diameter. Thus, three fractured specimens for Aji granite and two fractured specimens for Shirahama sandstone were produced.

For the fracture surfaces of each specimen, surface profiles were measured by using a precise surface profiler shown in Figure 3.13. This surface profiler is composed of two linear positioning systems and one laser displacement transducer. They are NSK EML-Series whose positioning precision is 1μm and Keyence LC-2210 whose resolution is 0.2μm respectively. This laser displacement transducer yields a measurement error, because the colored minerals on a fracture surface cause the deflection of reflection factor. Therefore, plaster replicas were used for the granite specimens that are containing a lot of biotite. On the other hand, they were not used for the sandstone specimens. This is because, such the measurement error to the sandstone specimens was less than 5μm and it was ignored.

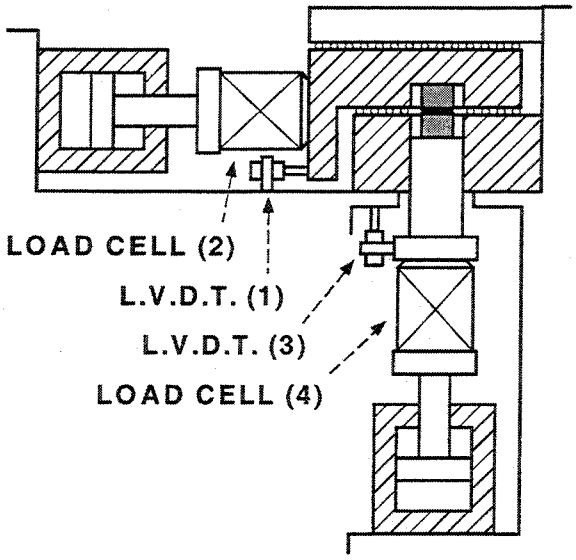

Figure 3.14: The schematic diagram of shear testing machine.

The 512 profiles were measured along the shear direction with the sampling interval of 0.05mm. The profiles had 512 data points and were separated 0.05mm each other. In addition, the center of the measured area was corresponded to the center of the fracture in order to measure the profiles in the same coordinate system. The profiles of facing two fracture surfaces were measured before and after the shear test, and the aperture profile was calculated. For the shared surfaces, the failed materials such as gouges were removed well before the profile measurement.

Share tests were carried out under the constant normal stress until the shear displacement reached to 2.5mm with the shear displacement rate of 0.05mm/minute. The schematic diagram of shear testing machine is shown in Figure 3.14. The normal stress was set to 7MPa, 14MPa and 21MPa for Aji granite. They correspond to 2.5%, 5% and 7.5% of the uniaxial compressive strength respectively. On the other hand, it was set to 3.5MPa and 7MPa for Shirahama sandstone. They correspond to 5% and 10% of the uniaxial compressive strength respectively. During the shear test, normal stress, normal displacement, shear stress and shear displacement were recorded every five seconds. The shear test was carried out two times for the specimens. Since the surface roughness and degree of interlocking will be changed by the shear test, the fracture surfaces having different *JRC* can be obtained by shear test.

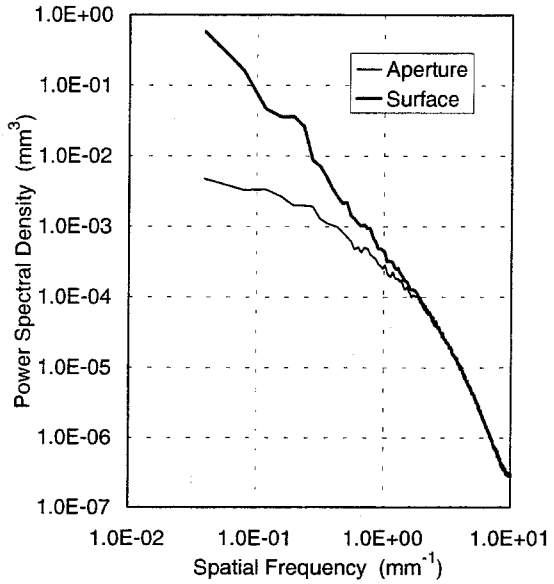

(a) Before the shear test

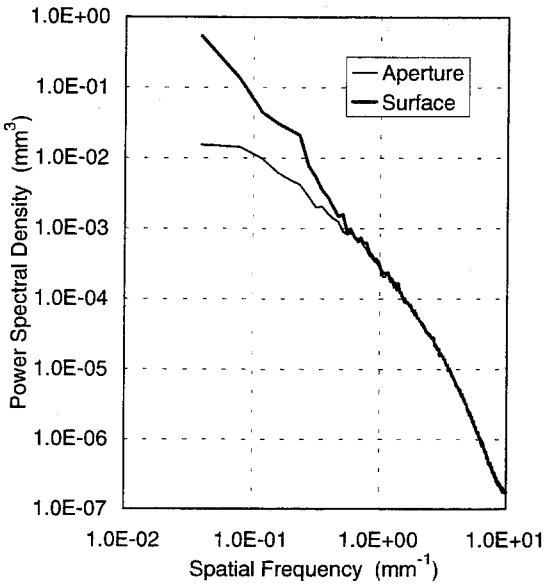

(b) After the first shear test

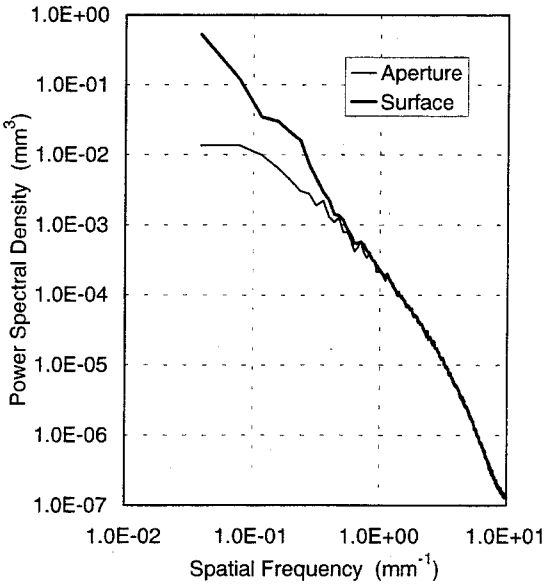

(c) After the second shear test

Figure 3.15: The log-log plots of the averaged PSD functions of the surface and aperture profiles for the granite specimen sheared under the normal stress of 14MPa. The interlocking wavelength increases with shearing.

3.5.2. Estimation of *JRC* and shear strength

Before the estimation of *JRC*, the interlocking wavelength, steepness and fractal dimension must be estimated. The interlocking wavelength was estimated from the log-log plot of averaged PSD functions of the 512 surface and aperture profiles. On the other hand, the steepness and fractal dimension were estimated from the variogram plot of averaged variogram function of the 512 surface profiles. Furthermore, these values of facing two surfaces were averaged for a fracture.

As an example, the log-log plots of the averaged PSD functions of the surface and aperture profiles are shown in Figure 3.15(a)~(c) for the granite specimen shared under the normal stress of 14MPa. Figure 3.15(a), Figure 3.15(b) and Figure 3.15(c) are for the specimen before shear test, after the first shear test and after the second shear test respectively. From these figures, it can be recognized that the interlocking frequency decreases with shearing, that is, the interlocking wavelength increases with shearing. On the other hand, the variogram plots for the same specimen are shown in Figure 3.16. From this figure, it can be seen that the steepness decreases with shearing.

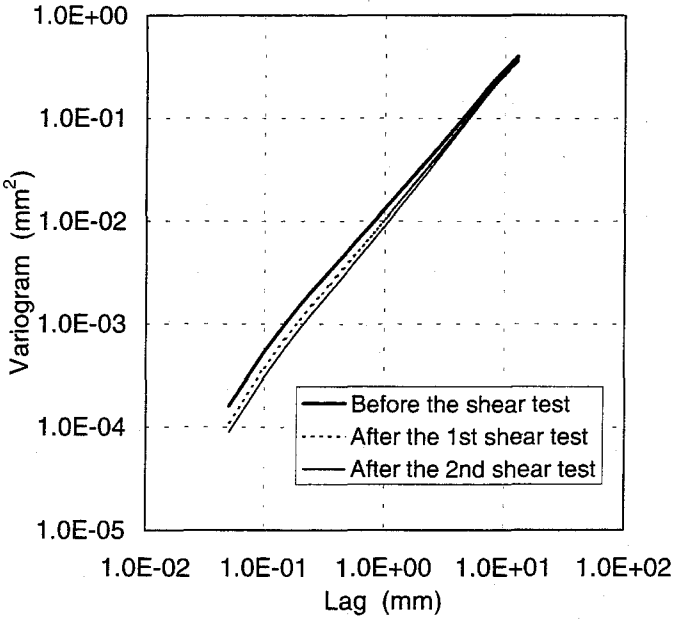

Figure 3.16: The variogram plots for the granite specimen sheared under the normal stress of 14MPa. The steepness decreases with shearing.

Table 3.3: The estimated interlocking wavelength, steepness, fractal dimension and *JRC*

Sample Name[1)]	Normal Stress (MPa)	Interlocking Frequency mm^{-1}	Interlocking Wavelength mm	Steepness mm^2	Fractal Dimension	JRC	
						JRC-diagram	JRC-Profile
K180	7.0	2.43593	0.411	0.012427	1.3245	10.74	12.33
K181	7.0	1.26257	0.792	0.010774	1.3285	7.25	12.17
K182	-	1.25826	0.795	0.010289	1.3045	6.95	10.00
K160	14.0	2.17652	0.459	0.013096	1.3085	10.40	11.33
K161	14.0	1.53184	0.653	0.010431	1.2806	7.52	9.17
K162	-	1.29783	0.771	0.008981	1.2634	6.32	8.50
K190	21.0	2.80780	0.356	0.015024	1.2663	12.01	11.83
K191	21.0	0.97774	1.023	0.014616	1.2581	7.99	10.50
K192	-	0.80475	1.243	0.013801	1.2524	7.17	10.00
S110	3.5	2.79616	0.358	0.005438	1.3722	6.90	8.33
S111	3.5	1.59608	0.627	0.003793	1.3079	3.86	8.00
S112	-	0.93277	1.072	0.003062	1.2832	2.65	7.00
S90	7.0	2.47704	0.404	0.006848	1.3393	7.29	7.17
S91	7.0	1.38054	0.724	0.004896	1.2736	4.26	5.50
S92	-	0.71476	1.399	0.003943	1.2491	2.89	4.83

1) KXXX indicates Aji granite, and SXXX indicates Shirahama sandstone.
XXX is decimal number, and the last number of each name indicates the number of shear test.

The estimated interlocking wavelength, steepness and fractal dimension are shown in Table 3.3. By using these values, *JRC* was estimated from JRC-diagram. In addition, *JRC* was estimated by using JRC-profile. For this method, six profiles separating 5mm each other were selected from the 512 profiles, and then these profiles were compared with JRC-profiles and determined their *JRC* values. Since the facing profiles seemed same, the six *JRC* values obtained from the lower fracture surface were averaged to be the *JRC* value of the fracture. An example of the selected profiles and determined *JRC* values are shown in Figure 3.17(a)~(c). This figure is for the same specimen used in Figure 3.15 and Figure 3.16. Moreover, Figure 3.17(a), Figure 3.17(b) and Figure 3.17(c) are for the profiles before shear test, after the first shear test and after the second share test respectively. From these figures, the profiles seem to be smooth with shearing.

The estimated *JRC* values by both methods are also shown in Table 3.3. Comparing these *JRC* values, *JRC* determined by JRC-diagram is a little smaller than that determined by JRC-profile. This tendency is much clear for the surfaces after the share test. Although the profiles became smoother by the shear test, the shape of the profiles was hardly changed as shown in Figure 3.17(a)~(c). Therefore, it seems difficult for JRC-profile to consider such the detail change of profile. On the other hand, JRC-diagram can consider the detail change of profile. This is

probably because the JRC-diagram is sensitive to the size of interlocking wavelength that is shorter than 1mm, but JRC-profile is not sensitive to such the small size.

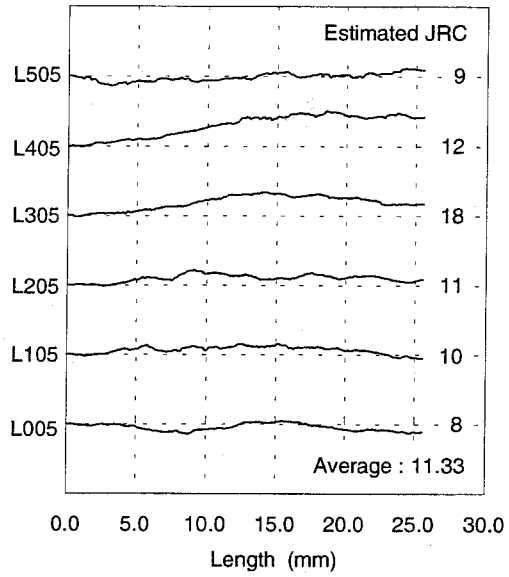

(a) Before the shear test

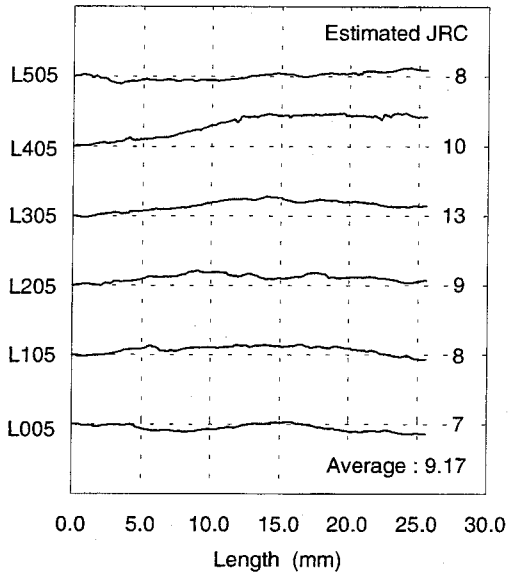

(b) After the first shear test

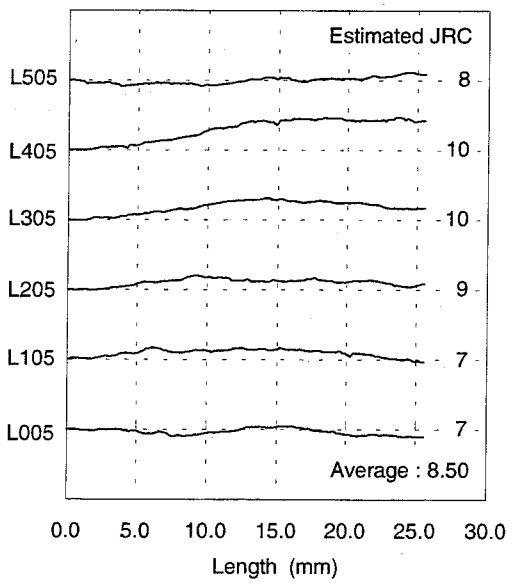

(c) After the second shear test

Figure 3.17: An example of the selected profiles and determined *JRC* values.

The peak shear strength of the fractures was estimated by applying the estimated *JRC* values to Equation (3.1). Adding to *JRC* and σ_n, *JCS* and ϕ_b are necessary for this equation. According to Barton and Choubey (1977), *JCS* can be supposed to be equal to the uniaxial compressive strength for a non-weathered fracture, and ϕ_b can be estimated from the values listed in Table 3.4. Therefore, the uniaxial compressive strength listed in Table 3.2 was used for *JCS*, and 33 degrees and 32 degrees were respectively used for ϕ_b of the granite and sandstone fractures. Thus, the peak shear strength is estimated as shown in Table 3.5. In this table, $\tau_{diagram}$ and $\tau_{profile}$ are the peak shear strength estimated by using JRC-diagram and JRC-profile respectively.

Table 3.4: Typical basic friction angle (after Barton and Choubey, 1977)

Rock Type	Moisture Condition	Basic Friction Angle ϕ_b	Reference
A. Sedimentary Rocks			
Sandstone	Dry	26-35	Patton, 1966
Sandstone	Wet	25-33	Patton, 1966
Sandstone	Wet	29	Ripley & Lee, 1962
Sandstone	Dry	31-33	Krsmanovic, 1967
Sandstone	Dry	32-34	Coulson, 1972
Sandstone	Wet	31-34	Coulson, 1972
Sandstone	Wet	33	Richards, 1975
Shale	Wet	27	Ripley & Lee, 1962
Siltstone	Wet	31	Ripley & Lee, 1962
Siltstone	Dry	31-33	Coulson, 1972
Siltstone	Wet	27-31	Coulson, 1972
Conglomerate	Dry	35	Krsmanovic, 1967
Chalk	Wet	30	Hutchinson, 1972
Limestone	Dry	31-37	Coulson, 1972
Limestone	Wet	27-35	Coulson, 1972
B. Igneous Rocks			
Basalt	Dry	35-38	Coulson, 1972
Basalt	Wet	31-36	Coulson, 1972
Fine-grained granite	Dry	31-35	Coulson, 1972
Fine-grained granite	Wet	29-31	Coulson, 1972
Coarse-grained granite	Dry	31-35	Coulson, 1972
Coarse-grained granite	Wet	31-33	Coulson, 1972
Porphyry	Dry	31	Barton, 1971b
Porphyry	Wet	31	Barton, 1971b
Dolerite	Dry	36	Richards, 1975
Dolerite	Wet	32	Richards, 1975
C. metamorphic Rocks			
Amphibolite	Dry	32	Wallace et al., 1970
Gneiss	Dry	26-29	Coulson, 1972
Gneiss	Wet	23-26	Coulson, 1972
Slate	Dry	25-30	Barton, 1971b
Slate	Dry	30	Richards, 1975
Slate	Wet	21	Richards, 1975

Table 3.5: The peak shear strength estimated by JRC-diagram and JRC-profile and the peak and residual shear strength obtained by the shear test.

Sample Name[1)]	Normal Stress (MPa)	τ_{peak} (MPa)	$\tau_{residual}$ (MPa)	$\tau_{diagram}$ (MPa)	$\tau_{profile}$ (MPa)
K180	7.0	17.84	6.88	8.40	9.21
K181	7.0	7.31	6.06	6.91	9.12
K182	-				
K160	14.0	35.57	15.87	14.77	15.41
K161	14.0	13.66	13.43	12.96	13.97
K162	-				
K190	21.0	40.37	22.74	22.14	21.98
K191	21.0	20.97	20.51	18.90	20.86
K192	-				
S110	3.5	11.15	2.85	3.04	3.25
S111	3.5	4.00	3.33	2.64	3.20
S112	-				
S90	7.0	17.08	6.54	5.73	5.70
S91	7.0	6.63	6.19	5.14	5.37
S92	-				

1) KXXX indicates Aji granite, and SXXX indicates Shirahama sandstone.
XXX is decimal number, and the last number of each name indicates the number of shear test.

3.5.3. Discussion

The shear displacement vs. shear stress curves and shear displacement vs. vertical displacement curves (*i.e.* dilatancy curves) for each fractured specimen are shown in Figure 3.18(a)~(e). In these figures, remarkable large peak shear strength can be seen in the first shear test, but it cannot be seen clearly in the second shear test. In addition, the residual shear strength of the first shear test is almost equal to that of the second shear test under the normal stress less than or equal to 7MPa. On the other hand, the residual shear strength of the first shear test is a little larger than that of the second shear test under the normal stress of 14MPa and 21MPa. The peak shear strength and the residual shear strength obtained from the shear test are also shown in Table 3.5. Here, the peak shear strength was given by the maximum shear strength. Therefore, it is not always the shear strength at the time when the fracture start sliding. On the other hand, the residual shear strength was given by the average of the shear strength mobilized after 2.4mm of shear displacement. In Table3.5, τ_{peak} and $\tau_{residual}$ are the peak shear strength and residual shear strength respectively.

In order to compare $\tau_{diagram}$ and $\tau_{profile}$ with τ_{peak} and $\tau_{residual}$, cross plots were made in Figure 3.19(a)~(d). First, from Figure 3.19(a)~(d), it can be recognized that $\tau_{diagram}$ is almost equal to $\tau_{profile}$. This is because the difference in shear strength become smaller than the difference in *JRC* from the property of Equation (3.1), though *JRC* estimated by JRC-diagram is a little smaller than that estimated by

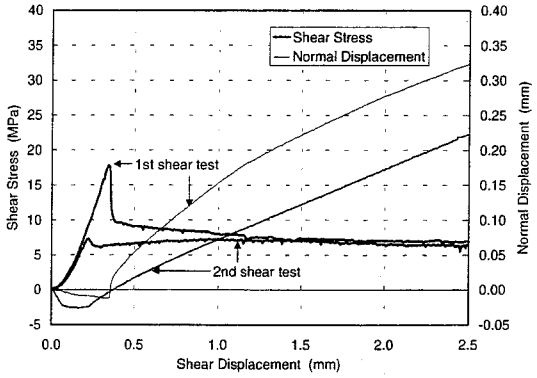

(a) Granite, normal stress = 7.0MPa

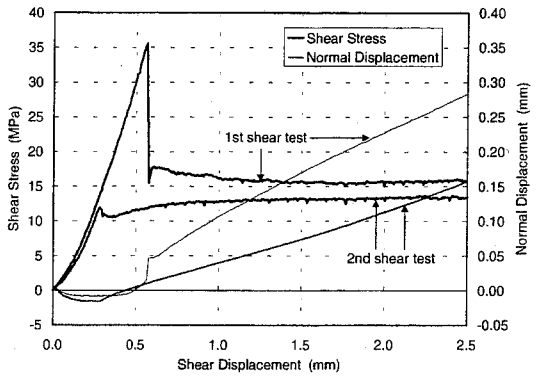

(b) Granite, normal stress = 14.0MPa

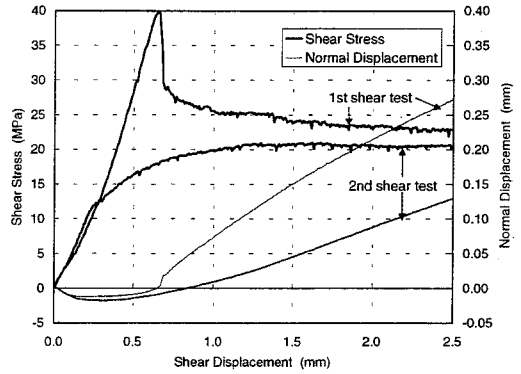

(c) Granite, normal stress = 14.0MPa

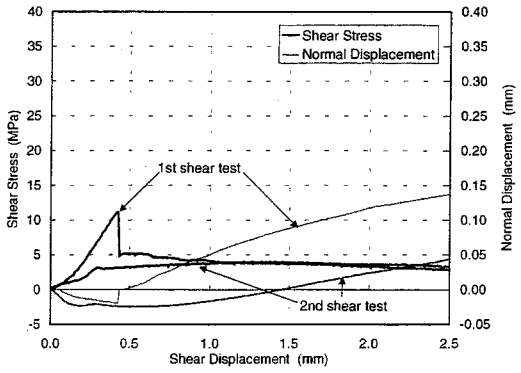

(d) Sandstone, normal stress = 3.5MPa

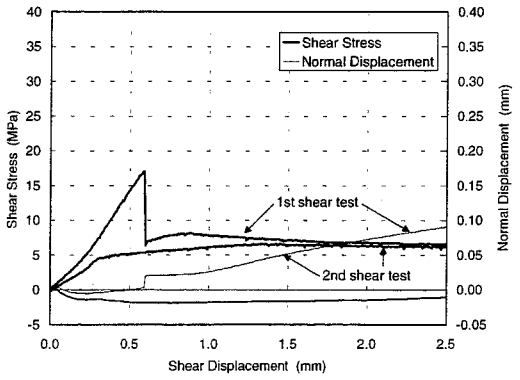

(e) Sandstone, normal stress = 7.0MPa

Figure 3.18: The shear displacement vs. shear stress curves and shear displacement vs. vertical displacement curves for each fractured specimen.

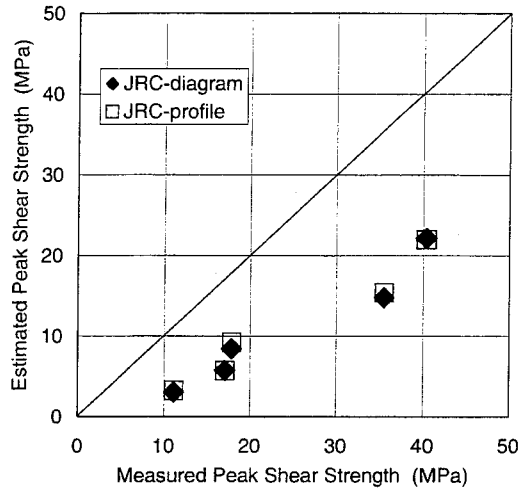

(a) Peak shear strength (1st shear test)

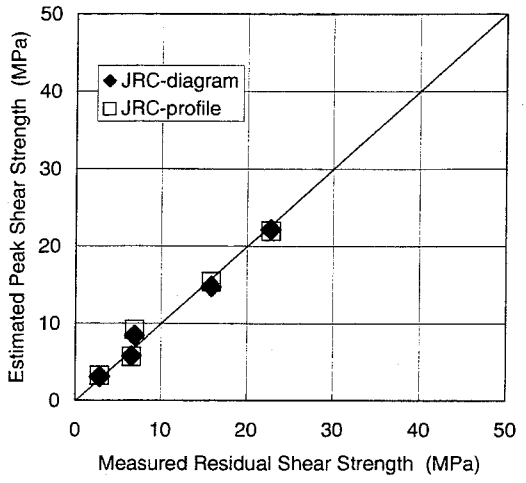

(b) Residual shear strength (1st shear test)

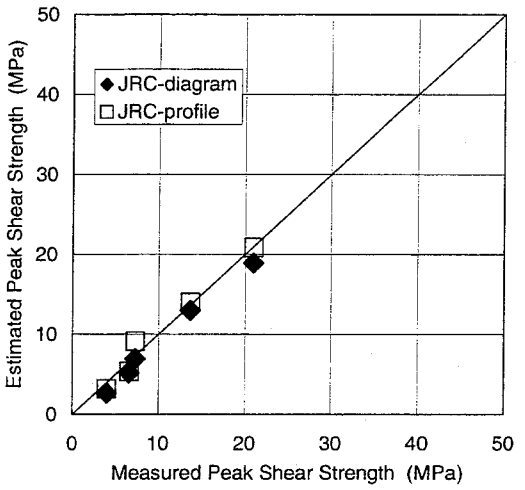

(c) Peak shear strength (2nd shear test)

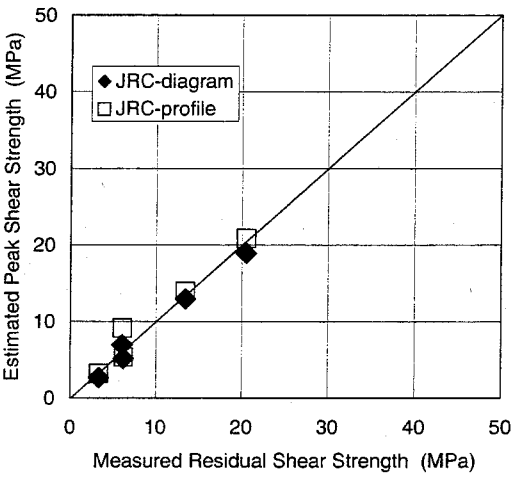

(d) Residual shear strength (2nd shear test)

Figure 3.19: Cross plot for the estimated shear strength and measured shear strength.

JRC-profile. Second, for the first shear test, it can be seen from Figure 3.19(a) that $\tau_{diagram}$ and $\tau_{profile}$ have positive correlation with τ_{peak}, but they are much smaller than τ_{peak}. In addition, it can be seen from Figure 3.19(b) that they are equal to $\tau_{residual}$ rather than τ_{peak}. On the other hand, for the second shear test, it can be seen from Figure 3.19(c) and Figure 3.19(d) that $\tau_{diagram}$ and $\tau_{profile}$ are almost equal to τ_{peak} and $\tau_{residual}$.

Table 3.6: Estimated actual interlocking wavelength for the fracture surface before shear test.

Sample Name	K180	K160	K190	S110	S90
Actual Interlocking Wavelength (mm)	0.082	0.048	0.043	0.019	0.014

From these results, it can be concluded that both the JRC-diagram and JRC-profile are not adequate to estimate *JRC* for the non-sheared and interlocking fracture, but they are adequate for the sheared or non-interlocking fracture. However, the actual interlocking wavelength can be assumed much smaller than that estimated by profile measurement, because the interlocking of a fracture is advanced by applying the normal and shear stresses.

Based on this assumption, the interlocking wavelength of each specimen to show τ_{peak} for the first shear test was estimated by backward calculation. Concretely, *JRC* was first estimated by Equation (3.1), and the interlocking wavelength was next estimated by JRC-diagram. Consequently, as shown in Table 3.6, the actual interlocking wavelength distributes from 0.043mm to 0.082mm for the granite specimen and from 0.014mm to 0.019mm for the sandstone specimen. Moreover, it seems to be small with the increase in normal stress. However, it is impossible to check whether such a small interlocking wavelength is actually valid or not. This is because the profile measurement can not be performed under a stressed condition and the spot diameter of the laser displacement-meter, which is about 0.09mm, is larger than the interlocking wavelength shown in Table 3.6. Furthermore, this discussion is based on the assumption that the Equation (3.1) is valid for estimating peak shear strength. However, if the actual interlocking wavelength becomes small with increase in normal stress as shown in Table 3.6, Equation (3.1) must be modified. This is because the term in Equation (3.1), $JRClog(JCS/\sigma_n)$, becomes small with the increase in normal stress and this is contrary to the results of the backward calculation. From these discussions, additional investigation on the contact problem of a fracture must be done in order to describe the peak shear strength for non-sheared and interlocking fracture.

On the other hand, the actual interlocking wavelength for the second shear test probably equals to that estimated by profile measurement even under the stressed condition, because the small interlocked asperities may be failed during the first

shear test. Therefore, $\tau_{diagram}$ and $\tau_{profile}$ were almost equal to τ_{peak} and $\tau_{residual}$. Furthermore, it can be said that Equation (3.1) is valid for the estimation of peak shear strength for the sheared or non-interlocking fracture and residual shear strength for every fracture.

3.6. Conclusions

The fractal model of a rock fracture is uniquely determined by the steepness and fractal dimension. First, the correlation between these parameters and *JRC* were investigated. Consequently, it was clarified that steepness and fractal dimension are closely related to the surface roughness and its size effect respectively. Second, a new original concept of JRC-diagram that is a self-similar fractal model determined by the variogram method was presented to evaluate the surface roughness and its size effect. In addition, the control size, which is the lag used for the roughness estimation by JRC-diagram, was suggested to be determined from the interlocking asperities size of the fracture surfaces. Third, by using JRC-diagram, the size effect of *JRC* was discussed and a theoretical equation that has the same style with the experimental equation presented by Barton *et al.* was derived. Finally, in order to check the validity of JRC-diagram, the *JRC* estimated by JRC-diagram was compared with the *JRC* determined from JRC-profile for several specimens. Moreover, the peak shear strength was estimated from these *JRC* values and compared with the results of shear test. Consequently, it was concluded that both the JRC-diagram and JRC-profile can not estimate *JRC* for non-sheared and interlocking fracture, but they can for sheared or non-interlocking fracture. However, JRC-diagram has a possibility to estimate the *JRC* of non-sheared and interlocking fracture, if the actual size of interlocking asperities that is under the stressed condition is much smaller than that estimated from profile measurement. In order to check the possibility and to describe the peak shear strength for such the fracture, additional investigations on the contact problem of a fracture must be done.

References

Bandis, S., A. C. Lumsden, and N. R. Barton, Experimental studies of scale effects on the shear behavior of rock joints, *Int. J. Rock. Mech. Min. Sci. & Geomech. Abstr.*, Vol. 18, 1-21, 1981.

Barton, N., Review of a new shear strength criterion for rock joints, *Engineering Geology*, Vol. 7, 287-332, 1973.

Barton, N. and V. Choubey, The shear strength of rock joints in theory and practice, *Rock Mechanics*, Vol. 10, 1-54, 1977.

Brown, S. R. and C. H. Scholz, Broad bandwidth study of the topography of natural rock surfaces, *J. Geophys. Res.*, Vol. 90, 12575-12582, 1985.

Brown, S. R., A note on the description of surface roughness using fractal dimension, *Geophys. Res. Lett.*, Vol. 14, 1095-1098, 1987.

Brown, S. R., Measuring the dimension of self-affine fractal: example of rough surfaces, In *Fractal in the Earth Sciences*, Barton, C. C. and La Point, P. R. (eds), Ch. 4. Plenum Press, New York, 77-87, 1995.

I. S. R. M. Commission on Standardization of Laboratory and Field Test, Suggested methods for the quantitative description of discontinuities in rock masses, *Int. J. Rock Mech. Min. Sci. & Geomech. Abstr.*, Vol. 15, 319-368, 1978.

Kulatilake, P. H. S. W., G. Shou, and T. H. Huang, A variogram/fractal based new peak shear strength criteria for rock joints, *Proc. 35th U. S. Symp. on Rock Mech.*, Balkema (Rotterdam), 673-697, 1995.

Ladanyi, B. and G. Archambault, Simulation of shear behavior of a jointed rock mass, *Proc. 11th Symp. on Rock Mech.*, Vol. 1, 105-125, 1970.

Lee, Y. H., J. R. Carr, D. J. Barr, and C. J. Haas, The fractal dimension as a measure of the roughness of rock discontinuity profiles, *Int. J. Rock Mech. Min. Sci. & Geomech. Abstr.*, Vol. 27, 453-464, 1990.

Mandelbrot, B. B., *The fractal geometry of nature,* W. H. Freeman and Company, New York, 1983.

Murata, S. and T. Saito, Evaluation of rock joint surface roughness by using fractal model (*in Japanese*), *Sigen-to-Sozai*, Vol. 113, 555-560, 1997.

Myers N. O., Characteristic of surface roughness, *Wear*, Vol. 5, 182-189, 1962.

Odling, N. E., Natural fracture profiles, fractal dimension and joint roughness coefficients, Rock Mech. Rock Eng., Vol. 27, 135-153, 1994.

Patton, F. D., Multiple modes of shear failure in rock, *Proc. 1st ISRM Congr.*, Lisbon, Vol. 1, 509-513, 1966.

Peitgen, H. -O. and D. Saupe, *The science of fractal images*, Ch. 1, Springer-Verlag, New York, 1988.

Power, W. L., T. E. Tullis, and J. D. Weeks, Roughness and wear during brittle faulting, *J. Geophys. Res.*, Vol. 93, 15,268-15,278, 1988.

Power, W. L. and T. E. Tullis, Euclidean and fractal models for the description of rock surface roughness, *J. Geophys. Res.*, Vol. 96, 415-424, 1991.

Sayles, R. S. and Thomas, T. R., The spatial representation of surface roughness by means of the structure function: a practical alternative to correlation, *Wear*, Vol. 42, 263-276, 1977.

Swan, G. and S. Zongqi, Prediction of shear behavior of joints using profiles, *Rock Mech. Rock Eng.*, Vol. 18, 183-212, 1985.

Tse, R. and Cruden, D. M., Estimating joint roughness coefficient, *Int. J. Rock Mech. Min. Sci. & Geomech. Abstr.*, Vol. 16, 303-307, 1979.

CHPTER4

CHANGE OF SURFACE PROPERTIES AND CONTACT CONDITION OF ROCK FRACTURE WITH THE PROGRESS OF SHEARING

4.1 Introduction

Contact condition is one of the most important factors affecting the mechanical properties of rock fractures. The contact condition is supposed to be a function of surface roughness, degree of interlocking, aperture and amount of gouge. Most of the fractures in a virgin rock mass probably interlock without any apertures and gouges. For this type of rock fracture, it has been thought that the shear strength can be evaluated by using the empirical equation presented by Barton and Choubey (1977), Equation (3.1). On the other hand, most of the fractures in the plastic region around a rock cavern and on the surface of natural or developed rock slope usually have aperture more or less. In addition, some of them may be sheared. For this type of rock fracture, it has been thought that the degree of contact condition such as interlocking, aperture and the amount of gouges besides surface roughness must be evaluated to give an exact estimation of shear strength.

However, as shown in Section 3.5, the Barton's equation could not estimate the peak shear strength for the non-sheared and interlocking fracture, but it could estimate the peak shear strength for the sheared and non-interlocking fracture. Furthermore, the equation could estimate the residual shear strength for both types of fracture. This result is different from the above general concept. Furthermore, reviewing the previous researches, only a few papers studying the effect of contact condition on the mechanical properties of rock fracture have been published. For example, Ladanyi and Archambault (1970) introduced a coefficient of interlocking to evaluate the shear strength of imperfectly interlocked fractures. In addition, Swan and Zongqi (1985), Yoshioka and Scholz (1989a, 1989b) discussed the closing and shearing properties of rock fracture by using a composite topography that is generated by the summation of upper and lower surface height. However, these pieces of research do not always consider the actual contact condition, because the actual contact condition usually changes with the progress of shearing and the change of it is difficult to forecast. Therefore, as concluded in Chapter 3, additional

investigations on the contact problem of a rock fracture must be done to evaluate the contact condition and describe the shear properties of a rock fracture correctly.

Here, for this purpose, fourteen rock fracture surfaces of Shirahama sandstone produced by Brazilian test procedure are sheared up to the different five stages of shearing as listed in Table 4.1. For these rock fractures, the change of surface properties is investigated by precise surface topography measurement, and the change of contact condition is directly observed by using a microscope. Furthermore, the relation between the fracture contact area and P-wave amplitude is investigated to know the change of contact condition under the stressed condition of shear test. Based on these investigations, shear process is discussed with the change of surface properties and contact condition.

Table 4.1: The list of the rock fracture specimens used for the topography measurement and microscope observation.

Shear Displacement	Topography Measurement	Microscope Observation
0 mm (Normal stress only)	No.30	F1
A little before the peak shear strength	No.31, No.32	F2
Just after the peak shear strength	No.33, No.34	F3
1 mm	No.36, No.37	F4
2 mm	No.39, No.40	F5

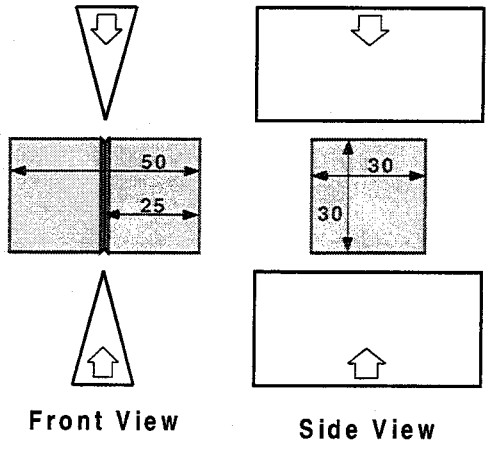

Figure 4.1: The shape of the rock specimen and the method to make a rock fracture surface.

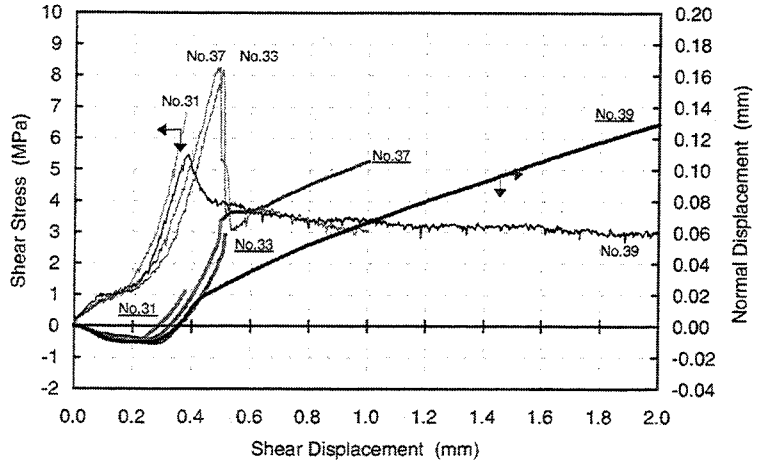

(a) The curves for the specimens used for the surface topography measurement.

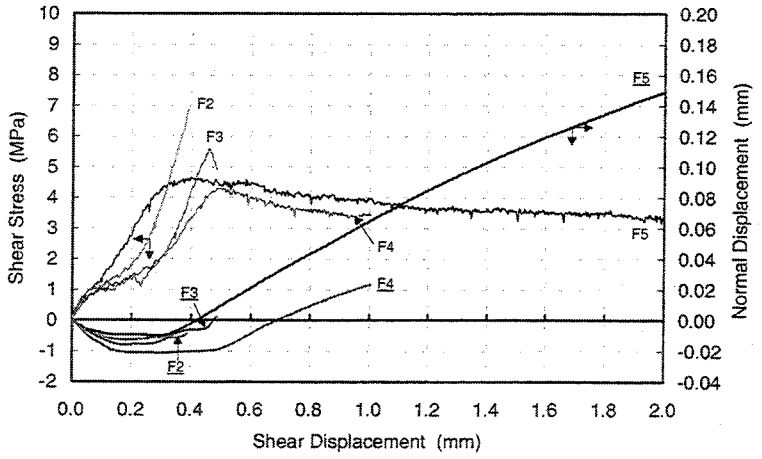

(b) The curves for the specimens used for the microscope observation

Figure 4.2: The shear displacement vs. shear stress and normal displacement vs. shear displacement curves obtained from the shearing. The thick curves indicated by the specimen's name with underline are the normal displacement-shear displacement curves.

4.2. Surface topography measurement and observation of contact condition

4.2.1. Fracture specimen of rock

The rock fracture surfaces of Shirahama sandstone whose uniaxial compressive strength is 59MPa, Young's modulus is 12GPa and Poisson's ratio is 0.24 were produced by Brazilian test procedure as shown in Figure 4.1. All of the

generated fractures were square shape whose side is 28mm long, because the notch prepared for making the fracture easily had a depth of 1mm. In addition, all fractures were perpendicular to the bedding plane. These fractures were sheared up to the different five stages of shearing as listed in Table 4.1 under the normal stress of 3MPa and the shear displacement rate of 0.05mm/min. The shear-testing machine is the same as shown in Figure 3.14. During the shearing, the shear stress, normal stress, shear displacement and normal displacement were measured every five seconds. The obtained shear stress vs. shear displacement curves and normal displacement vs. shear displacement curves are showed in Figure 4.2.

4.2.2. Measurement of fracture surface topography

The topography of the rock fracture surface was measured by using a precise surface profiler. As shown in Figure 3.13, this surface profiler is composed of two linear positioning systems and one laser displacement transducer. In order to detect the absolute change of surface topography, the origin of the measurement coordinate system was set to the center point of the specimen before fractured. As mentioned in Section 3.5.1, the laser displacement transducer yields a measurement error for a rock fracture surface because the colored minerals on the fracture surface have a different reflection factor each other. However, this kind of measurement error of this laser displacement transducer was less than 5μm to the fracture specimens of Shirahama sandstone. Therefore, the topography was measured on

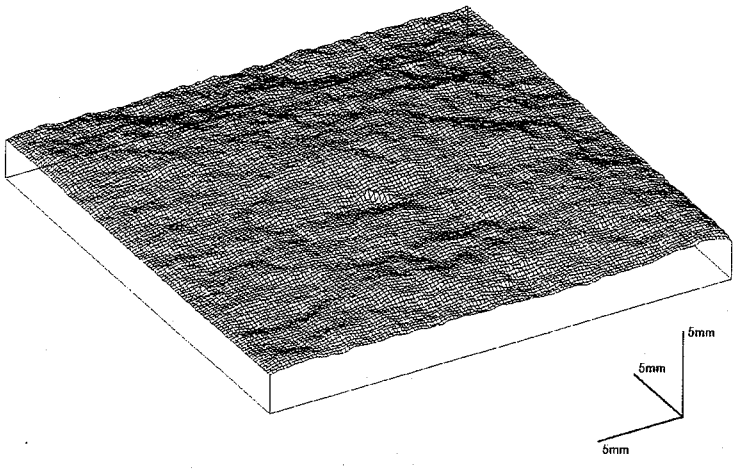

Figure 4.3: A result of the surface topography measurement.

the lattice of 256 by 256 points whose interval is 108μm without using plaster replicas. Consequently, the measured area was about 97% of the fracture surface area. An example of the obtained fracture surface is shown in Figure 4.3. This figure is shown by reducing the data points from 256 to 128 in x and y direction.

4.2.3. Microscope observation of contact condition of fractures

The observation of contact condition of rock fracture was carried out as follows. First, the sheared specimen was removed carefully from the shear box to keep the sheared condition. Second, the fracture was filled with red polyester resin, and sliced perpendicular to the fracture surface and parallel to the shear direction with every 4mm thick. Last, the sliced surface was observed under a stereomicroscope.

It is necessary to consider the recovery of normal and shear displacement in order to estimate the actual stressed contact condition, because this observation was performed under the unloaded condition. From the result of measurement, the recovery of normal displacement was from 0.02mm to 0.03mm and that of shear displacement was from 0.2mm to 0.3mm.

4.3. Results of surface topography measurement

4.3.1. The change of surface height

The change of surface height by the shearing can be known by subtracting the height after shearing from that before shearing. In this case, the region where the asperities were sheared and the height was decreased is described by positive value. On the other hand, the region where the removal of gouges was imperfect and the gouges remained on the fracture surface is described by negative value. An example of the result of subtraction is shown in Figure 4.4. The upper right of this figure showing large change of surface height is the region where the specimen was failed from the edge of the shear box. This failure was probably occurred by the stress concentration appeared at the edge of the shear box. Therefore, this large failure must be distinguished from the asperity failure, so that the center region of 128x256 points was used for the successive analysis.

For each stage of shearing, the mean and the standard deviation of the change of surface height are shown in Table 4.2. The ratio of the area where the change of surface height is more than 50μm and negative to the total area used for the analysis

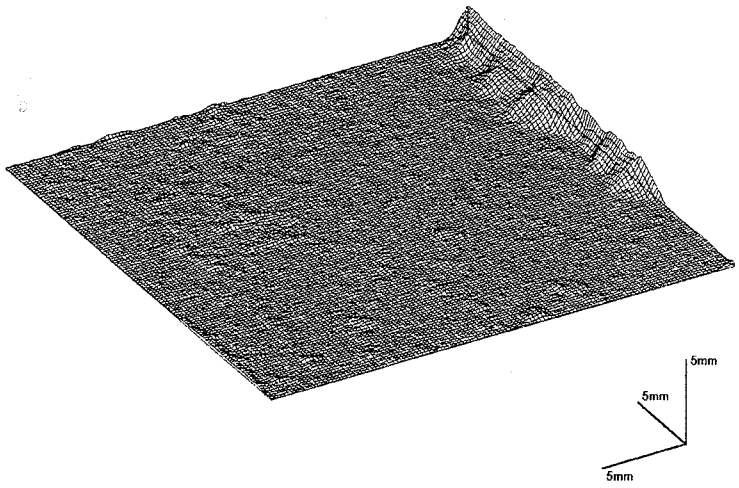

Figure 4.4: The distribution of surface height change.

Table 4.2: The mean and the standard deviation (S.D.) of the change of surface height caused by the shearing.

Shear Displacement	Specimen Name	Surface Side	Surface Height Change (μ m)		R(50) [1] (%)	R < 0 [2] (%)
			Mean	S.D.		
0 mm (Normal Stress Only)	No.30	Upper	21	15	2.39	5.22
		Lower	31	12	6.48	0.14
		Mean	26	14	4.44	2.68
A little before the peak shear strength	No.31	Upper	25	12	2.91	1.29
		Lower	25	17	7.15	5.22
		Mean	25	14	5.03	3.26
	No.32	Upper	22	13	1.83	2.71
		Lower	31	14	5.72	0.37
		Mean	27	13	3.78	1.54
Just after the peak shear strength	No.33	Upper	36	16	13.74	0.29
		Lower	37	19	14.49	0.30
		Mean	37	17	14.12	0.30
	No.34	Upper	9	16	1.88	26.50
		Lower	16	16	3.50	10.64
		Mean	12	16	2.69	18.57
1 mm	No.36	Upper	48	30	32.26	0.39
		Lower	22	24	10.87	10.47
		Mean	35	27	21.57	5.43
	No.37	Upper	27	30	16.75	9.98
		Lower	37	36	23.08	5.23
		Mean	32	33	19.92	7.61
2 mm	No.39	Upper	40	27	24.90	2.55
		Lower	42	30	26.90	2.30
		Mean	41	29	25.90	2.43
	No.40	Upper	27	29	16.21	12.78
		Lower	21	31	13.65	21.06
		Mean	24	30	14.93	16.92

1) R(50) is the ratio of the area where the change of surface height is more than 50 μm to the area of total joint surface.

2) R < 0 is the ratio of the area where the change of surface height is negative to the area of total joint surface.

are also shown in the column of R50 and R<0 respectively. From Table 4.2, we can know that the mean of the surface height change is from 25 to 27μm before the peak shear strength and it is from 32 to 41μm after the peak shear strength except for the specimen No.34 and No.40. From these results, it can be thought that the decrease of surface height increases by passing the peak shear strength, and the degradation of the fracture surface progresses with increasing the shear displacement after that. Furthermore, the reason why the change of surface height for the specimen No.34 and No.40 is small can be thought that the gouges were not removed enough. It can be supposed from the result that the R<0 value of these sample is larger than that of the other specimens.

On the other hand, we can know that the standard deviation of the surface height change is from 13 to 17μm until just after the peak shear strength and it is from 27 to 33μm after the shear displacement of 1mm. Considering that the standard deviation describes the magnitude of deviation from the mean value, the change of the surface topography until just after the peak shear strength is more uniform than that after the shear displacement of 1mm. In other word, there exist two regions after the shear displacement of 1mm. They are the region where the surface topography clearly changes and the region where the surface topography hardly changes.

4.3.2. The change of MEDF

On a fracture surface, the slopes that have positive angle to the shear direction resist the shear force. Among these slopes, the slope of maximum angle is most resistible. Considering this point, we modified EDF (Elevation Difference Function) proposed by Sun *et al.* (1995) and defined a new function called MEDF (Modified Elevation Difference Function). For a profile of rock fracture surface, MEDF is defined by Equation (4.1):

$$M(h) = \max\{z(x+h) - z(x)\} \tag{4.1}$$

where $z(x+h)$ and $z(x)$ are the surface height at $x+h$ and x, and h called lag distance or simply lag is the distance between these two points. In addition, max{ } is an operator to take the maximum value. For a rock fracture surface, MEDF is defined by the ensemble average of the MEDF for every profile parallel to the shear direction.

MEDF is supposed to be sensitive to the degradation of steep asperities, which

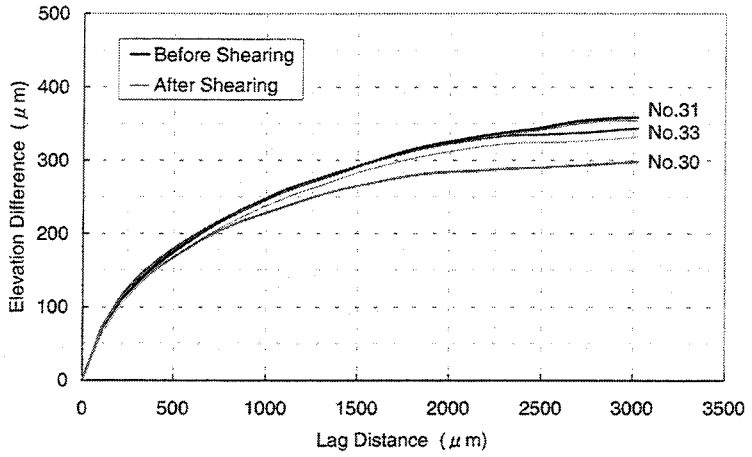

(a) MEDF for the specimen No.30, No.31 and No.33.

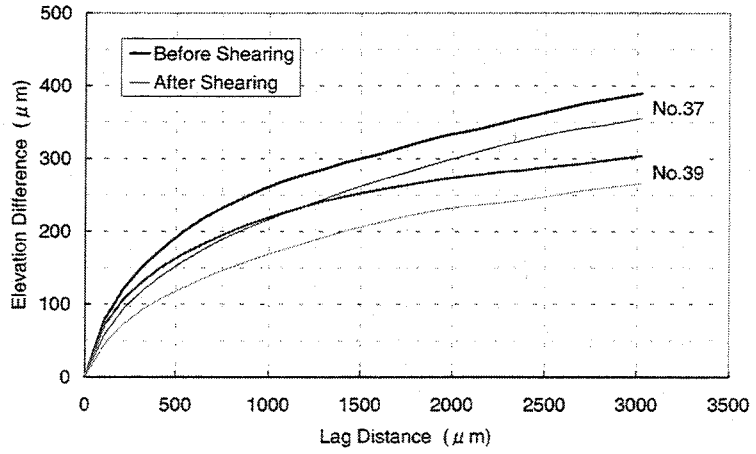

(b) MEDF for the specimen No.37 and No.39.

Figure 4.5: The change of MEDF for the specimen of different stage of shearing. The thick lines show the MEDF before shearing and the thin lines show the MEDF after shearing.

are the most influential to the shear property of the fracture, and to be able to detect the change of surface property that was missed by the analysis of surface height change. In order to investigate the change of this kind of surface property with the progress of shearing, MEDF curves of the specimens, No.30, 31, 33, 37, 39, were drawn in Figure 4.5(a) and Figure 4.5(b) for the fracture surface before shearing and after shearing. In these figures, the thick lines show before shearing and the thin

lines show after shearing. All curves are the average of MEDF of upper and lower surface. Generally, the MEDF after shearing decreases from that before shearing if the steep asperities are degraded by shearing. Therefore, we investigate the decrease of MEDF to know the amount of degradation of steep asperities.

From Figure 4.5(a), the decrease of MEDF can hardly be observed for the specimen No.30 that is applied normal stress only. On the other hand, the decrease of MEDF can be observed for the other specimens and it becomes large with the progress of shearing. The remarkable decrease of MEDF can be observed especially when the shear condition changes from a little before the peak shear strength to the shear displacement of 1mm. Furthermore, the decrease of MEDF is little after the shear displacement of 1mm. From these results, it can be said that the steep asperities are mainly failed when the shear condition passes the peak shear strength and reaches to the residual shear strength.

4.3.3. The change of power spectral density and fractal property

The power spectral density (PSD) function for a surface profile can be obtained by spectral analysis. Then, the range of spatial frequency or wave number of the PSD function is determined by the profile length, l, and the sampling interval, r, as $[1/l, 1/2r]$. Here, the PSD function of a fracture surface was defined by the ensemble average of the PSD function of the profiles that are parallel to the shear direction. The PSD function is proportional to the square of the amplitude of asperities. Therefor, if the PSD function after shearing become lower than that before shearing in a certain frequency range, we can suppose that the asperities whose size corresponds to the frequency range were failed.

Figure 4.6 shows the log-log plot of the PSD function for the specimens No.30, 31, 33, 37 and 39 according to the progress of shearing. Each graph is the average of PSD function of upper and lower surface. The thick lines show the PSD function before shearing and thin lines show that after shearing. In addition, the PSD functions of each sample are drawn with one log-cycle offset of spatial frequency to show them separately. From Figure 4.6, it is hardly recognized that the PSD functions after shearing become lower than that before shearing for the specimens No.30 and No.31 that have not reached the peak shear strength. On the other hand, it is recognized clearly that the PSD functions after shearing become lower than that before shearing for the specimens No.33, No.37 and No.39 that have passed the peak shear strength. Furthermore, the spatial frequency where the PSD

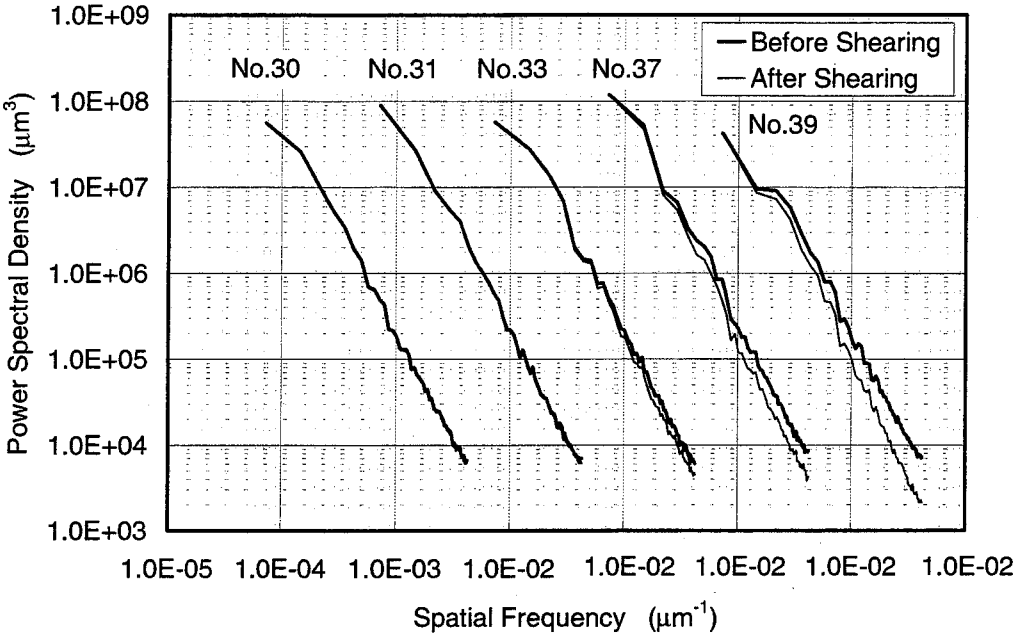

Figure 4.6: The change of PSD for the specimen of each stage of shearing. The thick lines show the PSD function before shearing and thin lines show the PSD function after shearing.

Table 4.3: The change of the fractal dimension and failure-limited frequency.

Specimen Name	Shear Displacement	Fractal dimension		Reduction ratio (%)	Failure-limited Frequency
		Before shearing (a)	After shearing (b)	((a)-(b))/(a) × 100	(μm^{-1})
No.30	0 mm (Normal stress only)	1.27	1.25	1.6	-
N0.31	A little before the peak shear strength	1.20	1.20	0.0	-
N0.32		1.25	1.24	0.8	(1.23E-3)
N0.33	Just after the peak shear strength	1.22	1.17	4.1	3.62E-03
N0.34		1.22	1.16	4.9	3.62E-03
N0.36	1 mm	1.23	1.14	7.3	1.45E-04
N0.37		1.23	1.16	5.7	7.23E-05
N0.39	2mm	1.25	1.09	12.8	7.23E-05
N0.40		1.27	1.08	15.0	7.23E-05

function start decreasing gradually moves to the lower frequency with the progress of shearing. We call this spatial frequency failure-limited frequency. From these results, it can be supposed that the small asperities having high spatial frequency are failed especially on the process of passing the peak shear strength, and then the fracture surface is degraded with the progress of shearing. Consequently, the failure-limited frequency is supposed to be lower.

Each PSD function under the failure-limited frequency can be approximated by a straight line. Therefore, it can be assumed that the fracture surface is fractal in this range of spatial frequency even after shearing. Based on this assumption, the fractal dimension before and after shearing was calculated. The calculated fractal dimension is shown in Table 4.3. From this table, it can be recognized that the decrease of fractal dimension is remarkable from just after the peak shear strength, and then it increases with the increase in shear displacement. Generally, the fracture surface becomes smooth with the decrease in fractal dimension. Therefore, it can be thought that the fracture surface becomes smooth with the progress of shearing especially after the peak shear strength.

4.3.4. The change of interlocking

The interlocking of a fracture surface is an important factor indicating a contact condition of the fracture surface. The degree of interlocking will become gradually worse if the asperities are failed with the progress of shearing. Here, the difference of interlocking between before and after shearing was investigated for all the specimens whose surface profiles were measured.

The interlocking can be evaluated by the interlocking frequency. It was defined by Murata and Saito (1997) as the spatial frequency where the discrepancy of PSD function between the surface profile and the aperture profile begins to be observed as shown in Figure3.8. The detail of the interlocking frequency has been explained in Section 3.4.2.

Table4.4: The change of interlocking frequency with the progress of shearing.

Specimen Name	Shear Displacement	Interlocking Frequency		Reduction ratio
		(a) Before shearing (μm^{-1})	(b) After shearing (μm^{-1})	((a)-(b))/(a)×100 (%)
No.30	0 mm (Normal stress only)	2.68E-03	2.68E-03	0.0
N0.31	A little before the peak shear strength	2.60E-03	2.97E-03	-14.2
N0.32		2.68E-03	2.75E-03	-2.6
N0.33	Just after the peak shear strength	2.68E-03	2.39E-03	10.8
N0.34		2.82E-03	2.68E-03	5.0
N0.36	1 mm	2.31E-03	1.52E-03	34.2
N0.37		2.39E-03	1.95E-03	18.4
N0.39	2mm	3.04E-03	2.24E-03	26.3
N0.40		2.68E-03	2.03E-03	24.3

The interlocking frequency for the surface before shearing and after shearing is shown in Table 4.4. In this table, the interlocking frequency after shearing is evaluated under the zero shear displacement condition. Therefore, the change of interlocking frequency indicated in this table is caused by the change of surface topography induced by the shearing. From this table, it can be known that the interlocking frequency of a little before the peak shear strength, specimens No.31 and 32, is higher than that of normal stress only, specimen No.30. This shows that the interlocking of a little before the peak shear strength is better than that of normal stress only. On the other hand, after the peak shear strength, the interlocking is gradually worse with the progress of shearing except for the specimen No.36. This is probably because the interlocked asperities were sheared off with the progress of shearing.

4.4. Results of microscope observation

The pictures of rock fracture for each stage of shearing described in Table 4.1 are shown in Figure 4.7(a)-(e). In Figure 4.7(b)-(e), the arrows indicate the shear direction.

First, from Figure 4.7(a), it can be seen that the rock fracture applied normal stress only contacts at a very few points and has an aperture about 100μm. Moreover, the wavelength of interlocked asperities is longer than 0.5mm. This smallest interlocked asperity size almost corresponds to the interlocking frequency shown in Table 4.4 that is from 2.31E-3 to 3.04E-3 μm^{-1}.

Second, from Figure 4.7(b), it can be recognized that the rock fracture a little before the peak shear strength interlocks very well. The shortest wavelength of the interlocked asperity is less than 0.1mm. In addition, the fracture aperture is less than about 15μm, which is much smaller than that of the fracture applied normal stress only. This picture may be an evidence of the contraction shown in Figure 4.2 and the advance of interlocking shown in Table 4.4. Moreover, this result supports the possibility of such the small interlocking wavelength as shown in Table 3.6. Therefore, if such the small interlocking wavelength can be estimated, the correct peak shear strength can be estimated by using JRC-diagram. Furthermore, since the obvious slide of fracture can not be recognized on this stage of shearing, the shear displacement measured on this stage is probably caused by the deformation of the interlocked asperities.

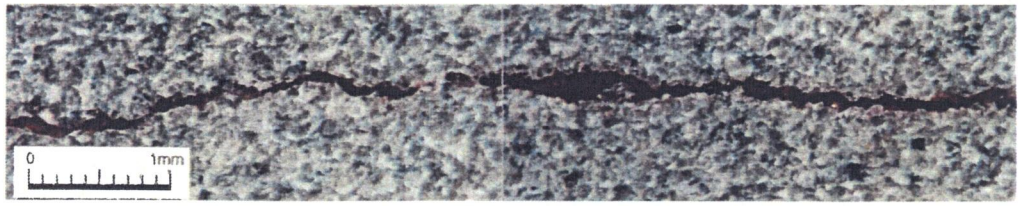

(a) Shear displacement of 0mm (Normal stress only)

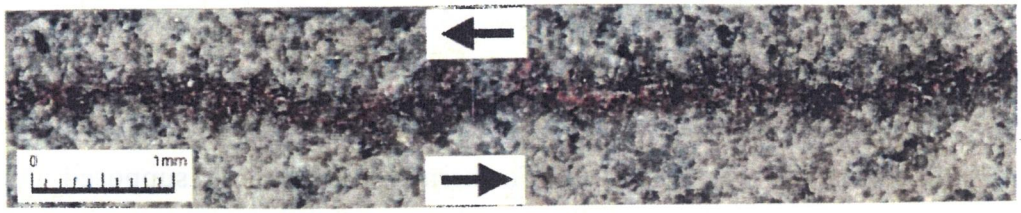

(b) A little before the peak shear strength

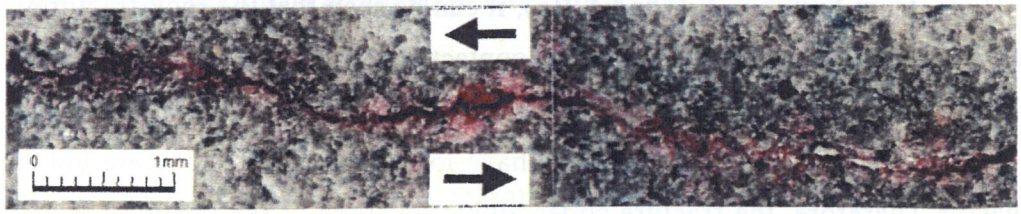

(c) Just after the peak shear strength

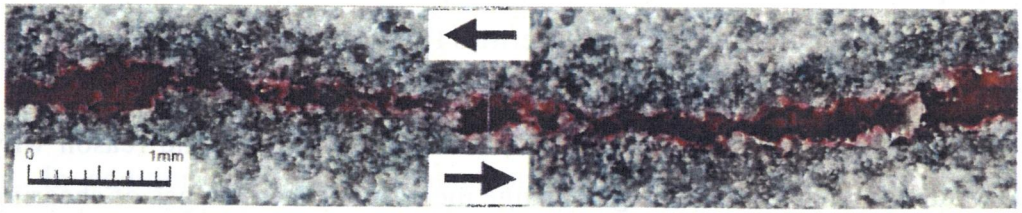

(d) Shear displacement of 1mm

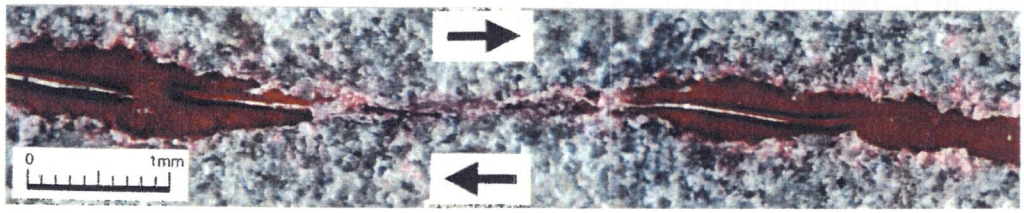

(e) Shear displacement of 2mm

Figure 4.7: The contact condition of the rock fractures observed by a microscope.

Third, from Figure 4.7(c), it can be seen that the rock fracture just after the peak shear strength slides and has about 50μm of aperture excepting at some contact points. In addition, a very little amount of gouge can be recognized in the aperture. On the other hand, the normal displacement increases rapidly from just before the peak shear strength to just after the peak shear strength as shown in Figure 4.2. This rapid increase in normal displacement is remarkable especially for the case that the clear peak shear strength was observed. Generally, the asperity of short wavelength has steeper slope than that of long wavelength. Therefore, we can suppose that the rock fracture interlocked at the asperities of short wavelength start sliding along the steep slope with the some distortion of the asperities, so that the rapid increase of normal displacement was observed. Furthermore, it can be supposed that the interlocking was suddenly released with a little failure of asperities when the resistance to the shear force reached the limit.

Last, from Figure 4.7(d) and 4.7(e), it can be seen that the rock fractures of the shear displacement of 1mm and 2mm contact on the slope of asperities that has positive gradient to the shear direction. In addition, at the contact points, gouges can be observed. Since these asperities have long wavelength, they are not sheared off easily. Therefore, the fracture slides along the slope of the contact asperity with shearing the small asperities, so that the dilation increases with the increase in the shear displacement. On the other hand, the aperture increases with the increase in shear displacement at the surface of asperities that has negative gradient to the shear direction. Consequently, the contacting surfaces are smoothed and the non-contacting surface maintained its roughness. This is probably the reason why the standard deviation of surface height change increases at these stages of shearing.

4.5. The relation between the fracture contact area and P-wave amplitude

4.5.1. The specimens for P-wave measurement

P-wave propagates in a fractured rock by passing through the contact areas of a fracture. Therefore, it can be thought that the P-wave propagating in a fractured rock has several pieces of information about the contact condition of a fracture.

In this section, first, six specimens of Shirahama sandstone that is arranged to have different contact area are prepared as shown in Figure 4.8. For these specimens, the P-wave measurement is carried out by mating them with a specimen of flat surface to investigate the relation between the contact area and P-wave amplitude.

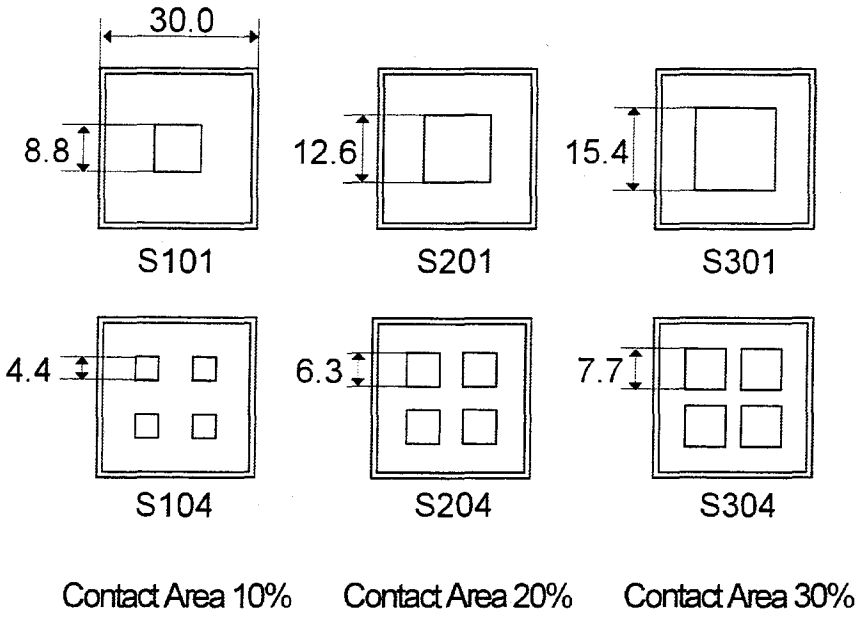

Figure 4.8: The specimens arranged to have different contact area.

Second, two fractured specimens of Shirahama sandstone are prepared by the same way shown in Figure 4.1. For these specimens, the P-wave measurement is carried out during the shear test to investigate the change of contact area with the progress of shearing.

The size of the specimens arranged to have different contact area is 30mm wide, 30mm long and 25mm high, and the edges of upper surface are planed off 1mm. In addition, the square shape contact areas are 0.5mm higher than the surrounding surface to keep the arranged contact area constant. As shown in Figure 4.8, the contact area of the specimens is 10%, 20% and 30% of the apparent fracture area, that is, the square area whose side is 28mm long. The number of the contact area is one and four. Among the specimens having the same number of contact area, the center points of the contact areas are located at the same points on the fracture surface. The P-wave velocity of these specimens is about 3300m/s in the measuring direction.

On the other hand, the fractured specimen, S55 and S56, was prepared by the same way as described in Section 4.2.1. The P-wave velocity of these specimens is about 2800m/s in the measuring direction.

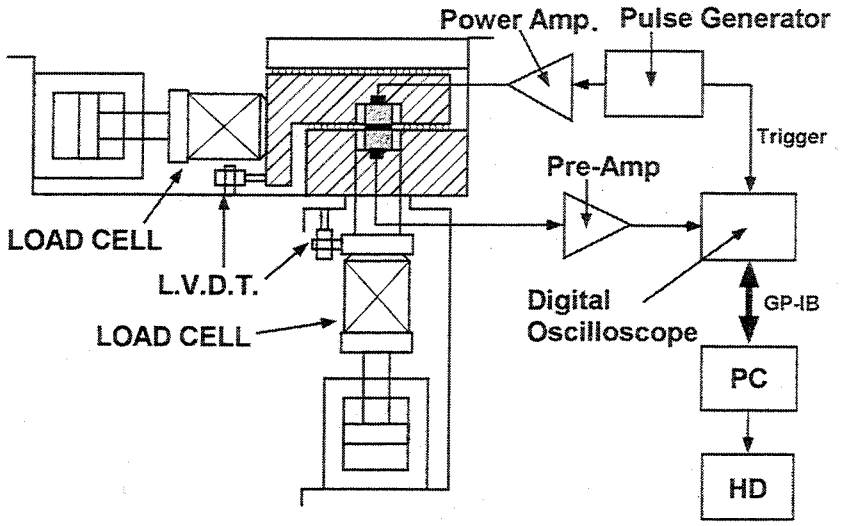

Figure 4.9: The shear testing machine and P-wave measurement system.

4.5.2. P-wave measurement and shear test

The specimens were set in the shear testing machine shown in Figure 4.9 and P-wave measurement was carried out under the normal stress of 3MPa. Two wide range AE sensors (NF Electronic Instruments, AE-900M) were used for the P-wave transmitter and receiver. These sensors were attached to the specimen directly at the center of the bottom surface. The P-wave measurement system is also shown in Figure 4.9. The pulse signal from the pulse generator was amplified 50 times by the power amplifier, and then applied to the transmitter. On the other hand, the received P-wave signal by the receiver was amplified 60dB by the pre-amplifier, and then it observed by the digital storage oscilloscope. In order to remove noise, the received signal was averaged 256 times by the oscilloscope. The oscilloscope was controlled by the personal computer (PC) and the averaged signal was transferred to the PC and stored in a hard disk drive.

The shear test was carried out under the normal stress of 3MPa and the shear displacement rate of 0.02mm/min. During the shear test, the P-wave measurement was carried out every 0.2mm of shear displacement and additional measurements were conducted just before and after the peak shear strength. Since it takes about one minute for averaging, the advance of shear displacement was stopped during the P-wave measurement. In addition, the shear stress, normal stress, shear displacement and normal displacement were measured every five seconds.

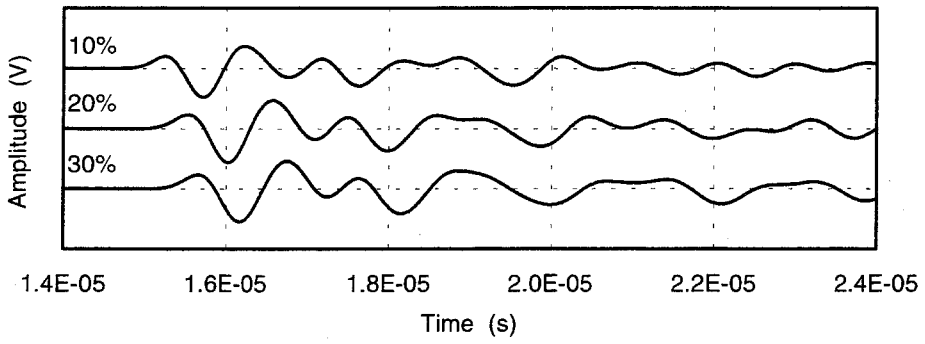

(a) One contact area

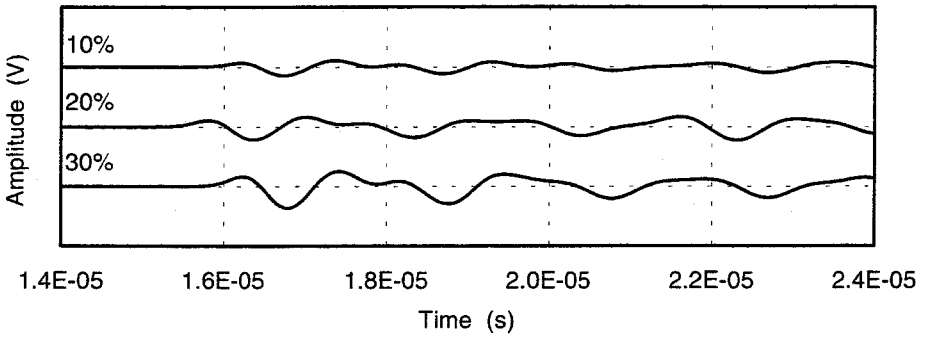

(b) Four contact area

Figure 4.10: The observed waveforms for the specimens of different contact area.

Table 4.5: Summary of the P-wave travel-time, velocity and amplitude.

Specimen	Travel Time (s)	Last Time (s)	Velocity (m/s)	V-1st (V)	V-rms (V)
s101	1.4765E-05	1.5215E-05	3386.4	0.012	0.057
s104	1.5665E-05	1.6779E-05	3243.7	0.041	0.041
s201	1.5005E-05	1.5929E-05	3332.2	0.141	0.111
s204	1.5170E-05	1.6704E-05	3321.4	0.063	0.066
s301	1.5130E-05	1.6503E-05	3304.7	0.141	0.165
s304	1.5600E-05	1.7523E-05	3216.6	0.101	0.111

4.5.3. The relation between the contact area and P-wave amplitude

For the specimens arranged to have different contact area, the observed waveforms are shown in Figure 4.10, and the travel-time, velocity and amplitude are summarized in Table 4.5. In this table, the specimen name corresponds to that shown in Figure 4.8. In addition, Travel Time is the travel-time of the first wave, and Last Time is the travel-time of the direct wave passing through the longest path

without multiple reflection. Furthermore, V-1st is the first-wave amplitude and V-rms is the rms-amplitude calculated from the P-wave observed between Travel Time and Last Time. The reason why the P-wave in this time range was used for the rms-amplitude is that the P-wave in this time range is not disturbed by the multiple reflection. Moreover, it can be thought to contain the most pieces of information about the contact condition of the surface.

Based on Table 4.5, the relation between the contact area and both V-1st and V-rms are plotted in Figure 4.11(a)-(b). Figure 4.11(a) is for the case of one contact area, and Figure 4.11(b) is for the case of four contact areas. From these figures, the followings can be recognized. The rms-amplitude is directly proportional to the contact area for both cases. On the other hand, the first-wave amplitude shows a direct proportion for the case of four contact areas, but it does not show a clear direct proportion for the case of one contact area. Therefore, it can be concluded that the rms-amplitude is more adequate for investigating the contact area than the first-wave amplitude.

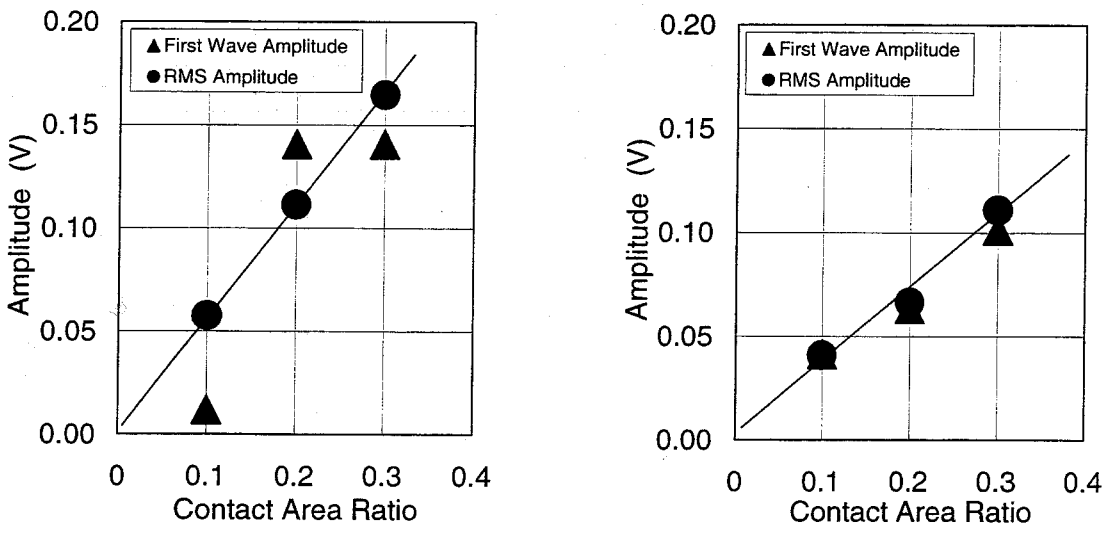

(a) One contact area

(b) Four contact areas

Figure 4.11: The relation between the contact area and P-wave amplitude.

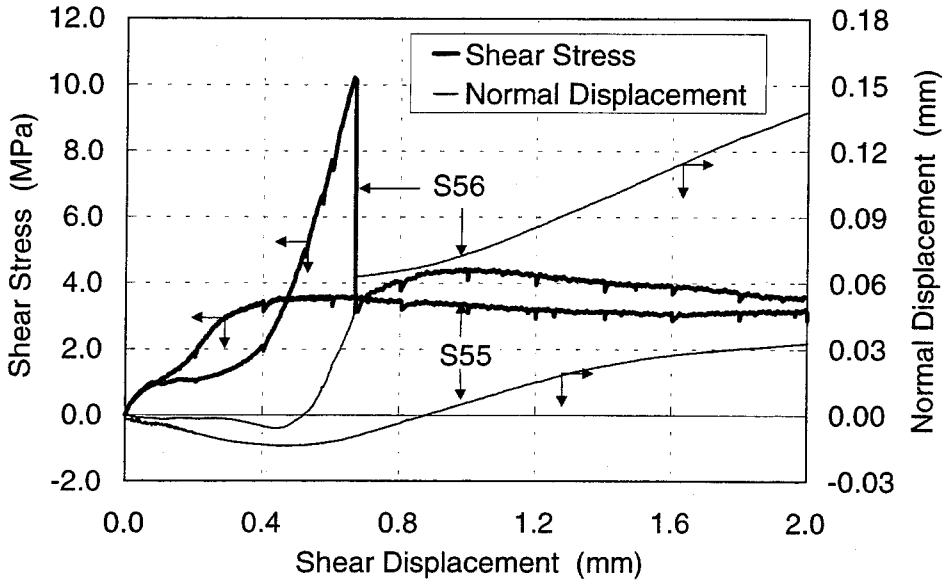

Figure 4.12: Shear displacement vs. shear stress curves and shear displacement vs. normal displacement curves for the fractured specimens.

4.5.4. The change of P-wave amplitude during the shear test

The shear displacement vs. shear stress curve and shear displacement vs. normal displacement curve obtained from the shear tests for the fractured specimens are drawn in Figure 4.12. As shown in this figure, one specimen, S56, has a clearly large peak shear strength, but another specimen, S55, has no peak shear strength.

On the other hand, the observed waveforms are shown in Figure 4.13(a)-(b) according to the progress of shearing. In these figures, the shear displacement for the P-wave measurement is indicated at the head of each waveform. In addition, it must be noted that the scale of vertical axis, which shows the amplitude of P-wave, is different each other; one division of the vertical axis of Figure 4.13(a) is 3.0V, and that of Figure 4.13(b) is 0.2V. From these waveforms, the rms-amplitude was calculated. In this case, the time range to calculate the rms-amplitude was determined so as no to include the reflected waves from side surfaces of the specimen. The change of the rms-amplitude with the progress of shearing is shown in Figure 4.14.

For the specimen showing peak shear strength, it can be recognized that the initial rms-amplitude is more than ten times larger than that of another specimen showing no peak shear strength. In addition, the rms-amplitude increases first when

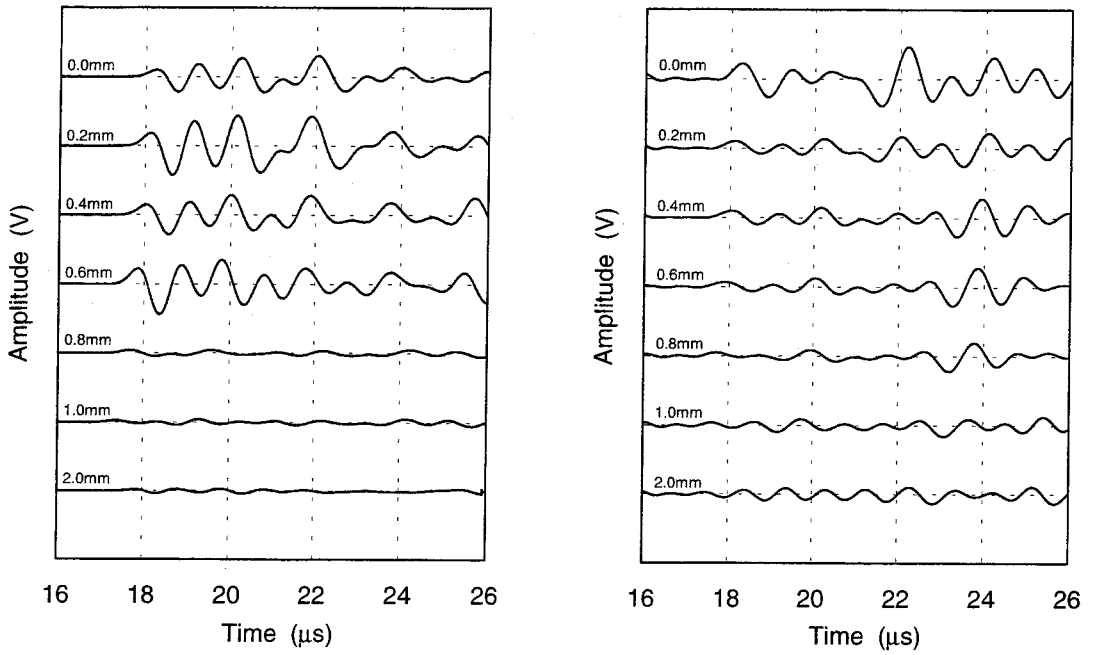

(a) Specimen showing peak shear strength (b) Specimen showing no peak shear strength

Figure 4.13: Observed waveforms according to the progress of shearing. The values of length in each figure indicate shear displacement.

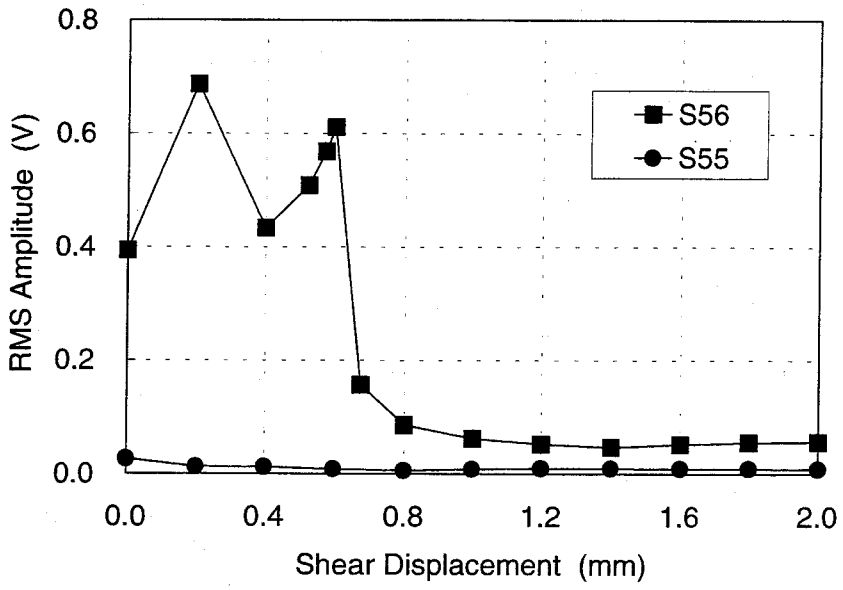

Figure 4.14: The change of the rms-amplitude with the progress of shearing. S56 shows peak shear strength, and S55 shows no peak shear strength.

the normal displacement is constant, but it decreases when the normal displacement decreases. After that, the rms-amplitude increases again with the rapid increase in normal displacement until the shear stress reaches the peak shear strength. Furthermore, it rapidly and largely decreases after the peak shear strength, and then it becomes constant under the residual shear strength. The final rms-amplitude is about five times larger than that of another specimen. On the other hand, the rms-amplitude of the specimen showing no peak shear strength decreases gradually, and then it becomes constant under the residual shear strength.

As shown in Section 4.5.3, the rms-amplitude is proportional to the fracture contact area. Therefore, it can be thought that the specimen showing peak shear strength initially has more than ten times larger contact area than the specimen showing no peak shear strength. However, the change of the rms-amplitude with the change of the normal displacement as mentioned above is difficult to explain only by the change of contact area.

According to the theory for seismic wave propagation across a displacement discontinuity such as a rock fracture, the coefficient of transmission of P-wave, T_p, can be described as a function of frequency, ω, (Nolte *et al.*, 1990).

$$T_p(\omega) = \frac{2(K_n/Z_p)}{-i\omega + 2(K_n/Z_p)} \tag{4.2}$$

where K_n is the specific stiffness in normal direction that is defined as the ratio of the applied stress to the average displacement and Z_p is the seismic impedance of P-wave. It is implicit from the Equation (4.2) that T_p increases with the increase in K_n. Since K_n generally increases with the increase in the applied stress, T_p probably increases with the increase in the applied stress. Therefore, the reason why the rms-amplitude increased just before the peak shear strength can be thought that the effect of increase in K_n may be larger than the effect of decrease in contact area. Thus, the effect of change in K_n must be considered when the contact area is estimated by using P-wave.

4.6. Discussion on the shear process

In this section, based on the results of above investigations, the shear process of an interlocking rock fracture is discussed by dividing it into five phases according to Archambault *et al.* (1996). The five phases are shown in Figure 4.15.

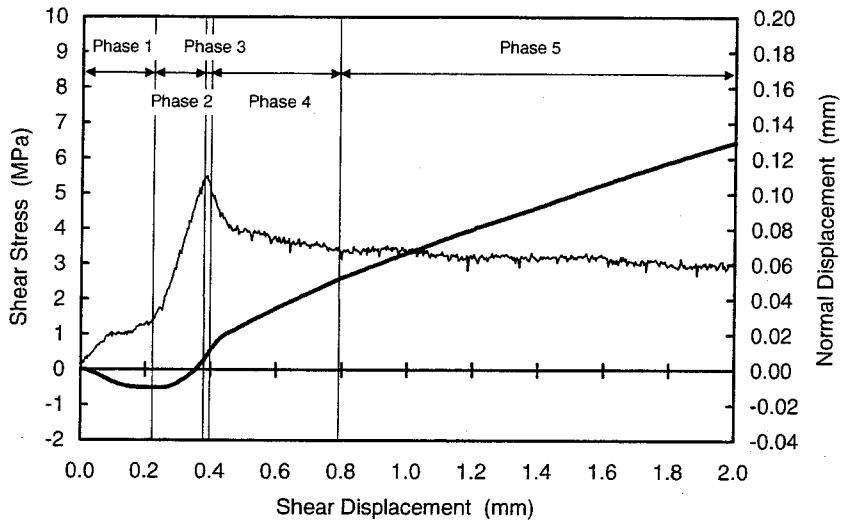

Figure 4.15: Five phases of shear process.

The first phase is initial shear stress mobilizing phase where the shear stress increases gradually and the normal displacement decreases more or less. In this phase, the following two points can be thought to be a reason for the decrease of normal displacement. The first point is that the insufficiently interlocking asperities are interlocked well by applying the shear force. The second point is that sufficiently interlocking asperities are bent by the applied shear force. Consequently, the actual interlocking wavelength is shortened to less than 0.1mm and the fracture aperture is reduced to less than 15μm as shown in Figure 4.7(b). In addition, it can be supposed that the contact area is initially increased by the advance of interlocking, but, after that, it is decreased to the one side of the interlocking asperities by bending of the interlocking asperities. Thus, the change of rms-amplitude as shown in Figure 4.14 can be observed. In this phase, furthermore, the macroscopic slide of the fracture has not taken place yet.

The second phase is dilatancy-hardening phase where the normal displacement increases non-linearly and shear stress increases linearly up to the peak shear strength with the large shear stiffness. In this phase, it can be thought that the fracture starts sliding along the surface of interlocking asperities. Since the interlocking asperities have a steep surface as observed by a microscope, the normal displacement increases rapidly.

The third phase is peak shear strength phase. In this phase, it can be thought that the shear resistance of interlocking asperities has reached the limit and the interlocking is just releasing. By passing this phase, the interlocking asperities are damaged to some extent, and therefore, the changes in surface height, MEDF, fractal dimension and interlocking frequency can be observed.

The forth phase is progressive softening phase where the shear stress decreases to the residual shear strength. In this phase, the contact condition changes from interlocking to non-interlocking. Therefore, the shear stress decreases and the increasing rate of normal displacement decreases. Moreover, under the non-interlocking condition, the damaged asperities on the contacting surface can be easily sheared off with the progress of shearing, but the asperities on the non-contacting surface can not be sheared. Consequently, the standard deviation of surface height change becomes large as shown in Table 4.2. In addition, the remarkable changes in surface height, MEDF, fractal dimension and interlocking frequency can be observed.

The fifth phase is residual shear strength phase. In this phase, the shear behavior is similar to that of fourth phase under the non-interlocking condition. The damaged small asperities on the contacting surfaces are sheared off with the progress of shearing. Therefore, as shown in Figure 4.7(e), fracture surfaces contact each other with some gouge. On the other hand, the asperities on the non-contacting surface can not be sheared. Consequently, the standard deviation of surface height change becomes large, and the remarkable changes in surface height, MEDF, fractal dimension and interlocking frequency can be observed.

Here, there is an interesting relation between the normal displacement vs. shear displacement curve (dilatancy curve) and the MEDF curve. The relation is that the dilatancy curve is nearly parallel to the lower MEDF curve for the surfaces after shearing as shown in Figure 4.16(a)-(b). In Figure 4.16(a), the drops of MEDF curve for both the upper and lower surfaces caused by the shearing are almost the same. This means that the degradation of facing two surfaces is almost the same for this specimen. On the other hand, in Figure 4.16(b), the drop of MEDF curve for the upper surface is much larger than that for the lower surface. This means that the degradation of upper surface is much larger than that of lower surface and the most of the degradation of fracture surface takes place on the upper surface for this specimen. However, it can be observed that for both specimens after shearing the MEDF curves of more degraded surface are almost parallel to the dilatancy curves.

This relation means that the fracture surfaces contact each other on such the steepest asperities that the MEDF considers according to the lag distance equivalent to the shear displacement. Therefore, if the MEDF curve for the sheared surface can be expected, the dilatancy behavior can be estimated without shear test.

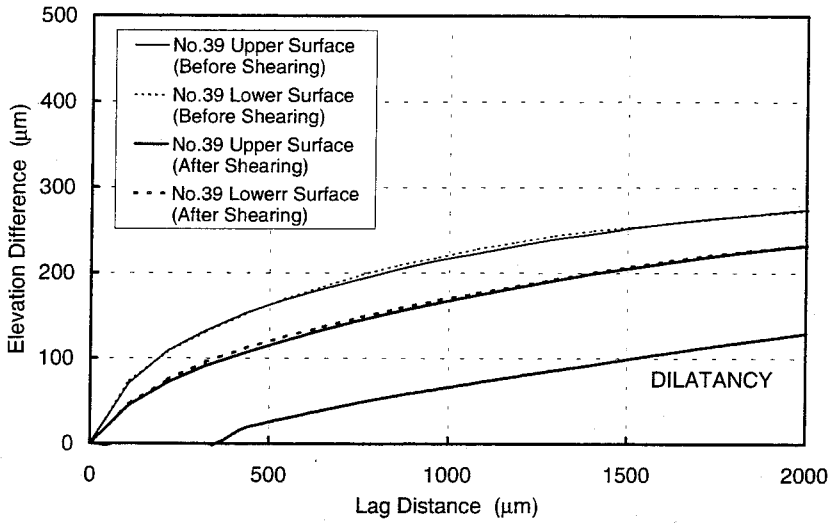

(a) MEDF curves for sheared surfaces are almost same

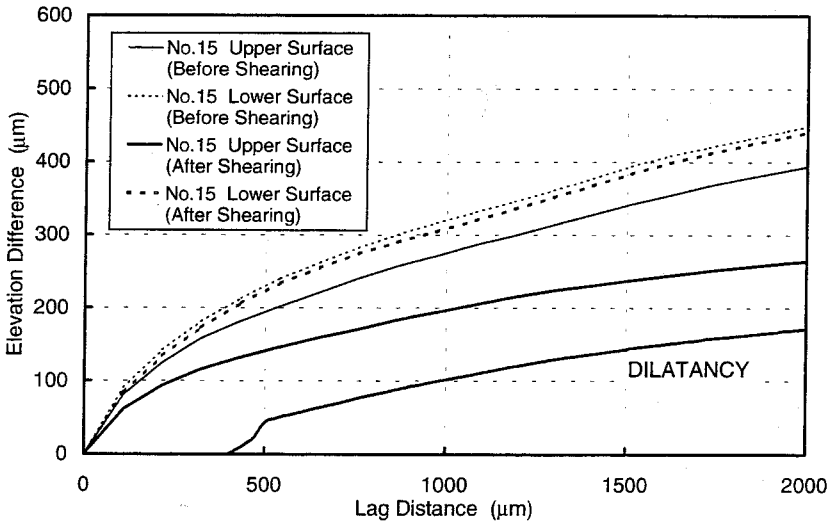

(b) MEDF curves for sheared surfaces are different

Figure 4.16: The dilatancy curve and the MEDF curve.

4.7. Conclusions

In this chapter, the changes of surface properties and contact condition with the progress of shearing were investigated. It was performed by the precise surface topography measurement and the direct observation using a microscope for the fourteen rock fracture surfaces of Shirahama sandstone produced by Brazilian test procedure and sheared up to the different five stages of shearing. Furthermore, the relation between the fracture contact area and P-wave amplitude is investigated to know the change of contact condition under the stressed condition of shear test.

Consequently, the followings were clarified. First, fracture surfaces degrade clearly after the peak shear strength and they become smooth with the progress of shearing. This is caused by the failure of small and steep asperities, and the failure mainly occurs at the peak shear strength and the successive residual shear strength. Second, the rock fracture interlocks closely by the application of shear stress at the beginning of the shearing, and the contraction of the fracture is induced. This result supports the possibility that the actual interlocking wavelength is much smaller than that determined from profile measurement. Therefore, the correct *JRC* is probably estimated by using JRC-diagram. Third, after the peak shear strength, the contact points of the fracture are limited to the slope of asperities that has positive gradient to the shear direction, so that the dilation of the fracture increases with increasing the shear displacement. It was observed that the dilatancy curve is nearly parallel to the lower MEDF curve for the fracture surfaces after shearing. On the other hand, the aperture increases with increasing the shear displacement at the other slope of the contact asperities. Therefore, there exist smoothed areas and rough areas on the fracture surface, and consequently the standard deviation of the surface height change becomes large. Last, it was observed that the rms-amplitude of direct wave is directly proportional to the contact area of a fracture. However, since the rms-amplitude can be affected by the specific stiffness, it was suggested that the change of the specific stiffness must be taken into consideration to estimate the contact area during the shear test.

Thus, these results help us to understand the shear process of a rock fracture qualitatively. Therefore, as discussed in section 3.5.3, it is necessary to develop a new method exchangeable for the Barton's empirical equation to estimate the shear properties considering the change of contact conditions.

References

Archambault, G., R. Flamand, S. Gentier, J. Riss and C. Sirieix, Joint shear behavior revised on the basis of morphology 3D modeling and shear displacement, *Proc. 2nd North American Rock Mech. Symp.*, 1223-1230, 1996.

Barton, N. and V. Choubey, The shear strength of rock fractures in theory and practice, *Rock Mechanics*, Vol.10, 1-54, 1977.

Ladanyi, B. and G. Archambault, Simulation of shear behavior of a fractured rock mass, *Proc. 11th U.S. Symp. on Rock Mech. AIME (New York)*, 105-125, 1970.

Muratra, S. and T. Saito, Evaluation of rock fracture surface roughness by using fractal model, *Shigen-to-Sozai*, Vol.133, 555-560, 1997 (in Japanese).

Pyrak-Nolte, L. J., L. R. Myer, and N. G. Cook, Transmission of seismic waves across single natural fractures, *J. Geophys. Res.*, Vol. 95, 8617-8638, 1990.

Sun, X., D. E. Chitty and S. E. Blouin, A comparative study on fracture roughness description by fractal, scaling and statistical methods, *Proc. 35th U.S. Symp. on Rock Mech.*, 711-716, 1995.

Swan, G. and S. Zongqi, Prediction of shear behavior of fractures using profiles, *Rock Mech. and Rock Eng.*, Vol.18, 183-212, 1985.

Yoshioka, N. and C. H. Scholz, Elastic properties of contacting surfaces under normal and shear load 1. Theory, *J. Geophys. Res.*, Vol. 94, 17681-17690, 1989a.

Yoshioka, N. and C. H. Scholz, Elastic properties of contacting surfaces under normal and shear load 2. Comparison of theory with experiment, *J. Geophys. Res.*, Vol. 94, 17691-17700, 1989b.

CHPTER5

CHARACTERIZATION OF FRACTURE PERMEABILITY BY USING A FRACTAL MODEL

5.1 Introduction

The formation fluid, such as water, oil and gases, mainly flow through fractures in a fractured rock mass, because fracture permeability is much larger than matrix permeability. Therefore, it is necessary to understand the behavior of the fluid flow in a single fracture as well as the heterogeneous distribution of the fractures in a rock mass.

Generally, the fracture permeability has been estimated by the cubic law described as follows.

$$q = -L_y \frac{d^3}{12\mu} \frac{dp}{dx} \tag{5.1}$$

where q is volumetric flow rate, L_y is fracture width, d is fracture aperture, μ is fluid viscosity and dp/dx is gradient of hydraulic pressure. The cubic law is valid for the laminar flow between two perfectly smooth parallel plates. However, the actual fracture surfaces have very complex geometry and some parts of them contact each other. Consequently, the behavior of fluid flow through the fractures is much more complex than that between the parallel plates. Therefore, it is difficult to represent such a complex fracture by a simple parallel plates model.

To overcome this difficulty, many pieces of research have been carried out as mentioned in Chapter 1. For example, a kind of correction factor for the surface roughness of a fracture, f, was introduced by Lomize (1951) and Louis (1969), and the empirical equation, Equation (1.5), was developed. By the correction factor f, Equation (5.1) can be written as follows.

$$q = -L_y \frac{d^3}{12\mu} \frac{1}{f} \frac{dp}{dx} \tag{5.2}$$

However, since this correction factor was derived from the experiment to the sand coated parallel glass plates and the rough concrete plates, it is difficult to say that the correction factor sufficiently represents the effect of the complex fracture

surface. On the other hand, a fractal model can represent the complex geometry of a fracture surface realistically. Therefore, the fracture permeability can be estimated more correctly if the correction factor is described by the fractal parameters, such as fractal dimension and steepness.

For this purpose, in this chapter, first, the core specimens of epoxy resin for the ten natural and artificial rock fractures that have different fractal parameters are prepared to remove the effect of the matrix permeability and porosity. Second, the fracture permeability and porosity are measured for the specimens under the several kinds of hydrostatic pressure, and investigated the deviation from the cubic law of fracture permeability. Last, the deviation from the cubic law of fracture permeability is theoretically represented by using the fractal parameters, and the effect of the parameters on the deviation is discussed.

5.2 Permeability measurement of single fracture

5.2.1 Specimens of the single fracture

The formation fluids flow in the rock matrix as well as the rock fracture. Therefore, it is necessary to remove the effect of the rock matrix in order to measure the fracture permeability and porosity correctly. For this purpose, the core specimens of epoxy resin that have a single fracture were made.

First, the natural and artificial rock fractures listed in Table 5.1 were shaped 3.8cm wide and 7cm long. Second, the fracture surfaces were copied by using a white silicon gum, KE-12 Shin-Etsu Chemical Co., Ltd. Last, the silicon gum blocks having the same surface properties with the rock fracture was used for

Table 5.1: The specimens of natural and artificial rock fracture

Specimen Name	Rock Type	Comment
M1	Marble	Artificial tensile fracture
M2	Marble	Artificial tensile fracture with shearing
S1	Sandstone	Artificial tensile fracture
S2	Sandstone	Artificial tensile fracture with shearing
T3	Tuff	Artificial tensile fracture
T4	Tuff	Artificial tensile fracture with shearing
HB	Pyrophyllite	Natural fracture sampled in Hiraki mine
I2	Limestone	Natural fracture sampled in Ibuki mine
GPV	Granite	Natural fracture (quarried in Portugal)
GSH	Granite	Natural fracture (quarried in Sweden)

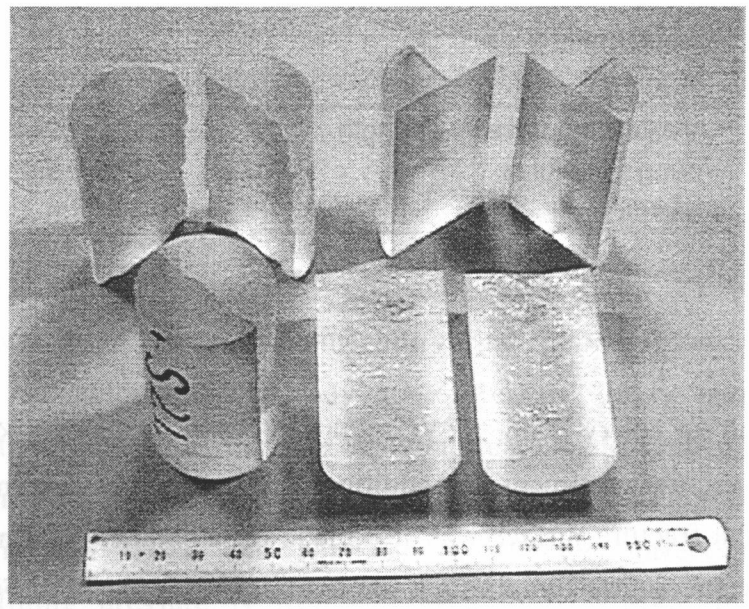

Figure 5.1: The epoxy core specimens containing a single fracture

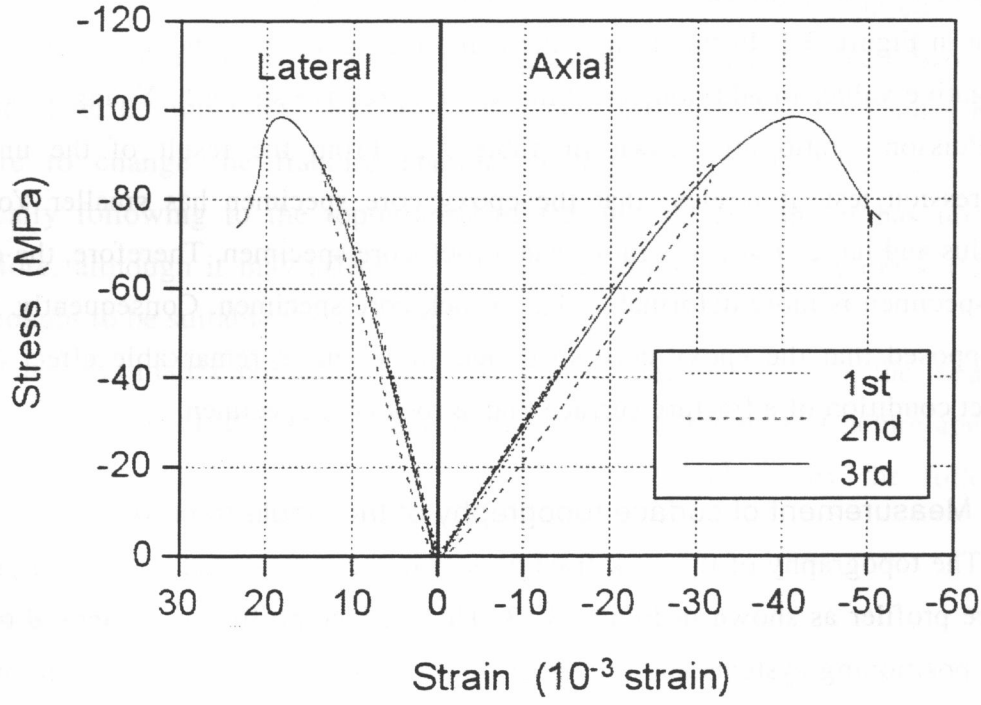

Figure 5.2: The stress-strain curve of the epoxy core specimen.

Table 5.2: The uniaxial compressive strength, Young's modulus and Poisson's ratio of the epoxy core specimen.

Uniaxial compressive strength	(MPa)	98.4
Young's modulus	(GPa)	3.03
Poisson's ratio		0.43

the matrix, and an epoxy resin, STYCAST 1263 Grace Japan K. K., was molded into the epoxy core specimens. In addition, an epoxy core specimen named FS containing a flat fracture surface was also made for a parallel plate model. Some of the epoxy core specimens containing a single fracture are shown in Figure 5.1.

Furthermore, in order to check the material properties of the epoxy core specimens, an epoxy core specimen whose size is 3.7cm in diameter and 7.5cm in length was made, and the uniaxial compression test was carried out. In order to check the recovery of deformation, in the uniaxial compression test, the axial load was unloaded at the axial stress about 40% and 80% of the uniaxial compressive strength, 106MPa, indicated on the catalog. The obtained stress-strain curves are shown in Figure 5.2. In this figure, the compressive stresses and strains are shown in negative value. In addition, the uniaxial compressive strength, Young's modulus and Poisson's ratio are shown in Table 5.2. From the result of the uniaxial compression test, it is clear that the epoxy core specimen has smaller Young's modulus and larger Poisson's ratio than a rock core specimen. Therefore, the epoxy core specimen is more deformable than a rock core specimen. Consequently, it can be supposed that the epoxy core specimen shows more remarkable effect of the contact condition of a fracture surface than a rock core specimen.

5.2.2 Measurement of surface topography of the single fracture

The topography of the rock fracture surface was measured by using a precise surface profiler as shown in Figure 3.13. This surface profiler is composed of two linear positioning systems and one laser displacement transducer. As mentioned in Section 3.5.1, since the laser displacement transducer yields a measurement error for a rock fracture containing colored minerals, the topography measurement was conducted to the silicon gum matrixes. The height of 31 profiles for a fracture

surface, that is, 62 profiles for a specimen were measured with the sampling interval of 50μm in the direction of macroscopic pressure gradient. Since the 1024 data were obtained for a profile, the length of each profile was 51.15mm. In addition, the separation of each profile was 1mm.

5.2.3 Permeability measurement

CMS-300 core measurement system produced by Core Laboratories Instruments was used for the permeability and porosity measurement. This instrument is an automated unsteady state pressure decay permeameter and porosimeter. It can determine the size of cylindrical core specimen, porosity, pore volume, air permeability, Klinkenberg permeability (equivalent liquid permeability), Forchheimer inertial factor and Klinkenberg slippage correction factor. The available confining pressure is from 1.72MPa to 67.57MPa. In addition, the measurable porosity is from 0.01% to 40%, and the measurable permeability is from 0.05 microdarcy to 15darcy, that is, from 4.93E-14mm^2 to 1.48E-5mm^2.

For the epoxy core specimens, the items listed above were measured under the confining pressure of 5.52 MPa, 6.89MPa, 9.65MPa, 12.41MPa and 17.93MPa. By changing the confining pressure, the fracture permeability of different fracture aperture can be obtained. From Figure 5.2, the specimens are supposed to be in elastic condition under such the confining pressure. For each specimen, two pieces of lead sheet 0.5mm thick and 5mm wide were set along the both sides of the fracture to change the fracture aperture widely. The lead sheet can deform plastically following to the topography of fracture surface and it has no pore. Therefore, although it may affect the contact condition of the fracture surface, it was thought to be suitable for a spacer.

Since the matrix porosity of the epoxy core specimen is zero, the measured pore volume is equal to the fracture volume. Therefore, the mean fracture aperture, $<d>$ and hydraulic fracture aperture, d_h, can be calculated by the following equations.

$$< d >= \frac{V_f}{L_x L_y} \tag{5.3}$$

$$d_h = \sqrt[3]{9.86923\times10^{-10}\times12\frac{k_f A_c}{L_y}} \tag{5.4}$$

where V_f is fracture volume, L_x and L_y are fracture length and width respectively, k_f is measured fracture permeability and A_c is cross-sectional area of the core specimen perpendicular to the core axis. Furthermore, applying $<d>$ to the cubic law, the fracture permeability, k_c, that follows the cubic law can be calculated by the next equation.

$$k_c = \frac{1}{9.86923\times10^{-10}} \frac{<d>^3}{12} \frac{L_y}{A_c} \tag{5.5}$$

In Equation (5.4) and Equation (5.5), 9.86923E-10 is a factor to convert the unit of permeability from md (millidarcy) to mm^2.

5.3 The results of the permeability measurement

5.3.1 The results of surface topography measurement

In order to determine the fractal parameters, the variogram was calculated for the 62 profiles and variogram plot was made for each profile. An example of the variogram plot for T4, M2 and I2 is shown in Figure 5.3. The variogram plot is linear in the range of small lag. Therefore, the fractal dimension and steepness can be determined from the slope and the variogram value for the unit lag (1mm) of the straight line respectively.

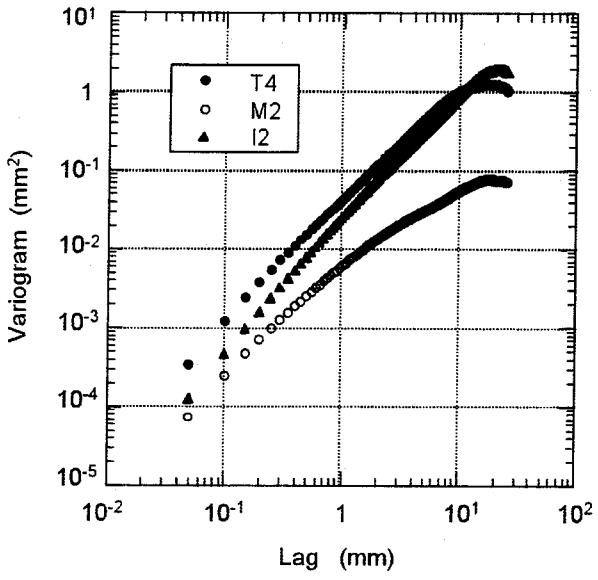

Figure 5.3: An example of the variogram plot for T4, M2 and I2

Table 5.3: The mean value of the fractal dimension, steepness and rms-height.

Specimen Name	Fractal Dimension	S.D.	Steepness (X 10^{-3})	S.D. (X 10^{-3})	RMS Height (mm)
M1	1.257	0.062	8.804	2.85	0.467
M2	1.345	0.032	5.616	0.76	0.216
S1	1.370	0.040	11.500	2.41	0.348
S2	1.365	0.058	8.829	1.62	0.440
T3	1.295	0.099	24.272	6.61	0.743
T4	1.255	0.056	38.592	16.88	0.934
HB	1.244	0.048	16.746	3.71	0.883
I2	1.153	0.035	24.166	10.08	1.029
GPV	1.271	0.042	23.094	5.50	0.553
GSH	1.245	0.054	36.771	12.50	0.721

Thus, the 62 pairs of fractal dimension and steepness were obtained, and then the arithmetic mean for the fractal dimension and steepness was calculated for each specimen. The mean value of the fractal dimension and steepness is shown in Table 5.3 with the standard deviation of them. The rms-height (root mean square height) of the fracture surface is also shown in this table. As shown in Table 5.3, the range of the fractal dimension is from 1.153 to 1.370, and that of the steepness is from 5.616E-3 to 38.592E-3. According to the correlation between steepness and *JRC*, Equation (3.5), the range of the steepness corresponds to the range of *JRC* from 4.14 to 15.78. Thus, the specimens of wide range of surface roughness could be prepared.

5.3.2 The results of the permeability measurement

First, in order to investigate the deviation from the cubic law of measured fracture permeability, k_f/k_c is plotted to $<d>$ in Figure 5.4(a)-(c) in a log-log space. In this figure, the larger the deviation from 1.0 of k_f/k_c, the larger the deviation from the cubic law. As shown in Figure 5.4, k_f/k_c decreases linearly with the increase in $<d>$ in log-log space, and the specimens can be divided into three groups from the slope of each plot. They are Group-A (M1, S2, I2 and GSH) whose slope is from -1.1 to -1.5, Group-B (M2, HB and GPV) whose slope is from -0.5 to -0.8 and Group-C (S1, T3, T4 and FS) whose slope is nearly zero.

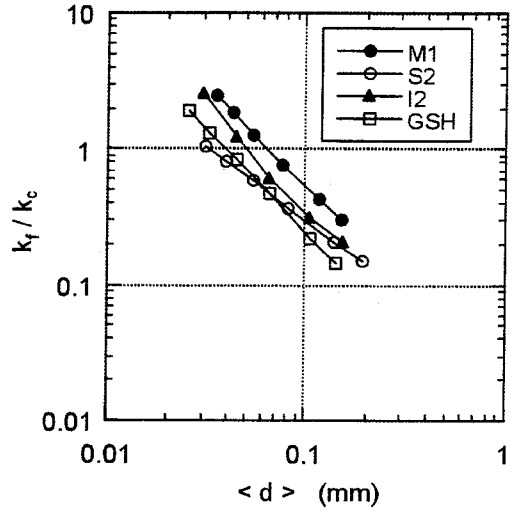

(a) Group-A

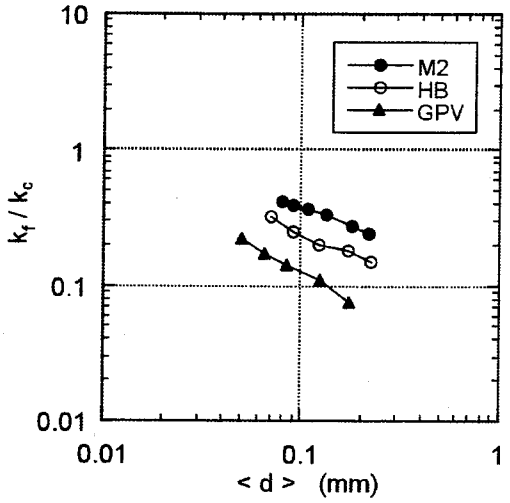

(b) Group-B

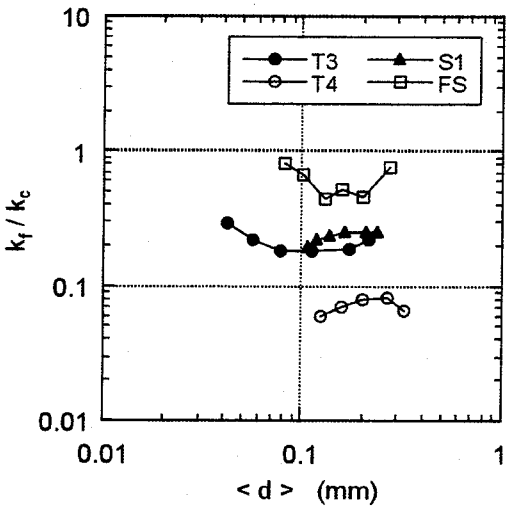

(c) Group-C

Figure 5.4: Relation between the deviation from the cubic law of fracture permeability, k_f/k_c and the mean fracture aperture, $<d>$.

The results shown in Figure 5.4 are contrary to the result of the numerical simulation conducted by Brown (1987). His result is that k_f/k_c decreases with the decrease in d_m/σ, where the d_m is mechanical aperture that is the distance between the mean planes of facing two surfaces and σ is rms-height of the fracture surface. Since d_m and $<d>$ are correlated positively and σ is a constant, k_f/k_c must decrease with the decrease in $<d>$ for their result.

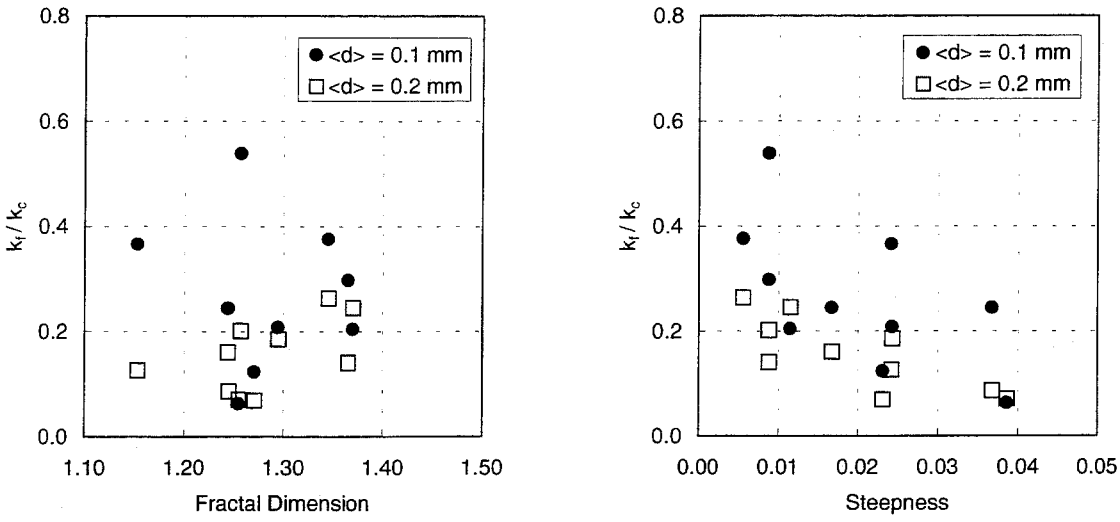

(a) k_f/k_c vs. fractal dimension (b) k_f/k_c vs. steepness

Figure 5.5: The correlation between the deviation from the cubic law of fracture permeability, k_f/k_c, and the fractal parameters

One possible reason for the difference between the results obtained by Brown and the author is as follows. Brown numerically prepared two rough surfaces having the same fractal dimension under the restriction that the four corner points and the four middle points of each side of a fracture are in the mean fracture plane. Then he investigated the k_f/k_c to the d_m/σ ranging from 1.0 to 10.0. In this case, the fracture probably has a large volume even for the small d_m/σ, because the mated two rough surfaces were not correlated well in a small size. On the other hand, the fracture prepared for this study almost interlocked. Therefore, the aperture must be smaller than 0.5mm that is the thickness of the lead spacer. Since the rms-height of most fractures is larger than 0.44mm as shown in Table 5.3, the d_m/σ for this study must be smaller than 1.0 under the confining pressure. For such a small d_m/σ, the deformation of contact asperities makes the fracture volume decrease more with the increase in the confining pressure, and consequently the $<d>$ is estimated small. In addition, fracture permeability does not decrease so much even for such the small d_m/σ, if the flow-path is maintained. As for this study, the neighbor of the lead spacer can be such a flow-path. Consequently, in this study, k_f/k_c can increase with the decrease in $<d>$.

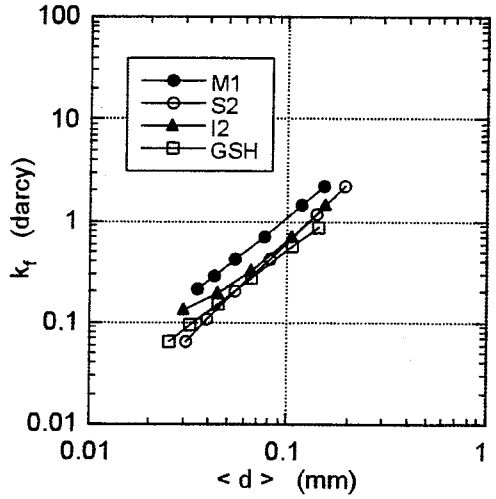

(a) Group-A

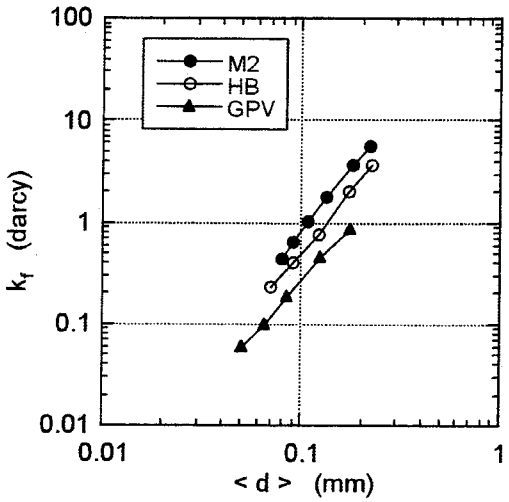

(b) Group-B

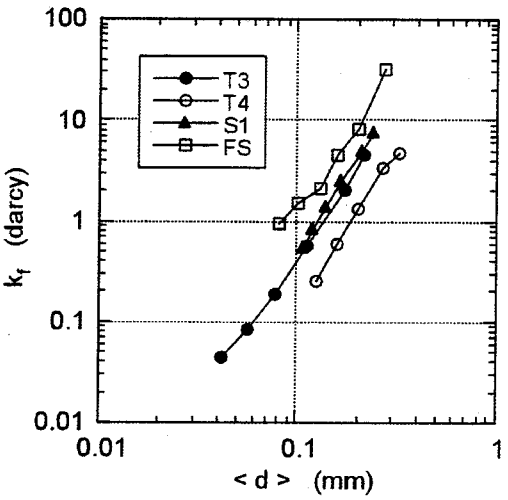

(c) Group-C

Figure 5.6: Relation between the fracture permeability, k_f, and the mean fracture aperture, $<d>$.

Furthermore, the correlation between k_f/k_c and the fractal parameters, that is the fractal dimension and steepness, at the $<d>$ of 0.1mm and 0.2mm are shown in Figure 5.5(a)-(b). For this figure, the value of k_f/k_c at the $<d>$ of 0.1mm and 0.2mm are determined by the value of the approximated function. From Figure 5.5, the clear correlation between k_f/k_c and the fractal dimension can not be seen, but a negative correlation between k_f/k_c and the steepness can be recognized. The correlation coefficient is -0.62 at the $<d>$ of 0.1mm and -0.78 at the $<d>$ of 0.2mm.

Therefore, it can be said that k_f/k_c decreases with the increase in the steepness.

Second, for each group, k_f was plotted to $<d>$ in a log-log space. The plots are shown in Figure 5.6(a)-(c). For every group, k_f increases linearly with the increase in $<d>$, and the next relation can be recognized between them.

$$k_f = a < d >^b \tag{5.6}$$

where a and b are a constant. The value of b obtained from the slope of each plot is from 1.47 to 1.92 for Group-A, from 2.17 to 2.49 for Group-B and from 2.83 to 3.26 for Group-C.

The value of b shows how the deviation from the cubic law depends on $<d>$. The deviation from the cubic law does not depend on $<d>$ when b is equal to 3.0, and the dependence on $<d>$ is stronger with the increase in the difference of b from 3.0. Therefore, the deviation from the cubic law of Group-A whose b is largely different from 3.0 is strongly dependent on $<d>$, but that of Group-C whose b is nearly equal to 3.0 is independent of $<d>$. This can be known from Figure 5.4, and the difference in b is probably caused by the difference in the contact condition of the fracture surfaces.

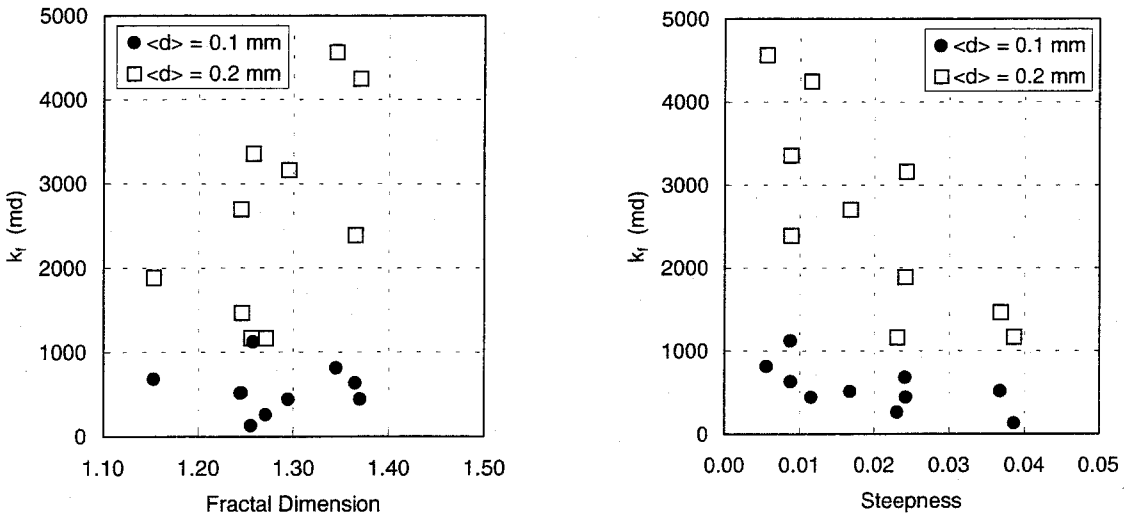

(a) k_f vs. fractal dimension

(b) k_f vs. steepness

Figure 5.7: The correlation between the fracture permeability, k_f, and the fractal parameters.

Furthermore, the correlation between k_f and the fractal parameters at the <d> of 0.1mm and 0.2mm are shown in Figure 5.7(a)-(b). From Figure 5.7, at the <d> of 0.2mm, a positive correlation between k_f and the fractal dimension whose correlation coefficient is 0.582 can be recognized, but at the <d> of 0.1mm, no clear correlation between them can be recognized. On the other hand, a negative correlation between k_f and the steepness can be recognized at both values of <d>. The correlation coefficient is -0.657 at the <d> of 0.1mm and -0.779 at the <d> of 0.2mm. Therefore, it can be said that k_f decreases with the increase in the steepness. As for the fractal dimension, clear conclusion can not be derived.

Last, k_f was plotted to the confining pressure, P_c, in a log-log space. That is shown in Figure 5.8. From this figure, it can be recognized that k_f linearly decreases with the increase in P_c in a log-log space, and the relation between them can be represented as

$$k_f = aP_c^{-b} \quad (b = 2.0 \sim 3.0) \tag{5.7}$$

where a and b are a constant.

Walsh (1981) theoretically represented the relation between $k_f^{1/3}$ and effective confining pressure, P_e, as following equation.

$$k_f^{1/3} = a - b\ln P_e \tag{5.8}$$

where a and b are a constant and P_e is given by the following equation.

$$P_e = P_c - sP_p \tag{5.9}$$

where s is a constant and P_p is pore pressure.

Since the P_p is nearly equal to zero for this permeability measurement, P_e is nearly equal to P_c. Therefore, in order to check the validity of Equation (5.8), $k_f^{1/3}$ was plotted to P_c in a semi-log space. That is shown in Figure 5.9. From this figure, Equation (5.8) is almost valid, but Equation (5.7) is more suitable for the result of this study.

In order to derive Equation (5.8), Walsh adopted the following logarithmic relation between a fracture aperture, d, and a normal stress, P, based on the contact theory of Greenwood and Williamson (1966).

$$d = a - b\ln P \tag{5.10}$$

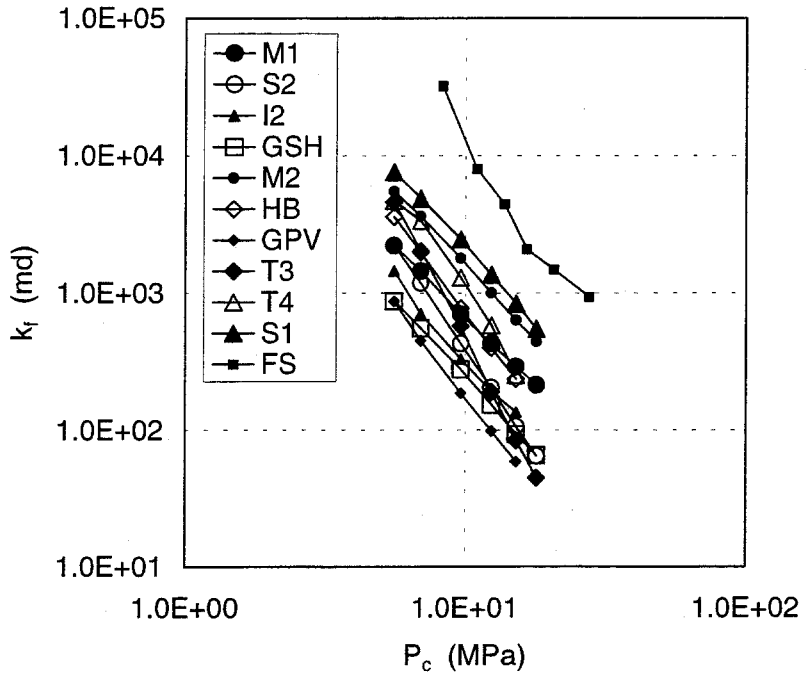

Figure 5.8: The relation between the fracture permeability, k_f, and the confining pressure, P_c.

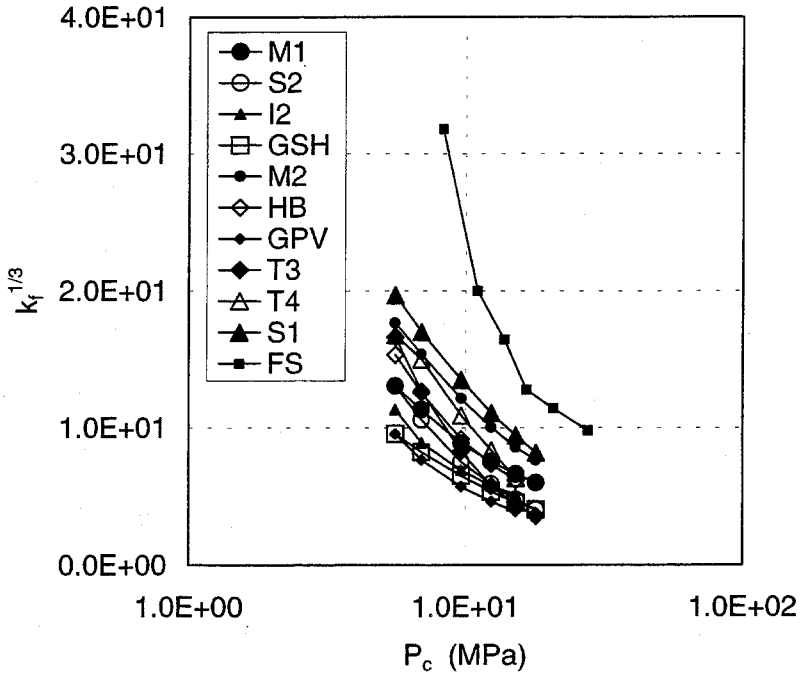

Figure 5.9: The relation between the fracture permeability, $k_f^{1/3}$, and the confining pressure, P_c.

where a and b are a constant. The same relation was presented by Goodman (1976). However, if the hyperbolic relation between them presented by Barton *et al.* (1985) is adopted, the relation between $k_f^{1/3}$ and P can be represented by a following hyperbolic function.

$$k_f^{1/3} = \frac{c + aP}{1 + bP} \tag{5.11}$$

where a, b and c are a constant. Thus, the relation between fracture permeability and confining pressure depends on the relation between fracture aperture and normal stress. Therefore, the reason why Equation (5.7) is more suitable than Equation (5.8) can be thought that the relation between fracture aperture and normal stress of each specimen does not follow Equation (5.10) exactly.

5.4 Deviation from the cubic law of fracture permeability described by a fractal model

5.4.1 Fracture permeability described by the equivalent channel model

Since the pore structure of a porous media is very complex, the fluid flow in it is very tortuous as shown in Figure 5.10(a). In order to represent such a tortuous fluid flow, Paterson (1983), Walsh and Brace (1984) presented the equivalent channel model as shown in Figure 5.10(b). As Brown (1989) pointed out, the essence of the equivalent channel model is to assume that there is a "typical" pore, which when bundled with many others describes the behavior of the whole. In addition, in this model, one also includes the possibility that the channels are not straight, but wind around through the specimen, so that the actual path length of the fluid is larger than the nominal length of the specimen. Therefore, this model assumes that the distribution of pore spaces is isotropic and all pore spaces are involved in the flow process; in other word, dead end, stagnant regions and isolated pore are neglected. For the fracture flow, these assumptions are satisfied in the fracture. Therefore, the equivalent channel model is applicable to the fluid flow through a fracture. In this section, the permeability of general rough fracture and that of parallel smooth plates are represented by the equivalent channel model. In addition, the deviation from the cubic law of fracture permeability is represented by the ratio of the former permeability to the latter permeability.

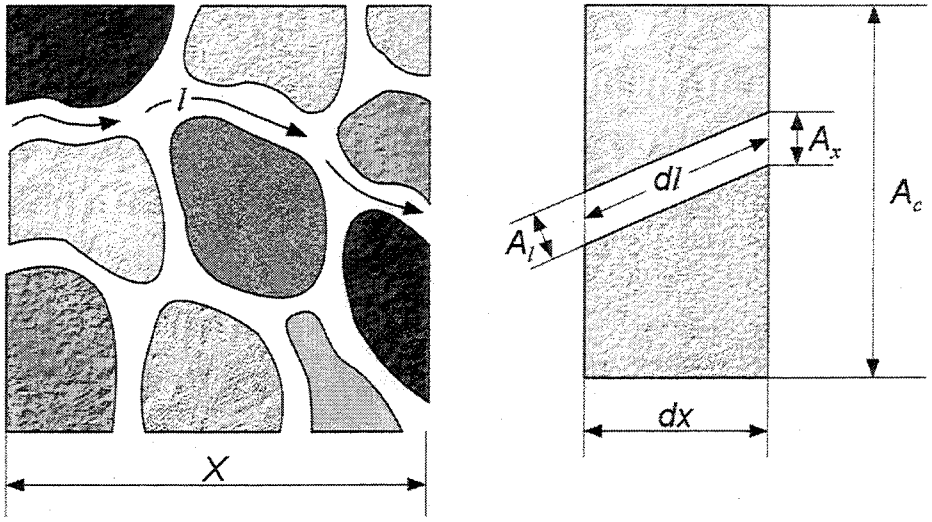

(a) Tortuous flow-path shown by the streamline (b) Representative section of the network

Figure 5.10: Geometry used in the equivalent channel model. (Redrawn from Walsh and Brace, 1984).

For the equivalent channel model, average fluid velocity v_l along the streamline shown in Figure 5.10(a) can be give by the following equation (see, for example Brace et al.; 1968).

$$v_l = -\left(\frac{m^2}{\beta\mu}\right)\left(\frac{dp}{dl}\right) \tag{5.12}$$

where m, hydraulic radius, is the ratio of the pore volume to the wetted area, β is a shape factor of pore, which is 2.0 for cylindrical tubes and 3.0 for parallel plates, μ is fluid viscosity. In addition, dp/dl is pressure gradient along the streamline. The pressure gradient, dp/dl, is related to the pressure gradient with respect to the specimen axis by

$$\frac{dp}{dl} = \frac{1}{\tau}\frac{dp}{dx} \tag{5.13}$$

where τ is tortuosity that is defined by the ratio of the actual path length to the nominal length of the specimen:

$$\tau = \frac{dl}{dx} \tag{5.14}.$$

The total flow rate, q, through the equivalent channel is represented by

$$q = v_l A_l \tag{5.15}$$

where A_l is the cross-sectional area of the equivalent channel perpendicular to the streamline. In addition, from Figure 5.10(b), A_l is related to the cross-sectional area of the equivalent channel perpendicular to the specimen axis, A_x, by

$$A_l = \frac{A_x}{\tau} \tag{5.16}.$$

The porosity, ϕ, of a specimen with the isotropic distribution of pore can be obtained by

$$\phi = \frac{A_x}{A_c} \tag{5.17}$$

where A_c is the cross-sectional area of the specimen.

From the Darcy's law, the permeability of a general rough fracture can be represented as next equation.

$$k_f = \left(\frac{q\mu}{A_c}\right) \Big/ \left(\frac{dp}{dx}\right) \tag{5.18}$$

Therefore, from Equation (5.12) to Equation (5.17), the permeability can be rewritten as following equation.

$$k_f = \frac{m^2}{\beta} \frac{\phi}{\tau^2} \tag{5.19}$$

Since the hydraulic radius is defined by

$$m = \frac{1}{2} \frac{\phi V_b}{A_f} \tag{5.20}$$

where V_b is bulk volume, A_f is surface area of the fracture. Substituting Equation (5.20) into Equation (5.19), the permeability of a general rough fracture can be presented by the following equation.

$$k_f = \frac{1}{4} \frac{\phi^3 V_b^{\,2}}{\beta \tau^2 A_f^{\,2}} \tag{5.21}.$$

On the other hand, the permeability of parallel smooth plates can be represented by substituting 3.0 for β, A for A_f and 1.0 for τ in Equation (5.21):

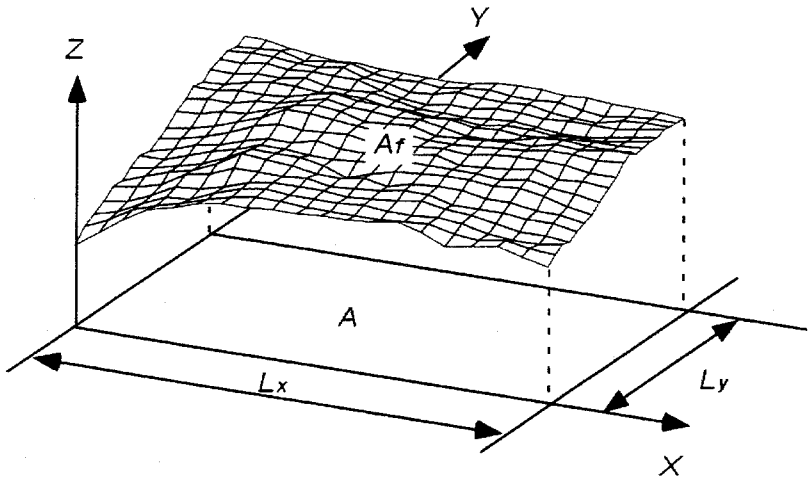

Figure 5.11: The relation between the fracture surface area, A_f, and the nominal fracture area, A.

$$k_f = \frac{1}{12}\frac{\phi^3 V_b^{\ 2}}{A^2} \tag{5.22}$$

where A is the area of parallel plates. Since the fracture volume, V_f, is represented by

$$V_f = dA = \phi V_b \tag{5.23}$$

where d is the aperture of parallel plates, eliminating A from Equation (5.22), the permeability of parallel plates can be represented by

$$k_f = \frac{1}{12}\phi d^2 \tag{5.24}$$

From Equation (5.24) and Darcy's law, the volumetric flow rate, q, can be represented by

$$q = -L_y \frac{d^3}{12\mu}\frac{dp}{dx} \tag{5.25}$$

where L_y is the width of parallel plates. This equation is equal to Equation (5.1), which represents the cubic law. Therefore, it can be said that the permeability represented by Equation (5.22) is the permeability that follows the cubic law. From Equation (5.21) and Equation (5.22), rewriting k_f with k_c in Equation (5.22), the

deviation from the cubic law of fracture permeability, k_f/k_c, can be represented by the following equation.

$$\frac{k_f}{k_c} = \frac{3}{\beta\tau^2 (A_f/A)^2} \tag{5.26}$$

where A is nominal fracture area, which is equal to the area of parallel plates. The relation between the fracture surface area, A_f, and the nominal fracture area, A, is drawn in Figure 5.11.

5.4.2 Deviation from the cubic law of fracture permeability described by using a fractal model

The deviation from the cubic law of fracture permeability can be represented by the fractal parameters, because the all parameters in the right hand side of Equation (5.26) depend on the geometry of fracture surfaces.

As shown in chapter 2, for the profile of a self-affine fractal, the fractal model represented by variogram method is given by the following equation.

$$\gamma(h) = Vh^{4-2D} \qquad (1 < D < 2) \tag{5.27}$$

where $\gamma(h)$ is variogram function, V is steepness and D is fractal dimension. For the profile of a fracture surface, the variogram function is practically calculated from the following experimental semi-variogram function.

$$\gamma(h) = \frac{1}{2N}\sum_{i=1}^{N}[z(x_i) - z(x_i + h)]^2 \tag{5.28}$$

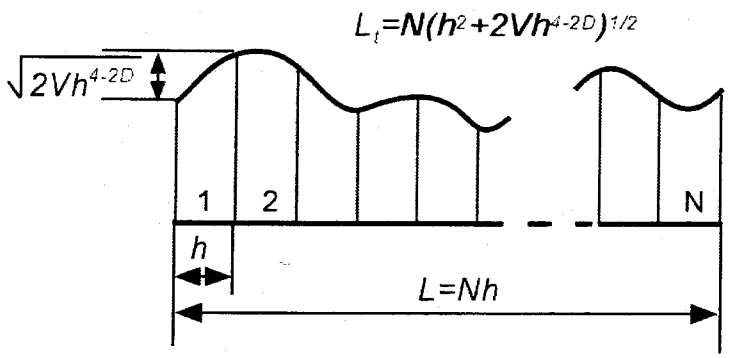

Figure 5.12: Explanation of flow-path length along a fractal surface measured by h.

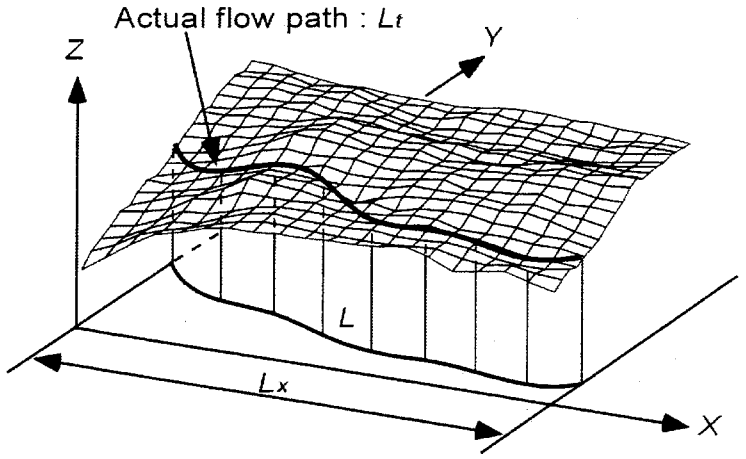

Figure 5.13: The actual flow-path length on the fracture surface, L_t, the projected flow-path length on the XY-plane, L, and the nominal fracture length, L_x. The XY-plane is parallel to the nominal pressure gradient.

where N is the number of pairs of data whose lag is h and $z(x)$ is the profile height at point x. From this equation, it is implicit that the twice of the variogram is the mean of the square of height difference between the two data points. Therefore, as explained by Figure 5.12, the ratio of the actual flow-path length to the projected flow-path length on the XY-plane, L_t/L, can be approximately represented by using the fractal dimension and steepness:

$$\frac{L_t}{L} = (1 + 2Vh^{2-2D})^{1/2} \tag{5.29}$$

Here, the actual flow-path length on the fracture surface, L_t, the projected flow-path length on the XY-plane, L, and the nominal fracture length, L_x, are explained in Figure 5.13. Therefore, supposing the isotropy of surface geometry, the ratio of the fracture surface area to the nominal fracture area, A_f/A, can be approximately represented by the following equation.

$$\frac{A_f}{A} = 1 + 2Vh^{2-2D} \tag{5.30}$$

On the other hand, from Equation (5.29) and Equation (5.31), the tortuosity, τ, is represented by

$$\tau = \frac{L_t}{L_x} = \alpha(1 + 2Vh^{2-2D})^{1/2} \tag{5.31}$$

Table 5.4: The fracture shape factor, β, of various cross section shape (after Schön, 1996).

Cross Section Shape		β
Circle		2.0
Ellipse, semi-axes a and b	a/b = 2	2.13
	a/b = 10	2.45
	a/b = 50	2.96
Square		1.78
Rectangle, sides a and b	a/b = 2	1.94
	a/b = 10	2.65
	a/b = infinity	3.0
Triangle, equilateral		1.67

where α is defined by

$$\alpha = \frac{L}{L_x} \tag{5.32}$$

and called two-dimensional tortuosity in this thesis.

Consequently, from Equation (5.26), Equation (5.30) and Equation (5.31), the deviation from the cubic law of fracture permeability can be represented by the following equation:

$$\frac{k_f}{k_c} = \frac{3}{\beta\alpha^2(1+2Vh^{2-2D})^3} \tag{5.33}$$

In this equation, the term, $(1+2Vh^{2-2D})^3$, can represent the effect of surface roughness of a fracture. In this term, h corresponds to the size of asperity along which fluid flows faithfully, and the author will called it control size in this thesis. In addition, the two-dimensional tortuosity can be mainly caused by the random aperture distribution that is affected by the contact condition of fracture surfaces. Therefore, the terms, α^2, can represent the effect of the contact condition of fracture surfaces.

5.4.3 Discussion

First, the reason why k_f/k_c increased with decrease in the mean fracture aperture, $<d>$, in the experimental results is discussed based on Equation (5.26). The contact of fracture surfaces will advance with the increase in confining pressure. Consequently, the $<d>$ decreases and the cross-sectional shape of the fracture changes from parallel plates into tube-like. Since the shape factor, β, takes the

values listed in Table 5.4 (after Schön, 1996), β gradually decreases from 3.0 to 2.0 or less with the decrease in $<d>$. Therefore, if the tortuosity does not change so large with the decrease in $<d>$ in the experiment, k_f/k_c will increase with the decrease in $<d>$. In the experiment, such the situation that the tortuosity does not change so large must have been accomplished by the existence of lead spacers.

Second, the effect of the fractal dimension, D, steepness, V, and two-dimensional tortuosity, α, on the deviation from the cubic law of fracture permeability, k_f/k_c, is discussed based on Equation (5.33). Judging from the values of the shape factor, β, for ellipses or rectangles shown in Table 5.4, β for a fracture may range from 2.0 to 3.0. On the other hand, it is reasonable to think that the control size, h, must be equal to the interlocking wavelength, because it can be thought that the fluid flows faithfully along the interlocking asperities whose wavelength is larger than the interlocking wavelength. According to Brown and Scholz (1985a, 1985b), the interlocking wavelength of a fracture ranges from 0.1mm to 10mm. Furthermore, the contact area of a fracture is generally small. Therefore, assuming β=3.0, k_f/k_c was calculated for the next nine cases by using Equation (5.33).

For h=0.1mm,

Case-1-1: D=1.2, V=0.02 and α=1.0, 1.1, 1.2, 1.3, 1.4 and 1.5.

Case-1-2: α=1.2, V=0.02 and D=1.0, 1.1, 1.2, 1.3, 1.4 and 1.5

Case-1-3: α=1.2, D=1.2 and V=0.005, 0.01, 0.02, 0.03, 0.04 and 0.05

For h=0.5mm,

Case-2-1: D=1.2, V=0.02 and α=1.0, 1.1, 1.2, 1.3, 1.4 and 1.5.

Case-2-2: α=1.2, V=0.02 and D=1.0, 1.1, 1.2, 1.3, 1.4 and 1.5

Case-2-3: α=1.2, D=1.2 and V=0.005, 0.01, 0.02, 0.03, 0.04 and 0.05

For h=10.0mm,

Case-3-1: D=1.2, V=0.02 and α=1.0, 1.1, 1.2, 1.3, 1.4 and 1.5.

Case-3-2: α=1.2, V=0.02 and D=1.0, 1.1, 1.2, 1.3, 1.4 and 1.5

Case-3-3: α=1.2, D=1.2 and V=0.005, 0.01, 0.02, 0.03, 0.04 and 0.05

The typical values of each parameter for a rock fracture are probably in the above ranges. The results for each h are shown in Table 5.5(a)-(c) respectively.

From these tables, the followings can be concluded. First, k_f/k_c decreases with the increase in α, and the effect of α on k_f/k_c is more remarkable than that of D and V when h is large. Since α is thought to be mainly affected by the contact of fracture surfaces, k_f/k_c must be largely affected by it when h is large. Second, the effect of D

Table 5.5: The results of sensitivity check of the fractal dimension, D, steepness, V, and two-dimensional tortuosity, α, on the deviation from the cubic law of fracture permeability, k_f/k_c, for the interlocking wavelength, h, of 0.1mm, 0.5mm, 10.0mm.

(a) h=0.1mm

Case-1-1 D=1.2, V=0.02		Case-1-2 α=1.2, V=0.02		Case-1-3 α=1.2, D=1.2	
α	k_f/k_c	D	k_f/k_c	V	k_f/k_c
1.0	0.750	1.0	0.617	0.005	0.645
1.1	0.620	1.1	0.578	0.010	0.599
1.2	0.521	1.2	0.521	0.020	0.521
1.3	0.444	1.3	0.446	0.030	0.456
1.4	0.383	1.4	0.354	0.040	0.401
1.5	0.333	1.5	0.253	0.050	0.355

(b) h=0.5mm

Case-2-1 D=1.2, V=0.02		Case-2-2 α=1.2, V=0.02		Case-2-3 α=1.2, D=1.2	
α	k_f/k_c	D	k_f/k_c	V	k_f/k_c
1.0	0.857	1.0	0.617	0.005	0.668
1.1	0.708	1.1	0.607	0.010	0.642
1.2	0.595	1.2	0.595	0.020	0.595
1.3	0.507	1.3	0.582	0.030	0.553
1.4	0.437	1.4	0.567	0.040	0.514
1.5	0.381	1.5	0.551	0.050	0.479

(c) h=10.0mm

Case-3-1 D=1.2, V=0.02		Case-3-2 α=1.2, V=0.02		Case-3-3 α=1.2, D=1.2	
α	k_f/k_c	D	k_f/k_c	V	k_f/k_c
1.0	0.954	1.0	0.617	0.005	0.686
1.1	0.788	1.1	0.644	0.010	0.678
1.2	0.662	1.2	0.662	0.020	0.662
1.3	0.564	1.3	0.674	0.030	0.647
1.4	0.487	1.4	0.681	0.040	0.632
1.5	0.424	1.5	0.686	0.050	0.618

on k_f/k_c decreases with increase in h. In addition, k_f/k_c decreases with increase in D when h is less than 1.0mm, but it increases with the increase in D when h is larger than 1.0mm. Third, k_f/k_c decreases with increase in V, and the effect of V on k_f/k_c decreases with the increase in h.

5.5 Conclusions

In this chapter, the deviation from the cubic law of fracture permeability was

investigated experimentally and theoretically. Consequently, it was represented quantitatively by using the fractal parameters, and the followings were clarified.

1) Fracture permeability, k_f, linearly increases with the increase in the mean fracture aperture, $<d>$, in a log-log space, and the relation, $k_f=a<d>^b$, can be recognized between them. The value of b is probably dependent on the contact condition of fracture surfaces. In addition, k_f decreases with the increase in the steepness.
2) Fracture permeability, k_f, linearly decreases with the increase in confining pressure, P_c, in a log-log space, and the relation, $k_f=aP_c^{-b}$ (b=2.0~3.0), can be recognized between them. The style of the relation depends on the closure behavior of a fracture.
3) The deviation from the cubic law of fracture permeability increases with the increase in two-dimensional tortuosity. The effect of it is more remarkable than that of fractal dimension and steepness when the control size is large.
4) The effect of fractal dimension on the deviation from the cubic law of fracture permeability decreases with increase in the control size.
5) The deviation from the cubic law of fracture permeability increases with increase in steepness. In addition, the effect of steepness on it decreases with the increase in the control size.
6) It is possible that the deviation from the cubic law of fracture permeability decreases with the decrease in mean fracture aperture, if the tortuosity does not change so large with the decrease in the mean fracture aperture.

Among the parameters discussed above, the two-dimensional tortuosity, which is an important parameter to determine the fracture permeability, is difficult to be estimated theoretically, because it depends on the random distribution of fracture aperture. Therefore, many physical or numerical experiments to visualize the streamline in a fracture must be carried out, and the relation between the two-dimensional tortuosity and the contact area, interlocking wavelength and fractal parameters must be clarified.

References

Barton, N., S. Bandis, and K. Bakhtar, Strength, deformation and conductivity coupling of rock joints, *Int. J. Rock Mech. Min. Sci. & Geomech. Abstr.*, Vol. 22, 121-140, 1985.

Brace, W. F., J. B. Walsh and W. T. Frangos, Permeability of granite under high pressure, *J. Geophys. Res.*, Vol. 73, 2225-2236, 1968.

Brown, S. R. and C. H. Scholz, Closure of random elastic surfaces in contact, *J. Geophys. Res.*, Vol. 90, 5531-5545, 1985a.

Brown, S. R. and C. H. Scholz, Broad bandwidth study of the topography of natural rock surfaces, *J. Geophys. Res.*, Vol. 90, 12575-12582, 1985b.

Brown, S. R., Fluid flow through rock joints: the effect of surface roughness, *J. Geophys. Res.*, Vol. 92, 1337-1347, 1987.

Brown, S. R., Transport of fluid and electric current through a single fracture, *J. Geophys. Res.*, Vol. 94, 9429-9438, 1989.

Goodman, R. E., *Method of geological engineering in discontinuous rocks*, West Publishing Company, 1976.

Greenwood, J. A. and J. B. P. Williamson, Contact of nominally flat surfaces, *Proc. R. Soc. London*, Vol. A295, 300-319, 1966.

Lomize, G. M., Flow in fractured rocks (*in Russian*), 127 pp., *Geosenergoizdat*, Moscow, 1951.

Louise, C., A study of groundwater flow in jointed rock and its influence on the stability of rock masses, *Rock Mech. Res. Rep.*, 10, 90 pp., Imp. Coll., London, 1969.

Paterson, M. S., The equivalent channel model for permeability and resistivity in fluid saturated rocks-A reappraisal, *Mech. Mater.*, Vol. 2, 345-352, 1983.

Schön, J. H., *Physical properties of rocks: fundamentals and principles of petrophysics*, Elsevier, 1996.

Walsh, J. B., Effect of pore pressure and confining pressure on fracture permeability, *Int. J. Rock Mech. Min. Sci. & Geomech. Abstr.*, Vol. 18, 429-435, 1981.

Walsh, J. B. and W. F. Brace, The effect of pressure on porosity and the transport properties of rock, *J. Geophys. Res.*, Vol. 89, 9425-9431, 1984.

CHPTER6

THE EFFECT OF TORTUOSITY ON THE FRACTURE PERMEABILITY

6.1 Introduction

In order to estimate the fluid flow in a fractured rock mass, it is necessary to understand the behavior of fluid flow in a single fracture as well as the heterogeneous distribution of the fractures in a rock mass. Generally, the fracture permeability has been estimated by the cubic law that is valid for the laminar flow between two perfectly smooth parallel plates. However, it is difficult to represent such a complex fracture by a simple parallel plates model, since the actual fracture surfaces are very complex and there are some contact parts on them.

To overcome this difficulty, in Chapter 5, such the complex fracture was represented by a fractal model, and the deviation from the cubic law of fracture permeability was investigated experimentally and theoretically. Consequently, it was represented by using the fractal parameters as Equation (5.33):

$$\frac{k_f}{k_c} = \frac{3}{\beta\alpha^2\left(1+2Vh^{2-2D}\right)^3} \tag{6.1}$$

where k_f is the permeability of a general rough fracture, k_c is the permeability of parallel smooth plates, β is fracture shape factor. In addition, α is two-dimensional tortuosity, V is steepness and D is fractal dimension. The fracture shape factor is 2.0 for cylindrical tube and 3.0 for parallel plates. Moreover, the two-dimensional tortuosity is defined by the ratio of projected flow path length on the plane that is parallel to the nominal pressure gradient to the fracture length.

Among these parameters, the two-dimensional tortuosity is an important parameter to determine the fracture permeability, but it is very difficult to estimate it theoretically because of its dependence on the random distribution of fracture aperture. Therefore, in order to estimate it, we must carry out many physical or numerical experiments to visualize the streamlines in a fracture and clear the relation between the two-dimensional tortuosity and the contact area, interlocking wavelength, fractal parameters.

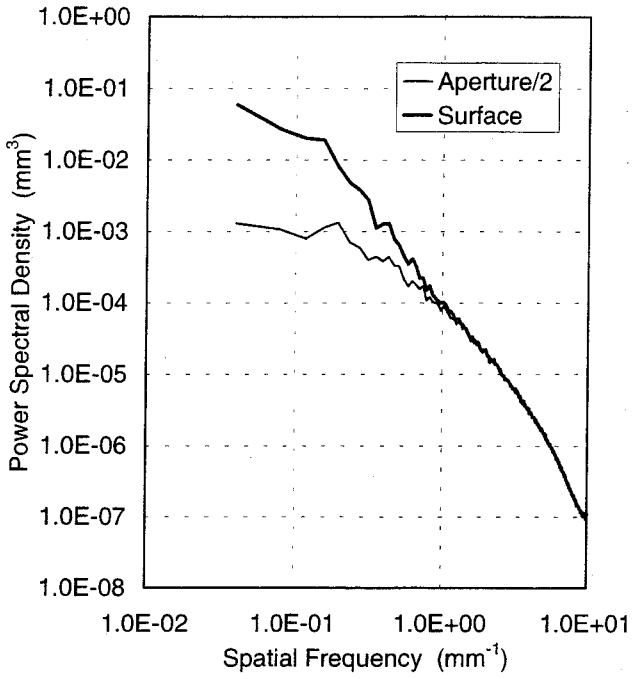

Figure 6.1: PSD function of fracture surface profile and fracture aperture profile. The PSD function of fracture aperture profile is shown by half of it to show the difference between them clearly.

For this reason, in this chapter, the physical flow experiments and numerical flow simulations to visualize the streamlines in a fracture are carried out for the interlocking and non-interlocking fractures. These fractures are artificially generated by using the fractal model. In addition, for these fractures, the validity of Equation (6.1) is discussed by comparing the k_f/k_c among the theoretical equation, the physical flow experiments and the numerical flow simulation.

6.2 Visualization of fluid flow through fractures

6.2.1 Method to generate an aperture distribution of fracture based on the fractal model

As described in Chapter 2, fracture surfaces are self-affine fractal. The PSD (power spectral density) function of their profile shows decaying power law that can be described as

$$G(f) = Cf^{-(5-2D)} \tag{6.2}$$

where D is fractal dimension and C is a constant. On the other hand, as shown in Figure 6.1, the PSD function of a fracture aperture profile flattens at the larger wavelengths than the interlocking wavelength. This is because two fracture surfaces composing a fracture are often closely matched at large wavelengths and mismatched at small wavelengths. In order to generate such a fracture aperture distribution numerically, Brown (1995) presented a method based on the two-dimensional Fourier filtering method (see Peitgen and Saupe; 1988).

The two-dimensional Fourier filtering method generates a self-affine fracture surface by constructing a two-dimensional complex amplitude spectrum with a random phase component which obeys the decaying power law, and then by operating an inverse Fourier transform of the amplitude spectrum. Therefore, in this method, the fractal dimension and steepness of a generated fracture surface are adjusted according to the slope and intersection of the decaying power law respectively. Here, the steepness was especially adjusted by multiplying a factor called steepness factor by the complex amplitude spectrum. In order to force two surfaces of a fracture to be matched at large wavelengths, Brown generated two surfaces by using the same random phase spectrum in the lower frequency and the identical random phase spectrum in the higher frequency. The length scale at which the phase spectrum of the two surfaces becomes different is equal to the interlocking wavelength. However, the PSD function of the aperture profile generated by Brown's method suddenly flattens or decreases at the interlocking wavelength as shown in Figure 6.2(a). This PSD function is different from that of a natural aperture profile as shown in Figure 6.1. The PSD function of a natural aperture profile gradually flattens at the wavelengths larger than the interlocking wavelength.

In order to overcome this problem, Glover *et al.* (1997) modified the Brown's method. They used two independent random numbers, *R1* and *R2*, for the wavelengths smaller than the half of the interlocking wavelength. In addition, for the larger wavelengths, they mixed these two random numbers linearly to form the third random number, *R3*, according to the following equation.

$$R3 = \lambda R1 + (1-\lambda)R2 \tag{6.3}$$

where λ is a function of the spatial frequency, f;

$$\lambda = \zeta\left(1-\frac{f}{2f_c}\right) \tag{6.4}$$

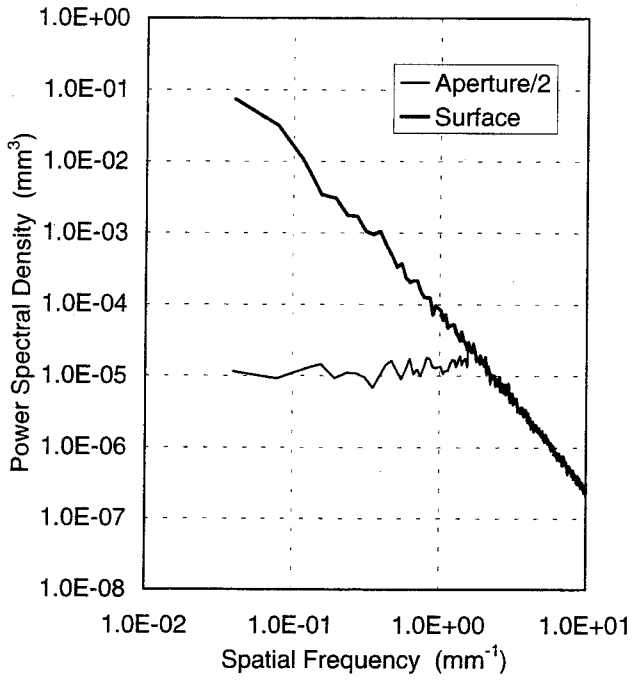

(a) For the fracture generated by Brown's method.

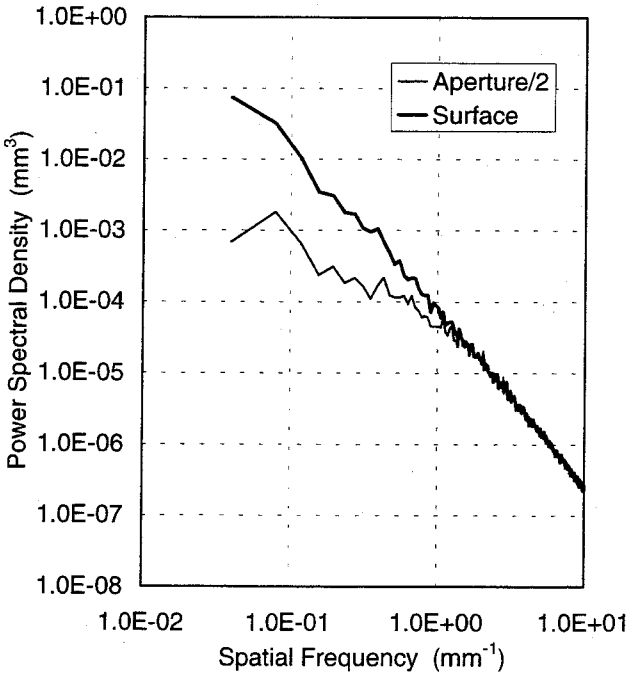

(b) For the fracture generated by Glover's method.

Figure 6.2: PSD function of fracture surface profile and fracture aperture profile for the fracture generated by Brown's method, (a) and Glover's method, (b).

```
CC*************************************************************
C  n          :  Matrix size
C  h          :  Hurst exponent (0.5 <= h <= 1.0)
C  steepf     :  Steepness factor
C  dt         :  Sampling interval
C  aniso      :  Anisotrophy factor (aniso : 1.0=isotropy)
C  mismch     :  Interlocking wavenumber
C  roff       :  Roll-off parameter (0 < roff < 1.0)
C  iseed      :  Random number seed
C  urand()    :  Uniform random number generator
C  nrand()    :  Normal random number generator
C  ifft2d()   :  Inverse 2-D Fourier transform
CC*************************************************************
START
C       ----------------------------------
          call urand(rand1,iseed)
          call urand(rand2,iseed)
          call nrand(randg,iseed)
C       ----------------------------------
       do 1000 icunt=1,2
       do 100 i=0,n/2
          do 200 j=0,n/2
             if(icunt .le. 1) then
                phase=2.0*pi*rand1
             else
                wnum=sqrt(real(i*i+j*j))
                if (wnum .lt. mismch) then
                   fact=wnum/mismch
                   myu=roff*(1.0-fact)
                   rand3=myu*rand1+(1.0-myu)*rand2
                   phase=2.0*pi*rand3
                else
                   phase=2.0*pi*rand2
                end if
             end if
             if((i .eq. 0) .and. (j .eq. 0)) then
                rad=0.0
             else
                rad=(i*i+j*j/(aniso*aniso))**(-(h+1.0)/2.0)
                rad=steepf*rad*randg
             end if
             gn0(i,j)=cmplx(rad*cos(phase),rad*sin(phase))
             if(i .eq. 0) then
                i0=0
             else
                i0=n-i
             end if
             if(j .eq. 0) then
                j0=0
             else
                j0=n-j
             end if
             gn0(i0,j0)=cmplx(rad*cos(phase),-1.0*rad*sin(phase))
 200      continue
 100   continue
C
       gn0(n/2,0)=cmplx(real(gn0(n/2,0)),0)
       gn0(0,n/2)=cmplx(real(gn0(0,n/2)),0)
       gn0(n/2,n/2)=cmplx(real(gn0(n/2,n/2)),0)
       do 300 i=1,n/2-1
          do 400 j=1,n/2-1
             if(icunt .le. 1) then
                phase=2.0*pi*rand1
             else
                wnum=sqrt(real(i*i+j*j))
                if (wnum .lt. mismch) then
                   fact=wnum/mismch
                   myu=roff*(1.0-fact)
                   rand3=myu*rand1+(1.0-myu)*rand2
                   phase=2.0*pi*rand3
                else
                   phase=2.0*pi*rand2
                end if
             end if
             rad=(i*i+j*j/(aniso*aniso))**(-(h+1.0)/2.0)
             rad=steepf*rad*randg
             gn0(i,n-j)=cmplx(rad*cos(phase),rad*sin(phase))
             gn0(n-i,j)=cmplx(rad*cos(phase),-1.0*rad*sin(phase))
 400      continue
 300   continue

C    ----------------------------------
       call ifft2d(gn0, n, work)
C    ----------------------------------

1000   continue
END
```

Figure 6.3: Algorithm of Glover's method described by Fortran cord.

where f_c is interlocking frequency and ζ is called roll-off parameter that represents the maximum fractional matching achieved at the largest wavelength and controls the extent to which the PSD function of the generated aperture profile flattens off at large wavelengths. Consequently, the random phase spectrum gradually changes from matching condition to mismatching condition.

The algorithm of this method is shown in Figure 6.3. In addition, an example of the PSD functions of a fracture surface profile and aperture profile generated by this method is shown in Figure 6.2(b). It can be noted that the problems encountered by Brown's method are no longer present, and the PSD function similar to that of natural aperture profile is obtained. Therefore, the author used Glover's method to generate an aperture distribution of the artificial fractures used for the physical flow experiment and the numerical flow simulation.

6.2.2 The physical flow experiments

First, the fractures for the physical flow experiments were prepared by the following ways. An artificial fracture surface can be generated on a material, such as metal, chemical wood, paraffin and so on, by carving it with a numerical controlled (NC) modeling machine according to the numerical height data of the fracture surface. The numerical height data were generated on the 256 by 256 points whose interval is 0.2mm by using the Glover's method. Therefore, the generated fracture surface is 51mm wide and 51mm long. The NC-modeling machine used here is PNC-300G produced by Roland DG, and the carved material is a modeling wax, which is a kind of paraffin. As mentioned in Section 6.2.1, the Glover's method numerically generates two fracture surfaces composing a fracture. Therefore, a physical fracture can be generated by carving them individually and mating them together. It is worth noting that any desired fracture can be easily prepared by this method, though it is very difficult to do so by sampling natural fractures.

Two types of fractures were prepared for the physical flow experiment. They are interlocking fractures and non-interlocking fractures. The interlocking fracture were prepared by copying the carved two surfaces composing a fracture with white silicon gum and transparent acrylic resin individually and mating the copies together. In addition, the non-interlocking fractures were prepared by copying a carved fracture surface with the white silicon gum and mating it with a flat and transparent acrylic plate. By using silicon gum, the fracture specimen is easily

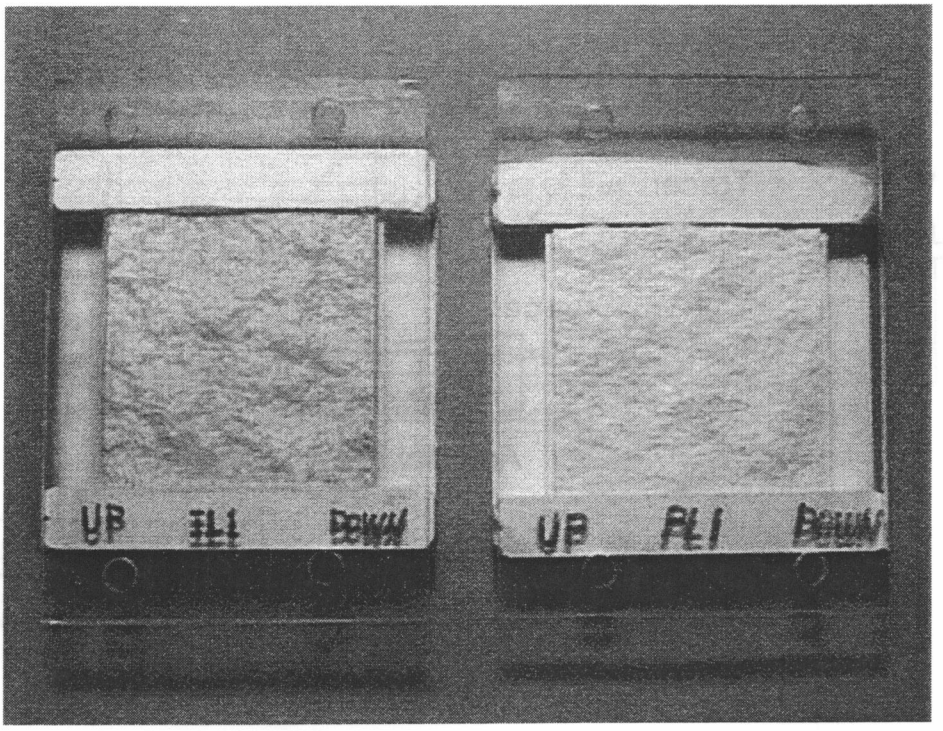

Figure 6.4: The prepared specimen for each type of fracture, IL1 and PL1.

Table 6.1: The fractal dimension, steepness and interlocking wavelength of the specimens for each specimen.

Specimen Name	Fractal Dimension	Steepness	Interlocking Wavelength (mm)
IL1	1.21	0.0236	1.0
IL2	1.21	0.0085	1.0
PL1	1.21	0.0228	-
PL2	1.21	0.0082	-

sealed and the contact area of the fracture can be changed easily. The transparent acrylic resin and plate were used to observe the flow behavior in the fracture directly. The prepared specimen for each type of fracture is shown in Figure 6.4. For each type of fracture, two fracture specimens of different steepness were prepared. The fractal dimension, steepness and interlocking wavelength of the specimens are shown in Table 6.1. The size of prepared fracture specimens is 51mm long and 51mm wide. In addition, the asperities of the same type of the specimens are on the same place of the fracture surfaces, though the height of them is different.

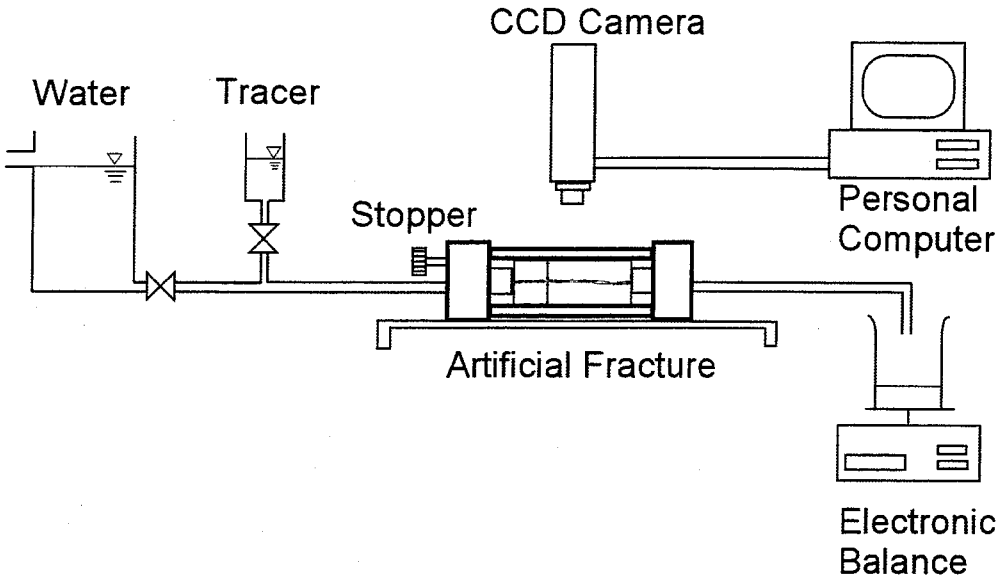

Figure 6.5: Schematic diagram of the physical flow experiment.

Second, the physical flow experiments to visualize the behavior of fluid flow in a single fracture were carried out. The schematic diagram of the experiments is shown in Figure 6.5. Tap water was overflowed the water tank to keep the hydraulic head constant. The water was first introduced into the fracture, and then the hydraulic head was adjusted by moving water tank upward or downward by a jack to get a proper flow rate. After the volumetric flow rate became almost constant, a tracer, black water paint, was introduced into the fracture little by little and the images of tracer flow were taken by a CCD camera. The taken images were stored in a personal computer. The volumetric flow rate was measured by weighting the effluent every constant time interval with electronic balance. Water temperature was also measured to know the water viscosity.

Finally, the contact area was estimated by the following method. Clear contrast between the fracture pore space and the contact area was obtained by filling the fracture pore space with the tracer. Therefore, the contact area of the fracture can be estimated by image processing.

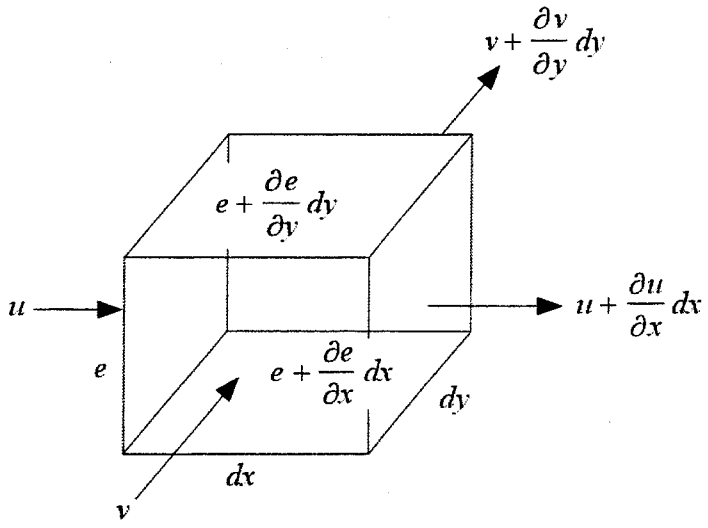

Figure 6.6: Influx and efflux in the small volume element.

6.2.3 The numerical flow simulations

The steady state laminar flow of an incompressible fluid flow through a fracture can be simulated by the following simplified Reynolds equation (Brown, 1987, 1989; Zimmerman *et al.*, 1991; Brown *et al.*, 1995)

$$\nabla \cdot (e^3 \nabla p) = 0 \tag{6.5}$$

where e is fracture aperture and p is flow potential. The most general form of Reynolds equation describes steady state laminar flow of a compressible viscous fluid between slightly nonplanar and nonparallel surfaces. It can be derived from Navier-Storkes equations assuming that flow is laminar, viscous shear dominates over inertial forces, the surface forming the flow channel have gentle slope, and the thickness of the fluid film is small relative to the lateral extent of the channel.

On the other hand, the simplified Reynolds equation can be derived by assuming the validity of local cubic law and the mass conservation in the small volume element as shown in Figure 6.6. For this small volume element, the volume of influx and efflux are represented by

$$\text{Influx: } uedy + vedx \tag{6.6}$$

$$\text{Efflux: } \left(u+\frac{\partial u}{\partial x}dx\right)\left(e+\frac{\partial e}{\partial x}dx\right)dy+\left(v+\frac{\partial v}{\partial y}dy\right)\left(e+\frac{\partial e}{\partial y}dy\right)dx \tag{6.7}$$

where u and v are flow rate in x and y direction respectively. For the steady state laminar flow, both of them are equal each other so that the mass may be conserved. Therefore, by equating them, the following equation can be obtained.

$$\frac{\partial(ue)}{\partial x}+\frac{\partial(ve)}{\partial y}=0 \tag{6.8}$$

Here, assuming that the cubic law is valid in the small volume element;

$$u=-\frac{e^2}{12\mu}\frac{\partial p}{\partial x} \tag{6.9}$$

$$v=-\frac{e^2}{12\mu}\frac{\partial p}{\partial y} \tag{6.10}$$

and substituting these equations into Equation (6.8) yields the Reynolds equation as follows.

$$\begin{aligned} & \frac{\partial}{\partial x}\left(-\frac{e^3}{12\mu}\frac{\partial p}{\partial x}\right)+\frac{\partial}{\partial y}\left(-\frac{e^3}{12\mu}\frac{\partial p}{\partial y}\right)=0 \\ \Leftrightarrow \quad & 3\left(\frac{\partial e}{\partial x}\frac{\partial p}{\partial x}+\frac{\partial e}{\partial y}\frac{\partial p}{\partial y}\right)+e\left(\frac{\partial^2 p}{\partial x^2}+\frac{\partial^2 p}{\partial y^2}\right)=0 \\ \Leftrightarrow \quad & \nabla\cdot(e^3\nabla p)=0 \end{aligned} \tag{6.11}$$

The numerical flow simulation was performed by solving the Reynolds equation for the aperture distributions generated by the Glover's method. In this simulation, finite difference method was used to solve the Reynolds equation.

For the numerical flow simulation, the topography of the fracture surfaces was the same as that of the fracture surfaces used for the physical flow experiments. In addition, the aperture data were numerically generated at the 256 by 256 points whose interval is 0.2mm by adjusting the contact area to be equal to that of the fracture surface used for the physical flow experiment. In the flow simulations, both sides of the fracture parallel to the nominal pressure gradient are no-flow boundaries. At that boundary, fluid can flow along it, but can not flow across it. Moreover, both ends of the fracture perpendicular to the nominal pressure gradient are constant pressure boundaries. In the numerical flow simulations, the inlet and outlet pressures were set to 1.0 and 0.0 respectively.

By solving the Reynolds equation under such the boundary conditions, the

pressure distribution in the fracture can be obtained and the volumetric flow rate vector can be calculated by the local cubic law. In the calculation of volumetric flow rate, the fluid viscosity was set to 1.0. In order to visualize the behavior of fluid flow through a fracture, the volumetric flow rate vectors were plotted. Furthermore, the total volumetric flow rate was calculated by adding the contribution from the individual flow vectors across the fracture parallel to the constant pressure boundary, since the both sides of the fracture parallel to the nominal pressure gradient are no-flow boundary.

6.3 The results of the visualization

6.3.1 The results of physical flow experiments

The visualized image for each specimen is shown in Figure 6.7(a)-(d). Each image shows the whole fracture; therefore, the size of the images is about 51mm long and 51mm wide. In these images, the fluid flows from the left to the right. In addition, for each specimen, the two-leveled image of the fracture whose pore space is filled with the tracer is shown in Figure 6.8(a)-(d). The contact area can be calculated from this figure. For each specimen, the ratio of contact area, the mean fracture aperture, the hydraulic head and the volumetric flow rate are shown in Table 6.2. The mean fracture aperture can be calculated by dividing the fracture pore volume by the nominal fracture area. In this physical flow experiment, however, the measurement of the fracture pore volume is very difficult, because the dead volume is much larger than the fracture pore volume and consequently the measurement error is very large. Therefore, the fracture pore volume was calculated from the numerical aperture data after adjusting the contact area. The contact area was adjusted by the overlapped area of the fracture surfaces as shown in Figure 6.9, but the change of fracture pore volume caused by the deformation of contacted asperities was ignored.

From the image of interlocking fractures, it can be observed that the streamlines are winding complicatedly and forming several channels. Since fluids can be thought to flow selectively at the large aperture in a fracture, such the complex streamlines means that the relatively large apertures distribute in such a complex manner. From the image of non-interlocking fractures, on the other hand, it can be observed that the streamlines are formed to avoid the contact area and they are not so complicated.

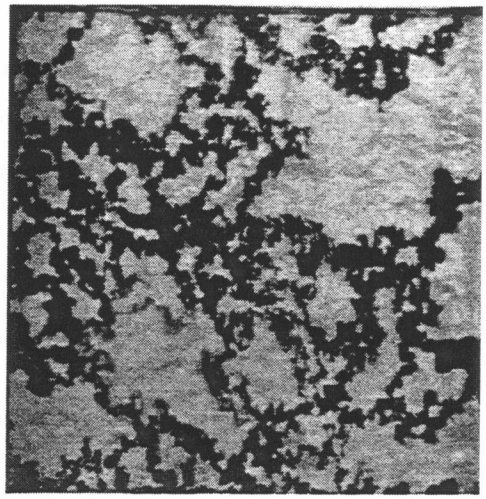

(a) IL1

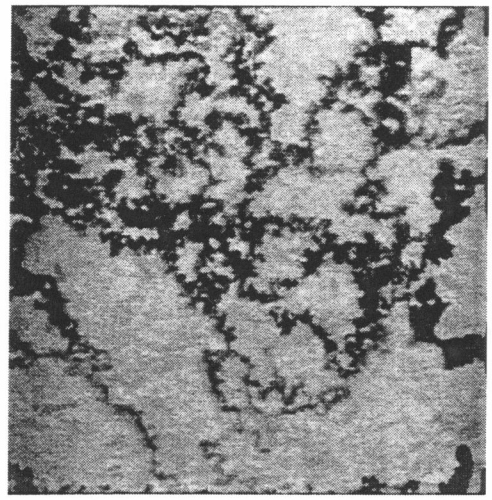

(b) IL2

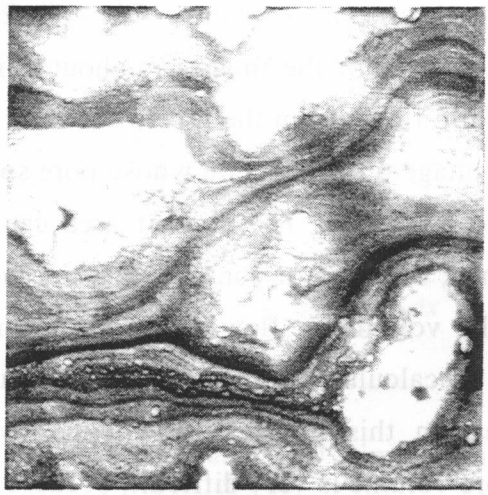

(c) PL1

(d) PL2

Figure 6.7: Fluid flow image observed in the physical flow experiment.

Table 6.2: The ratio of contact area to the fracture area, mean fracture aperture, hydraulic head, volumetric flow rate and two-dimensional tortuosity

Specimen Name	Contact Area Ratio (%)	Mean Fracture Aperture (mm)	Hydraulic Head (mm)	Volumetric Flow Rate		2D-Tortuosity	
				Experiment (cm^3/s)	Simulation (cm^3/s)	Experiment	Simulation
IL1	30	0.081	277	0.046	0.042	1.39~1.60	1.35~1.66
IL2	25	0.056	277	0.016	0.019	1.39~1.60	1.35~1.66
PL1	11	0.801	41	3.417	19.839	1.06~1.27	1.16~1.26
PL2	11	0.481	41	1.446	4.285	1.06~1.27	1.16~1.26

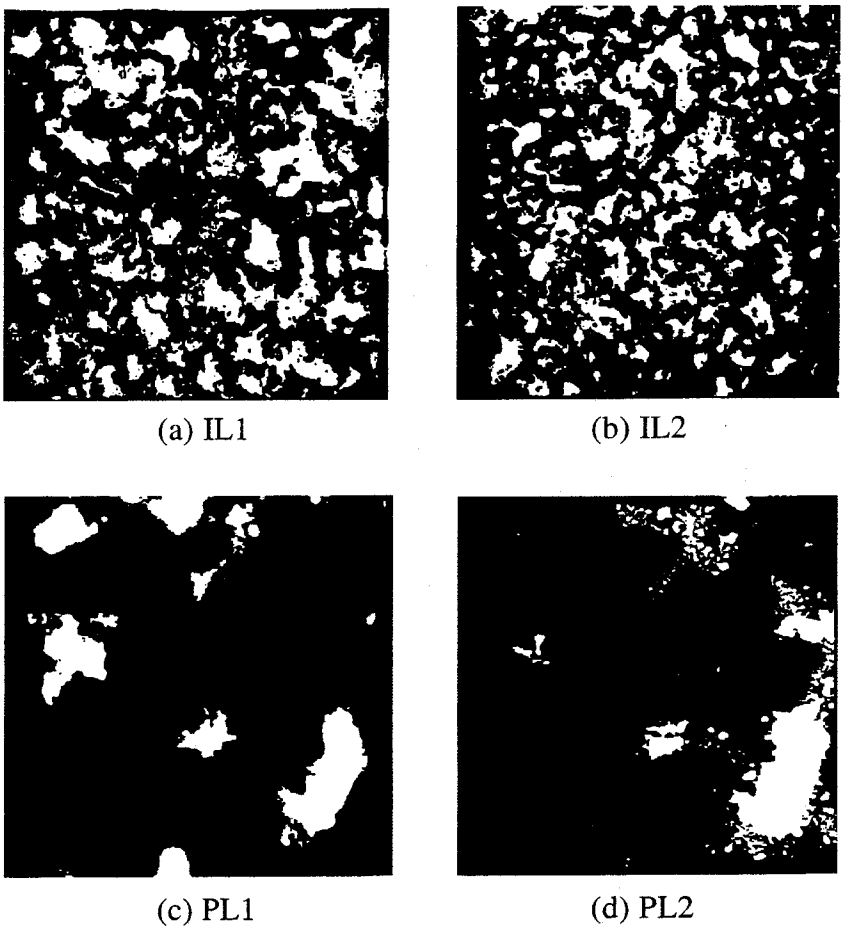

Figure 6.8: Two-leveled image of the fracture whose pore space is filled with the tracer

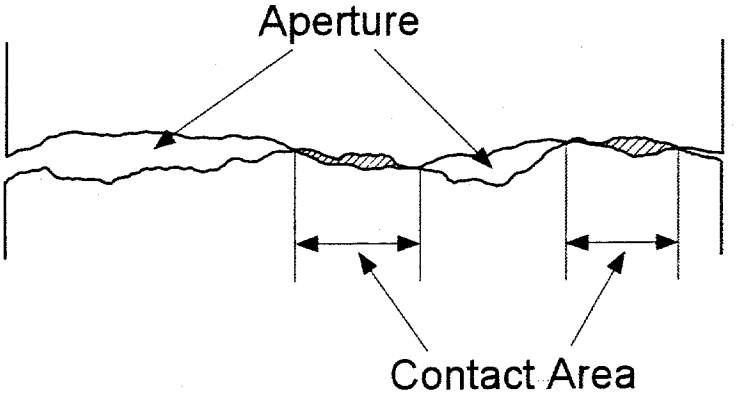

Figure 6.9: Fracture contact area. The overlapped areas of the fracture surfaces were regarded to the contact area and the change of fracture pore volume caused by the deformation of contacted asperities was ignored.

Furthermore, it can be observed that the shape of the streamlines is almost the same between the fractures having the same steepness. Therefore, it can be said that steepness does not affect the two dimensional tortuosity. For each type of fractures, the length of selected three main streamlines were measured and the two-dimensional tortuosity was estimated. The estimated two-dimensional tortuosity is also shown in Table 6.2.

6.3.2 The results of numerical flow simulations

The result of the numerical flow simulation for each specimen is shown in Figure 6.10(a)-(d). In these figures, the volumetric flow rate vectors are plotted at the 64 by 64 points on the image of the fracture aperture distribution to show them clearly, though the simulation was conducted for the 256 by 256 data points. Furthermore, the total volumetric flow rate for each specimen is shown in Table 6.2 with that of the physical flow experiment. It can be calculated by multiplying a factor by the simulation result according to the measured hydraulic head shown in Table 6.2 and water viscosity at 25 ° C, 8.90E-4Pa•s. In addition, the contact area and the mean fracture aperture are equal to those of the physical flow experiment.

From Figure 6.10, it can be observed that the streamlines of interlocking fractures are winding complicatedly and forming several thin channels as observed in the physical flow experiment. For the interlocking fractures, however, the shape of the flow channels is different from that observed in the physical flow experiment. On the other hand, for non-interlocking fractures, it can be observed that the gently winding streamlines are formed to avoid the contact area and the flow channels are relatively wide. In addition, the shape of the flow channels is very similar to that observed in the physical flow simulation.

A probable reason why the shape of flow channels is different between the physical flow experiment and the numerical flow simulation for the interlocking fractures and it is similar between them for the non-interlocking fractures is as follows. The fracture aperture is small and the number of contact area is many for the interlocking fractures as shown in Table 6.2 and Figure 6.8(a)-(b). In such the case, the aperture distribution is affected easily by the deformation of contacting asperities and the errors occurred in the specimen preparation. Such the deformation of contacting asperities is ignored in the numerical flow simulation. Consequently, it can be thought that the detail formation of flow channels can not be simulated sufficiently. On the other hand, the fracture aperture is large and the number of

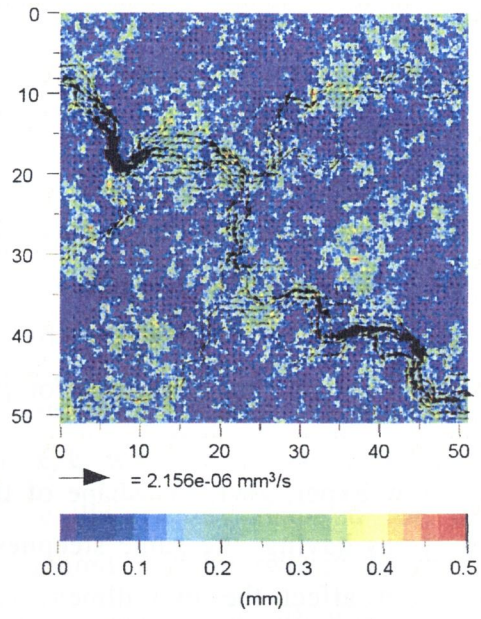

(a) IL1

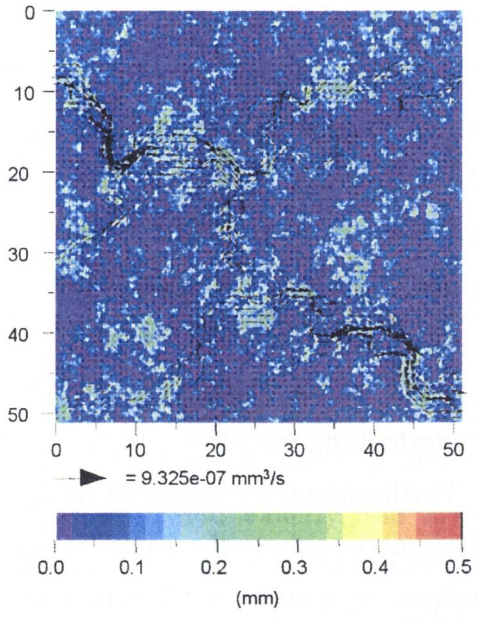

(b) IL2

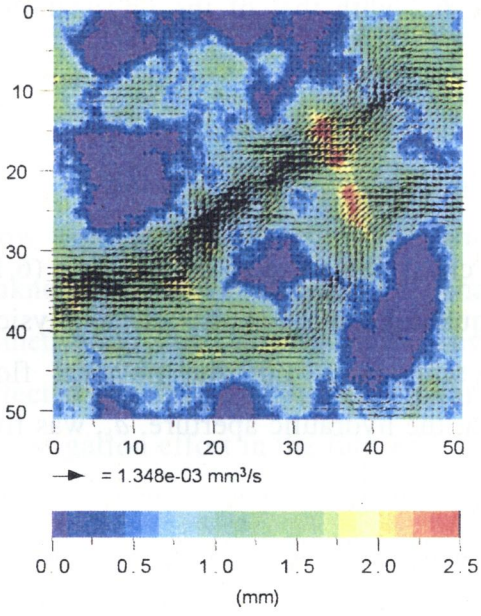

(c) PL1

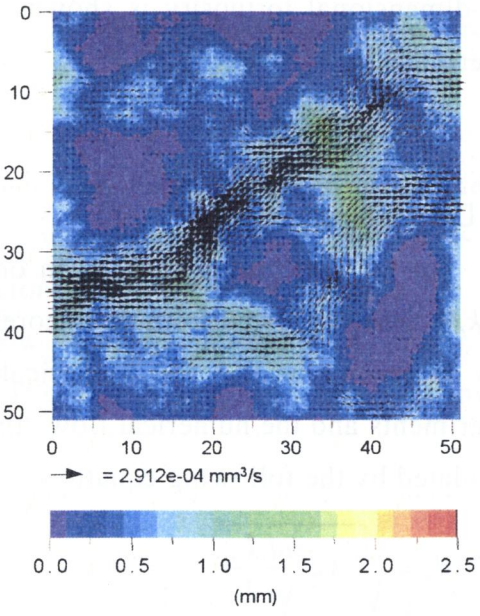

(d) PL2

Figure 6.10: Simulated volumetric flow rate vectors plotted on the image of the fracture aperture distribution.

contact area is few for non-interlocking fractures as shown in Table 6.2 and Figure 6.8(c)-(d). In such the case, the aperture distribution is not affected by the deformation of contacting asperities and the errors occurred in the specimen preparation so much. Consequently, it can be thought that the flow behavior of the numerical flow simulation corresponds to that of the physical flow experiment.

As shown in Table 6.2, the volumetric flow rate is almost the same between the physical flow experiment and numerical flow simulation for the interlocking fractures, but it is remarkably different between them for the non-interlocking fractures. This is because the volumetric flow rate was not measured exactly by the occurrence of air plugging during the volumetric flow rate measurement for the non-interlocking fractures.

Furthermore, as observed in the physical flow experiment, the shape of the streamlines is almost the same between the fractures having the same steepness. Therefore, it can be said that steepness does not affect the two dimensional tortuosity. For each type of fractures, the length of selected two main streamlines were measured and the two-dimensional tortuosity was estimated. The estimated two-dimensional tortuosity is shown in Table 6.2 with that of the physical flow experiment.

6.4 Discussion

For the fractures used here, in order to check the validity of Equation (6.1), the k_f/k_c was calculated from the theoretical equation and the results of the physical flow experiments and the numerical flow simulation. For the physical flow experiments and the numerical flow simulation, the hydraulic aperture, d_h, was first calculated by the following equation;

$$d_h = \sqrt[3]{-12\frac{\mu q}{\Delta p}\frac{L_x}{L_y}} \tag{6.12}$$

where μ is fluid viscosity, q is volumetric flow rate, Δp is pressure difference between inlet and outlet, L_x and L_y are fracture length and width respectively. Then the k_f/k_c was calculated by the following equation;

$$\frac{k_f}{k_c} = \frac{d_h^{\,3}}{<d>^3} \tag{6.13}$$

Table 6.3: The deviation from the cubic law of fracture permeability, k_f/k_c estimated from the results of the physical flow experiment and numerical flow simulation and from the theoretical equation.

Specimen Name	Experiment	Simulation	2D-Tourtuosity		Theory (β=2.0)		Theory (β=3.0)	
			Experiment	Simulation	Experiment	Simulation	Experiment	Simulation
IL1	0.340	0.314	1.45	1.66	0.621	0.474	0.414	0.316
IL2	0.343	0.420	1.45	1.66	0.678	0.518	0.452	0.345
PL1	0.177	1.028	1.27	1.26	0.814	0.827	0.542	0.551
PL2	0.347	1.029	1.27	1.26	0.886	0.900	0.590	0.600

where <d> is mean fracture aperture. On the other hand, for the theoretical equation, the k_f/k_c was calculated by applying the measured parameters to Equation (6.1). Since the fracture shape factor, β, can not be estimated exactly, the k_f/k_c was calculated for the two cases that β is equal to 2.0 and 3.0. In addition, the interlocking wavelength was used for h, which corresponds to the smallest size where the fluid flows faithfully along the fracture surface. The calculation results are shown in Table 6.3. In this table, the k_f/k_c of the PL1 and PL2 estimated from the physical flow experiment are wrong, because the measured volumetric flow rate is not exact.

From the Table 6.3, it can be recognized that the theoretical k_f/k_c shows near value to the k_f/k_c estimated from the physical flow experiment and the numerical flow simulation. Therefore, Equation (6.1) may be valid. However, it is still unknown how we estimate the shape factor and how we determine the two-dimensional tortuosity from the several flow channels. Furthermore, the k_f/k_c is affected severely by these two parameters. These problems must be solved by the investigation effort in the future.

6.5 Conclusions

In this chapter, the physical flow experiments and numerical flow simulations were carried out to visualize the streamlines in a fracture and to investigate the two-dimensional tortuosity for the interlocking and non-interlocking fractures. These fractures were artificially generated by using the fractal model. In addition, for these fractures, the validity of theoretical equation to estimate k_f/k_c presented in Chapter 5 is discussed by comparing the k_f/k_c among the theoretical equation, the

followings were suggested.

1) The streamlines of interlocking fracture are winding complicatedly and forming several channels. On the other hand, the streamlines of non-interlocking fracture are formed to avoid the contact area and they are not so complicated.
2) Steepness does not affect the two dimensional tortuosity.
3) Fluid flows selectively at the large aperture in a fracture.
4) It is difficult to match the results of numerical flow simulation with the results of physical flow experiment for interlocking fractures. A probable reason of this problem is that the aperture distribution is affected easily by the deformation of contacting asperities and errors occurred in the specimen preparation for such the small aperture fractures.
5) The theoretical k_f/k_c shows almost similar value to the k_f/k_c estimated from the physical flow experiment and the numerical flow simulation. Therefore, the theoretical equation may be valid.

From the third item, the two-dimensional tortuosity is probably determined from the random aperture distribution. Consequently, it is very difficult to determine it exactly. However, the range of it can be clarified in the relation with the interlocking wavelength, fractal parameters and contact area from this investigation for many cases. Therefore, in order to do so, the several problems as mentioned in this chapter must be solved by the investigation effort in the future.

References

Brown, S. R., Fluid flow through rock joints: the effect of surface roughness, *J. Geophys. Res.*, Vol. 92, 1337-1347, 1987.

Brown, S. R., Transport of fluid and electric current through a single fracture, *J. Geophys. Res.*, Vol. 94, 9429-9438, 1989.

Brown, S. R., Simple mathematical model of a rough fracture, *J. Geophys. Res.*, Vol. 100, 5941-5952, 1995.

Peitgen, H. -O. and D. Saupe, *The science of fractal images*, Ch. 1, Springer-Verlag, New York, 1988.

Glover, P. W. J., K. Matsuki, R. Hikima, and K. Hayashi, Fluid flow in fractally rough synthetic fractures, *Geophys. Res, Lett.*, Vol. 24,1803-1806, 1997.

Zimmerman, R. W., S. Kumar, and G. S. Bodvarsson, Lubrication theory analysis of the permeability of rough-walled fractures, *Int. J. Rock Mech. Min. Sci. & Geomech. Abstr.*, Vol. 28, 325-331, 1991.

CHPTER7

CONCLUDING REMARKS

As mentioned first, the surface properties of a rock fracture can be separated into geometric surface properties and material surface properties, and they play an important roll on its mechanical and hydrological properties. In this thesis, in order to characterize these two properties of a rock fracture, the geometric surface properties were represented by a fractal model made by variogram method, and the followings were studied. First, the problem of variogram method that the range of lag where the power law is valid is very small was discussed to make a precise fractal model by using variogram method. Second, JRC-diagram that is a new method to evaluate the surface roughness of a fracture surface was presented, and the size effect of the surface roughness based on this method was discussed. Third, the change of geometric surface properties and contact condition with the progress of shearing was investigated to apply JRC-diagram properly for the estimation of surface roughness. Finally, the geometric effect of a fracture surface on fracture permeability was investigated, and the deviation from the cubic law of fracture permeability was represented by using a fractal model. In addition, in order to understand the behavior of fluid flow in a fracture and to investigate the two-dimensional tortuosity, the streamlines were visualized by physical flow experiment and numerical flow simulation. Consequently, the followings were concluded.

In Chapter 2, it was clarified mathematically that the cause of the problem of variogram method is mainly the fact that the length of sampled profile is finite. It was also clarified mathematically that the range of lag decreases with the decrease in the fractal dimension of a profile. Furthermore, followings were concluded in this chapter. First, a sufficiently long profile sampled with sufficiently small sampling interval is necessary to make a precise fractal model. Second, the removal of the linear trend of a profile can also cause an error in the evaluation of the fractal dimension for the variogram method, but it is necessary for a consistent evaluation. These results in this chapter will help us to apply the variogram method for making a precise fractal model of a fracture surface.

In Chapter 3, first, it was shown that the fractal model of a rock fracture is uniquely determined by steepness, which is defined here, and fractal dimension. In

addition, it was clarified that the steepness and fractal dimension are closely related to the surface roughness and its size effect respectively. Second, a new original concept of JRC-diagram was presented to evaluate the fracture surface roughness and its size effect. In addition, the control size, which is the lag used for the roughness estimation by JRC-diagram, was suggested to be determined from the interlocking wavelength of fracture surfaces. Third, based on the concept of JRC-diagram, a theoretical equation that represents the size effect of *JRC* was derived.

For several specimens, in order to check the validity of JRC-diagram, the *JRC* estimated by JRC-diagram was compared with the *JRC* determined from JRC-profile. Moreover, the peak shear strength was estimated from these *JRC* values by using the Barton's empirical equation and compared with the results of shear test. Consequently, it was concluded that both the JRC-diagram and JRC-profile can not estimate *JRC* for non-sheared and interlocking fracture, but they can for sheared or non-interlocking fracture. However, JRC-diagram has a possibility to estimate the *JRC* of non-sheared and interlocking fracture, if the actual size of interlocking asperities that is under the stressed condition is much smaller than that estimated from profile measurement.

In Chapter 4, the changes of surface properties and contact condition with the progress of shearing were investigated by the precise surface topography measurement and the direct observation by using a microscope. In addition, the relation between the fracture contact area and P-wave amplitude is investigated to know the contact condition of a fracture under the stressed condition. Consequently, the followings were clarified. First, fracture surfaces degrade clearly after the peak shear strength and they become smooth with the progress of shearing. This is mainly caused by the failure of small and steep asperities in that stage of shearing. Second, the rock fracture interlocks closely by the application of shear stress at the beginning of shearing. Therefore, it can be thought that the actual interlocking wavelength is much smaller than that determined from profile measurement and JRC-diagram is probably applicable to estimate the correct *JRC* for an interlocking fracture. Third, after the peak shear strength, the contact points of the fracture are limited to the slope of asperities that has positive gradient to the shear direction, so that the dilation of the fracture increases with increasing the shear displacement. In addition, it was observed that the dilatancy curve is nearly parallel to the MEDF curve of more degraded fracture surfaces after shearing. On the other hand, the aperture increases with increasing the shear displacement at the other slope of the

contact asperities. Therefore, there exist smoothed areas and rough areas on the fracture surface, and consequently the standard deviation of the surface height change becomes large. Last, it was observed that the rms-amplitude of direct P-wave is directly proportional to the contact area of a fracture. However, since the rms-amplitude can be affected by the specific stiffness, it was suggested that the change of the specific stiffness during the shear test must be taken into consideration to estimate the contact area by using P-wave.

In Chapter 5, the deviation from the cubic law of fracture permeability was investigated experimentally and theoretically. Consequently, the deviation was represented quantitatively by using the fractal parameters, and the followings were clarified. First, between the fracture permeability, k_f, and the mean fracture aperture, $<d>$, the relation, $k_f=a<d>^b$, can be recognized and the value of b is probably dependent on the contact condition of fracture surfaces. In addition, k_f decreases with the increase in the steepness. Second, between the fracture permeability, k_f, and the confining pressure, P_c, the relation, $k_f=aP_c^{-b}$ (b=2.0~3.0), can be recognized and the style of this relation depends on the behavior of fracture closure. Third, the deviation from the cubic law of fracture permeability increases with the increase in two-dimensional tortuosity, fractal dimension and steepness. The effect of the two-dimensional tortuosity is the most remarkable among them especially when the control size is large. Fourth, the effect of fractal dimension and steepness on the deviation from the cubic law of fracture permeability decreases with increase in the control size. Last, it is possible that the deviation from the cubic law of fracture permeability decreases with the decrease in the mean fracture aperture, if the tortuosity does not change so large with the decrease in the mean fracture aperture.

As concluded in Chapter 5, two-dimensional tortuosity is an important parameter to determine the fracture permeability, but it is difficult to be estimated theoretically, because it depends on the random distribution of fracture aperture. Therefore, in Chapter 6, the physical flow experiments and numerical flow simulations were carried out to visualize the streamlines in a fracture and to investigate the two-dimensional tortuosity for the interlocking and non-interlocking fractures. In addition, for these fractures, the validity of theoretical equation to estimate k_f/k_c presented in Chapter 5 is discussed. Consequently, the followings were suggested. First, the streamlines of interlocking fracture are winding complicatedly and forming several channels. On the other hand, the streamlines of non-interlocking fracture are formed to avoid the contact area and they are not so

complicated. Second, steepness does not affect the two dimensional tortuosity. Third, fluid flows selectively at the large aperture in a fracture. Fourth, it is difficult to match the results of numerical flow simulation with the results of physical flow experiment for interlocking fractures. A probable reason of this problem is that the aperture distribution is affected easily by the deformation of contacting asperities and errors occurred in the specimen preparation for such the fractures of small aperture. Last, the theoretical k_f/k_c shows almost similar value to the k_f/k_c estimated from the physical flow experiment and the numerical flow simulation. Therefore, the theoretical equation may be valid. It will be difficult to determine the two-dimensional tortuosity exactly, because it is determined from the random aperture distribution. However, the range of it can be clarified in the relation with the interlocking wavelength, fractal parameters and contact area from the investigation for many cases, and it will be helpful to estimate the more correct fracture permeability.

These results shown in this thesis will help us to understand and characterize the mechanical and hydrological properties of a rock fracture. Finally, author will emphasize the following two points. First, the mechanical and hydrological properties can be discussed theoretically by separating the surface properties of a fracture into geometric surface properties and material surface properties. This is because the variety of the mechanical and hydrological properties of a fracture is mainly caused by the complexity of geometric surface properties, though the material surface properties are almost constant for a fracture. In addition, the geometric surface properties can be represented by a fractal model theoretically. Second, therefore, the concept of JRC-diagram will be applicable to develop a new method to estimate the shear strength considering the size effect and the contact condition of a fracture that is exchangeable for the Barton's empirical equation. Furthermore, the theoretical equation to estimate the deviation from the cubic law of fracture permeability will be more applicable.

For these purposes, the shear tests and the physical flow experiments or numerical flow simulations must be carried out for many fracture specimens whose fractal dimension, steepness and interlocking wavelength are controlled. The method to prepare such the fracture specimen has been developed in this study. Therefore, the shear tests and the physical flow experiment or numerical flow simulation will be carried out in the near future.

PUBLICATION LIST

—Relating to this work—

Chapter 2

S. Murata and T. Saito, The variogram method for a fractal model of a rock joint surface, Geotechnical and Geological Eng. Vol. 17, pp. 197-210, 1999.

S. Murata and T. Saito, The variogram method for conducting the fractal model of a rock joint surface, Proc. of the 10th Symp. on Rock Mech. In Japan, pp. 175-180, 1998 (in Japanese).

S. Murata and T. Saito, The variogram method for a fractal model of a rock joint surface, Proc. of Int. Conf. on Geomechanics/Ground Control in Mining and Underground Construction, Wollongon, Vol.2, pp. 1019-1028, 1998.

Chapter 3

S. Murata and T. Saito, Evaluation of rock joint surface roughness by using fractal model, Shigen-to-Sozai, Vol. 113, pp.555-560, 1997 (in Japanese).

Chapter 4

T. Saito and S. Murata, Failure of rock joint surface during shear test observed with precise surface topography measurement system, Proc. of the Korean-Japan Joint Symp. on Rock Eng., Seoul Korea, 1996.

S. Murata, K. Ogawa and T. Saito, The change of surface properties and contact condition of rock joint according to the progress of shearing, Proc. of the '99 Japan-Korea Joint Symp. on Rock Eng., Fukuoka Japan, pp. 343-350, 1999.

Chapter 5

S. Murata, K. Nagase and T. Saito, Effect of surface topography on fracture permeability, J. the Society of Material Science Japan, Vol. 47, pp.501-507, 1998 (in Japanese).